Observed Seasonal Evolution of the Antarctic Slope Current System off the Coast of Dronning Maud Land, East Antarctica

Julius Lauber[1], Laura de Steur[1], Tore Hattermann[2], and Elin Darelius[3]

[1]Norwegian Polar Institute
[2]Norwegian Polar Institute, Tromsø, Norway
[3]University of Bergen

October 17, 2023

Abstract

The access of heat to the Antarctic ice shelf cavities is regulated by the Antarctic Slope Front, separating relatively warm offshore water masses from cold water masses on the continental slope and inside the cavity. Previous observational studies along the East Antarctic continental slope have identified the drivers and variability of the front and the associated current, but a complete description of their seasonal cycle is currently lacking. In this study, we utilize two years (2019-2020) of observations from two oceanographic moorings east of the prime meridian to further detail the slope front and current seasonality. In combination with climatological hydrography and satellite-derived surface velocity, we identify processes that explain the hydrographic variability observed at the moorings. These processes include (i) an offshore spreading of seasonally formed Antarctic Surface Water, resulting in a lag in salinity and thermocline depth seasonality toward deeper isobaths, and (ii) the crucial role of buoyancy fluxes from sea ice melt and formation for the baroclinic seasonal cycle. Finally, data from two sub-ice-shelf moorings below Fimbulisen show that flow at the main sill into the cavity seasonally coincides with a weaker slope current in spring/summer. The flow is directed out of the cavity in autumn/winter when the slope current is strongest. The refined description of the variability of the slope current and front contributes to a more complete understanding of processes important for ice-shelf-ocean interactions in East Antarctica.

Observed Seasonal Evolution of the Antarctic Slope Current System off the Coast of Dronning Maud Land, East Antarctica

Julius Lauber[1,2], Laura de Steur[1], Tore Hattermann[1], Elin Darelius[2,3]

[1]Norwegian Polar Institute, Tromsø, Norway
[2]Geophysical Institute, University of Bergen, Bergen, Norway
[3]Bjerknes Centre for Climate Research, Bergen, Norway

Key Points:

- The seasonal maximum in thermocline depth and minimum in subsurface salinity occurs up to six months later over 2200 m than 1100 m isobath
- Buoyancy fluxes from sea ice melt play an important role in seasonal variations in the baroclinic slope current strength
- Flow into the Fimbulisen cavity is strongest in spring/summer when the Antarctic Slope Current is weakest

Corresponding author: Julius Lauber, `julius.lauber@npolar.no`

Abstract

The access of heat to the Antarctic ice shelf cavities is regulated by the Antarctic Slope Front, separating relatively warm offshore water masses from cold water masses on the continental slope and inside the cavity. Previous observational studies along the East Antarctic continental slope have identified the drivers and variability of the front and the associated current, but a complete description of their seasonal cycle is currently lacking. In this study, we utilize two years (2019-2020) of observations from two oceanographic moorings east of the prime meridian to further detail the slope front and current seasonality. In combination with climatological hydrography and satellite-derived surface velocity, we identify processes that explain the hydrographic variability observed at the moorings. These processes include (i) an offshore spreading of seasonally formed Antarctic Surface Water, resulting in a lag in salinity and thermocline depth seasonality toward deeper isobaths, and (ii) the crucial role of buoyancy fluxes from sea ice melt and formation for the baroclinic seasonal cycle. Finally, data from two sub-ice-shelf moorings below Fimbulisen show that flow at the main sill into the cavity seasonally coincides with a weaker slope current in spring/summer. The flow is directed out of the cavity in autumn/winter when the slope current is strongest. The refined description of the variability of the slope current and front contributes to a more complete understanding of processes important for ice-shelf-ocean interactions in East Antarctica.

Plain Language Summary

Ice shelves are the floating extensions of a land ice sheet. Along most of the East Antarctic coast, the water temperature below the ice shelves is close to the freezing point ($-2\,^\circ$C). This limits the melting of the ice from below. In front of the ice shelves, relatively warm water ($1\,^\circ$C) is located, but it usually cannot reach the ice due to a strong alongshore current, the Antarctic Slope Current. Here, we use temperature, salinity, and velocity observations from moored instruments at two locations within this current to investigate how it changes throughout the year. Our analyses are supported by two other data sets. We observe that changes in temperature, salinity, and velocity during the year happen earlier at the coast than offshore. In addition, we find that yearly sea ice melt during austral summer contributes to speeding up the Antarctic Slope Current in autumn. When the current is weakest, we observe a southward flow close to the seafloor toward Fimbulisen Ice Shelf, and a northward flow away from the shelf when the slope current is strongest. A better understanding of the Antarctic Slope Current is important to predict ice shelf melting in the future.

1 Introduction

The Antarctic Slope Front (ASF) is a key feature regulating offshore-onshore exchanges along most of the Antarctic coast (Jacobs, 1991; Thompson et al., 2018). Easterly alongshore winds drive onshore Ekman transport that accumulates surface water at the coast; due to continuity, this water is downwelled (Sverdrup, 1954; Mathiot et al., 2011), creating the ASF. The resulting meridional sea surface height (SSH) and density gradients balance a geostrophic current, the Antarctic Slope Current (ASC). The strength of the ASF/ASC controls the extent to which offshore Circumpolar Deep Water, capable of increasing basal melting, can access the continental shelf and the ice shelf cavities (Smedsrud et al., 2006; Nøst et al., 2011; Nakayama et al., 2021).

In the Weddell Sea, the large-scale circulation is dominated by the clockwise Weddell Gyre (Deacon, 1979; Vernet et al., 2019; Neme et al., 2021), driven by the large-scale wind stress curl (Gordon et al., 1981; Armitage et al., 2018; Auger, Sallée, et al., 2022) modulated by sea ice (Naveira Garabato et al., 2019). The southern limb of the gyre represents the ASC which in Dronning Maud Land (DML, 20°W-45°E) flows along the narrow continental shelf in close proximity to the ice shelves (Smedsrud et al., 2006; Nøst et al., 2011). In this region, the meridional SSH and density gradients lead to a westward ASC (Thompson et al., 2018) that decreases with depth (Huneke et al., 2022; Le Paih et al., 2020). In summer, a counter-current near the bottom has been observed (Heywood et al., 1998; Núñez-Riboni & Fahrbach, 2009; Chavanne et al., 2010). Warm Deep Water (WDW), a derivative of Circumpolar Deep Water in the Weddell Sea, is located close to the coast, but suppressed below the shelf break depth due to a steep ASF (Heywood et al., 1998; Hattermann, 2018; Thompson et al., 2018). This regime has been labeled as the Fresh Shelf regime by Thompson et al. (2018). Despite the steep ASF, modified WDW (mWDW) may cross the continental slope toward the ice shelf cavities via baroclinic eddies (Nøst et al., 2011; Hattermann et al., 2012; Thompson et al., 2014). As opposed to the West Antarctic ice shelves, however, no continuous warm water presence has yet been observed in the DML ice shelf cavities (Hattermann et al., 2012; Lauber, Hattermann, et al., 2023).

Previous analyses of the ASF/ASC system have revealed both the hydrography (Hattermann, 2018; Pauthenet et al., 2021) and the currents (Le Paih et al., 2020) to evolve coherently along the southern rim of the Weddell Sea, following isobaths due to the conservation of potential vorticity (Thompson et al., 2018). Auger, Sallée, et al. (2022) proposed that the SSH is seasonally forced by the zonal ocean stress (wind stress modulated by sea ice) over shallow isobaths ($< 1000\,\mathrm{m}$) and by ocean stress curl over deep isobaths ($> 1000\,\mathrm{m}$). The strongest depth-mean currents from moored instruments at the prime meridian have been observed in April/May over 2000 m depth, and in June over 3500 m depth, i.e. delayed by one to two months (Núñez-Riboni & Fahrbach, 2009; Le Paih et al., 2020). A similar delay in ASC seasonality between shallow and deep isobaths was found in circum-Antarctic satellite-derived geostrophic surface velocities (Auger, Sallée, et al., 2022). This feature has been hypothesized to originate from the sea ice edge seasonally moving offshore and associated changes in atmosphere-ocean momentum transfer (Núñez-Riboni & Fahrbach, 2009; Auger, Sallée, et al., 2022).

The baroclinic variability of the ASC on seasonal timescales in the Weddell Sea is associated with a steepening of the ASF from March to July and a relaxing from August to February (Pauthenet et al., 2021), caused by buoyancy forcing (Heywood et al., 1998) and wind (Graham et al., 2013): sea ice melt and surface warming from October/November on create a fresh and warm, and thus buoyant, water mass called Antarctic Surface Water (ASW). It accumulates at the coast via wind-driven onshore Ekman transport, seasonally forming a secondary, relatively shallow ($< 250\,\mathrm{m}$) front near the surface around February to April (Heywood et al., 1998; Hattermann, 2018). It is, however, unclear to what extent the seasonal production of ASW, which is accumulated at the coast, drives the ASC, independently of a seasonal ocean stress increase. Eddy overturning counteracts the steepening of the ASF and secondary front (Nøst et al., 2011; Zhou et al., 2014; Stewart & Thompson, 2015) and eddy-resolving models indicate that this is associated with an offshore spreading of ASW (Si et al., 2023). Following the sea ice minimum, which typically occurs in March, the ASW is gradually transformed into more saline Winter Water (WW) via brine release due to sea ice formation (Nøst et al., 2011). Overall, our knowledge of the ASF/ASC is based on a limited amount of observations and idealized models and hence it is incomplete. As a consequence, it is unknown how the ASF/ASC seasonality relates to warm inflow under the ice shelves along the eastern Weddell Sea.

In this study, we present new time series of temperature, salinity, oxygen, and velocity from April 2019 to December 2020, obtained from two oceanographic moorings located over isobaths of 1100 m and 2200 m east of the prime meridian. These data are introduced in section 2, along with a CTD section at 6°E, climatological hydrography (Hattermann, 2018), satellite-derived surface geostrophic velocities (Auger, Prandi, & Sallée, 2022), and mooring observations from the ice shelf cavity of Fimbulisen (located 200 km downstream). Methods to analyze these data are described in section 3. The new ASF/ASC observations are presented in section 4.1, and seasonal drivers of ASF/ASC seasonality are refined using the mentioned auxiliary data sets in section 4.2. In section 4.3, we assess how the seasonal ASF/ASC variability relates to the inflow into the ice shelf cavity of Fimbulisen. Finally, the results are discussed in light of the existing literature in section 5, and final conclusions are given in section 6.

2 Data

Two oceanographic moorings were deployed from R/V Kronprins Haakon in March 2019 during the Southern Ocean Ecosystem cruise off the DML coast and recovered from M/V Malik Arctica in December 2020 and January 2021 during the Troll Transect cruise. One mooring (DML_{deep}) was located at 6.0°E, 69.1°S over a water depth of 2166 m. The other mooring ($DML_{shallow}$) was located at 10.6°E, 69.4°S over a water depth of 1059 m, on the eastern flank of "Astrid Ridge" (Fig. 1a). Both moorings were equipped with one Teledyne 300 kHz ADCP and one Teledyne 150 kHz ADCP, two Nortek Aquadopp current meters, three/four Sea-Bird SBE37 MicroCATs, and 11/10 Sea-Bird SBE56 thermistors (DML_{deep}/$DML_{shallow}$). Details about the instrumentation are given in Table S1 and S2 in Supporting Information S1.

The mooring data are complemented by a CTD section that was taken between 70°S and 68°S along 6°E during the Troll Transect cruise in December 2020 and January 2021 using an SBE 911plus CTD.

A climatology of temperature and salinity sections with monthly resolution obtained from instrumented seals and ship sections around 17°W between 1977 and 2016 was used (Hattermann, 2018, referred to as H18 hereafter) to support and extend the analyses from our mooring observations.

We also include a data set of satellite-derived SSH and surface geostrophic current anomalies (Auger, Prandi, & Sallée, 2022, referred to as A22 hereafter), spanning the period from April 2013 to July 2019. These data overlap only partly with the open-ocean mooring period starting in late March 2019, and instead of comparing the time series directly, monthly mean climatologies of the SSH and geostrophic currents were calculated for the grid points along 6°E.

Monthly mean sea ice concentration (DiGirolamo et al., 2022) and velocity (Tschudi et al., 2019) data at 25 km resolution were obtained from the National Snow and Ice Data Centre. Monthly mean 10 m wind velocities were taken from the fifth generation of European Center for Medium-Range Weather Forecasts atmospheric reanalyses (ERA5, Hersbach et al., 2023).

In addition, data from two sub-ice-shelf moorings installed under Fimbulisen (Hattermann et al., 2012; Lauber, Hattermann, et al., 2023) were used. These moorings are located along expected major deep inflow pathways of WDW into the cavity (M1 and M3, Fig. 1a) and have delivered temperature and velocity data at two depths each from 2009 to 2021.

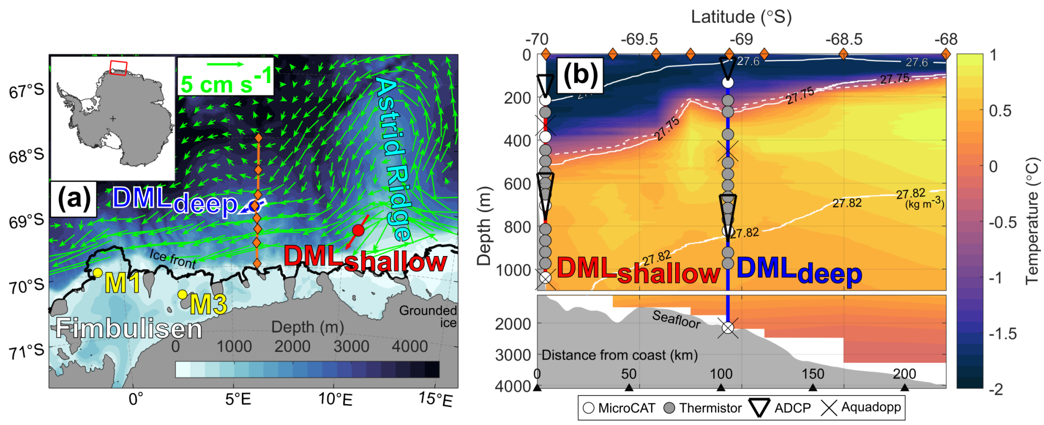

Figure 1. (a) Map of the study region. DML_{deep}/$DML_{shallow}$ denote the open-ocean moorings, and M1/3 denote the sub-ice shelf moorings. The orange line shows the location of the CTD section in panel b, with stations marked by diamonds. Colors show the bathymetry (IBCSO v2, Dorschel et al., 2022). Arrows at the offshore mooring locations show the direction and strength of the depth- and time-averaged currents, and green arrows show the difference between April to July and August to March in surface geostrophic currents (Auger, Prandi, & Sallée, 2022). The scale arrow is valid for all arrows. (b) In-situ temperature of the CTD section indicated by the orange line in panel a. Solid white lines show selected isopycnals (potential density anomaly) and the single dashed white line shows the $-0.3\,°C$ isotherm. Diamonds at the top are the station locations. The vertical blue line shows the location of DML_{deep}, and the vertical red line shows the isobath-projected location of $DML_{shallow}$.

3 Methods

To simplify investigations across the ASF/ASC, the data of $DML_{shallow}$ were projected on the same isobath at the longitude of DML_{deep} (Fig. 1b). When doing this, we assumed that the flow (green arrows in Fig. 1a) is oriented along isobaths, as has been observed by Le Paih et al. (2020) for the Weddell Sea and is corroborated by theoretical considerations of Isachsen et al. (2003). Therefore, for all velocity data, the component in the direction of the time- and depth-mean (red/blue arrow in Fig. 1a) will be shown in the following. The original location of DML_{deep} (105 km distance from the coast) and the projected location of $DML_{shallow}$ (10 km distance from the coast) within the ASF with their instruments are shown in Fig. 1b.

Daily and monthly averages of the mooring time series were computed for use in subsequent analysis. Hydrographic properties like absolute salinity, conservative temperature, and potential density were computed using the Gibbs Seawater Toolbox (McDougall & Barker, 2011). Temporary gaps in some of the ADCP bins due to seasonally reduced backscatter intensity were filled or extrapolated via a vertical linear regression of all available bins.

Vertical profiles of temperature and salinity of the H18 data, provided as a function of isobath, were projected on the bathymetry at 6°E, where the continental slope is less steep than at the original longitude of the climatology of 17°W. For this purpose, the bathymetry at 6°E was taken as a longitudinal average from 3°E to 9°E, based on IBCSO v2 data (Dorschel et al., 2022), to smooth out small-scale features.

Based on the general water mass distribution, the thermocline depth (TCD), i.e. the depth of the interface between WDW and WW, at the open-ocean moorings was defined as the depth of the $-0.3\,°$C isotherm after linear interpolation. Due to the vertically densely spaced thermistors (Fig. 1b), this depth was determined with an uncertainty of less than 50 m. The ASF slope was then calculated by combining the two thermocline depths:

$$slope_{ASF} = \frac{TCD_{shallow} - TCD_{deep}}{\Delta y} \tag{1}$$

Here, $TCD_{shallow}$ and TCD_{deep} are the thermocline depths for $\mathrm{DML_{shallow}}$ and $\mathrm{DML_{deep}}$, respectively, and $\Delta y = 100\,\mathrm{km}$ is the horizontal distance between the position of $\mathrm{DML_{deep}}$ and the projected position of $\mathrm{DML_{shallow}}$. The same calculation was conducted for the H18 data over the corresponding isobaths.

The barotropic velocity, i.e. the depth-independent component, was estimated from the mooring data (UBT_{obs}) via averages over the depth ranges where the vertical gradient in velocity is the smallest:

$$UBT_{obs} = \overline{U_{obs,\Delta z}} \tag{2}$$

Here, $U_{obs,\Delta z}$ is the observed along-stream velocity of the lowermost 12 bins of the lower ADCP at each mooring (683-773 m at $\mathrm{DML_{shallow}}$, 784-874 m at $\mathrm{DML_{deep}}$), selected after inspecting the profiles. The bar indicates an average over this depth range. For comparison, the barotropic velocity was also estimated from the auxiliary data by taking the difference between the A22 surface geostrophic velocity at 6°E ($UGEO_{A22}$, containing both barotropic and baroclinic current components) and the surface baroclinic velocity from the H18 data (UBC_{H18}, defined in Eqn. 5) after binning them on the same grid:

$$UBT_{H18A22} = UGEO_{A22} - UBC_{H18} \tag{3}$$

From the resulting time-latitude field of velocity, time series at the mooring isobaths were extracted.

The near-surface baroclinic velocity, i.e. the depth-varying component, was estimated from the mooring data (UBC_{obs}) by subtracting UBT_{obs} from the measured velocity at the uppermost ADCP bin (100 m at $\mathrm{DML_{shallow}}$, 20 m at $\mathrm{DML_{deep}}$):

$$UBC_{obs} = U_{obs} - UBT_{obs} \tag{4}$$

Here, U_{obs} is the observed along-stream velocity at the uppermost ADCP bin. The baroclinic velocity was also calculated from the H18 climatology for 6°E (UBC_{H18}) using the thermal wind equation:

$$UBC^{i}_{H18} = \frac{\Delta z}{\rho_0 f} \frac{\rho^{i}_{j+1} - \rho^{i}_{j}}{\Delta y} + UBC^{i-1}_{j} \tag{5}$$

Here, $\Delta z = 20\,\mathrm{m}$ is the depth increment, $\rho_0 = 1028\,\mathrm{kg\,m^{-3}}$ is a background density, f is the Coriolis parameter, i is the upward increasing depth index, j is the northward increasing meridional index, and $\Delta y = 4\,\mathrm{km}$ is the meridional increment. Zero velocity was assumed at the bottom or the lowest depth with data available. From the resulting depth-isobath-time field, time series were extracted over the isobaths and at the upper ADCP bin depths of $\mathrm{DML_{deep}}$ and $\mathrm{DML_{shallow}}$ to compare to UBC_{obs}.

Sea ice concentration and velocity, as well as wind data were interpolated on a common polar stereographic grid and combined to yield an estimate of the ocean stress (Martin et al., 2016; Dotto et al., 2018):

$$\vec{\tau} = \alpha\vec{\tau}_{ice-water} + (1-\alpha)\vec{\tau}_{air-water} \tag{6}$$

with

$$\vec{\tau}_{ice-water} = \rho_{water} C_{iw} \left|\vec{U}_{ice}\right| \vec{U}_{ice} \quad (7)$$

$$\vec{\tau}_{air-water} = \rho_{air} C_d \left|\vec{U}_{air}\right| \vec{U}_{air} \quad (8)$$

Here, α is the sea ice concentration, $\rho_{air} = 1.25\,\mathrm{kg\,m^{-3}}$ is the background density of air, $\rho_{water} = 1028\,\mathrm{kg\,m^{-3}}$ is the background density of seawater, $\vec{U}_{ice}$ is the horizontal sea ice velocity, $\vec{U}_{air}$ is the 10 m horizontal wind and $C_d = 1.25\times10^{-3}$ and $C_{iw} = 5.50\times10^{-3}$ (Tsamados et al., 2014) are the drag coefficients for the air-water and ice-water interface, respectively. Stresses from the ocean currents on the ice from below were not included here, possibly creating biases close to the coast where the sea ice velocity is similar to the ocean velocity (Stewart et al., 2019). Le Paih et al. (2020), however, show that the ocean stress in this region can still be qualitatively valid despite neglecting the ocean currents. The curl was calculated from the ocean stress, with positive (negative) values indicating downwelling (upwelling) favorable conditions.

To assess the relationship between the ASF/ASC dynamics and inflow of mWDW below Fimbulisen, the data from the lower M1 and M3 instruments (at 540 m and 450 m, respectively) close to the seabed were used, referred to as $\mathrm{M1_{lower}}$ and $\mathrm{M3_{lower}}$ hereafter. The velocity was rotated to be oriented into the cavity along the bathymetry, that is $-30°$ at $\mathrm{M1_{lower}}$ and $-120°$ at $\mathrm{M3_{lower}}$ (0° is directed toward the east and negative values indicate a clockwise rotation).

4 Results

4.1 Mooring Observations

4.1.1 Hydrography

The CTD section from December 2020 and January 2021 (Fig. 1b) shows the typical southward down-sloping isopycnals of the ASF and the offshore core of the WDW at the northern edge of the section at a depth of around 300-400 m. The section represents a snapshot of the ASF during summertime.

A Hovmöller diagram of temperature at $\mathrm{DML_{shallow}}$ (Fig. 2a) shows a layer of cold water with temperatures down to $-1.9\,°\mathrm{C}$ over a layer of warm water with temperatures up to $1\,°\mathrm{C}$. The thermocline depth ($-0.3\,°\mathrm{C}$ isotherm) shows a systematic seasonality, deepening between April and June to 500 m, and shoaling between July and March to

200 m. At $\mathrm{DML_{deep}}$, the thermocline is on average 100 m shallower than at $\mathrm{DML_{shallow}}$ (Fig. 2c) and deepens between June and December to 400 m, i.e. it reaches its maximum depth six months later compared to $\mathrm{DML_{shallow}}$. In 2020, the deepening is interrupted by a period of shoaling in October/November. The thermocline continues to shoal to 200 m from January to May, and reaches its minimum depth two months later compared to $\mathrm{DML_{shallow}}$. The warmest WDW is seen at both sites when the thermocline is shallowest.

The upper-ocean water masses (of which the densities are almost entirely determined by salinity) at $\mathrm{DML_{shallow}}$ are characterized in a temperature-salinity (T-S) diagram (Fig. 3a): the upper water mass is cold ($\approx -1.8\,^\circ\mathrm{C}$) and fresh ($\approx 34.5\,\mathrm{g\,kg^{-1}}$) WW, transforming into mWDW by mixing with the lower water mass which is warm ($\approx 1\,^\circ\mathrm{C}$) and saline ($\approx 34.8\,\mathrm{g\,kg^{-1}}$) WDW. Oxygen (colors in Fig. 3 and time series in Fig. S1 in Supporting Information S1) is a measure of the origin of the water masses. The freshest and oxygen-richest WW is observed at the uppermost MicroCAT (210 m) at the time of the deepest thermocline in winter in June. This water mass is similar to Eastern Shelf Water, a mix between ASW and WW. The observed WW in June 2019 is almost $0.1\,\mathrm{g\,kg^{-1}}$ fresher and richer in oxygen than in June 2020. During the period of thermocline shoaling from July onward, mWDW gradually appears. The most saline, warm, and oxygen-poor mWDW is observed in March when the thermocline is shallowest (see also Fig. 2a). At the uppermost MicroCAT (130 m) at $\mathrm{DML_{deep}}$, the WDW shows similar properties as at $\mathrm{DML_{shallow}}$, but the WW is generally more saline (Fig. 3b). A first seasonal salinity minimum and oxygen maximum are observed in June 2019. After that, temperature and salinity first increase toward mWDW, but then decrease back to WW. This yields a second seasonal salinity minimum and oxygen maximum at the time of the deepest thermocline in December 2019. During the period of thermocline shoaling, the water mass properties change toward mWDW until May 2020. After that, when the thermocline deepens, WW appears again, which is $0.05\,\mathrm{g\,kg^{-1}}$ more saline and has a lower oxygen concentration than in 2019. This is similar to the higher salinities and reduced oxygen observed at $\mathrm{DML_{shallow}}$ in 2020 (relative to 2019).

The observed seasonal deepening and freshening of the WW layer at $\mathrm{DML_{shallow}}$ (Fig. 2a) is attributed to the wind-driven accumulation of ASW at the coast (Zhou et al., 2014; Hattermann, 2018): summer sea ice melt between September and February (Fig. 4a) adds freshwater to form ASW. The latter is downwelled at the coast due to the prevailing easterly winds, explaining the salinity minimum and oxygen maximum at 210 m at $\mathrm{DML}_{\mathrm{shallow}}$ in June 2019 and 2020 (Fig. 3a and 4b) and the deepest thermocline one month later in July (Fig. 4c). Sea ice formation between March and August (Fig. 4a) releases brine into the upper ocean and leads to a salinity increase between July and September. With temperatures almost at the freezing point and oxygen close to its maximum value, this indicates that convection takes place down to 210 m depth during this period at $\mathrm{DML}_{\mathrm{shallow}}$ in 2019 (box in Fig. 3a). In 2020, the temperature is higher and the oxygen concentration is lower during the sea ice formation period, suggesting that convection did not reach down to this depth.

We also identify a period of convection at $\mathrm{DML}_{\mathrm{deep}}$: From June to August 2020, the water mass evolution from mWDW to similarly cold, but more saline and less oxygen-rich WW than in 2019 shows a mixing between mWDW and WW salinified by convection (box in Fig. 3b). In October/November 2020, the increase in temperature and salinity (off the direct mixing line toward WDW) and decrease in oxygen indicate that the convection reached through the thermocline, mixing WDW upward. This is neither observed in 2019 nor at $\mathrm{DML}_{\mathrm{shallow}}$. At 130 m at $\mathrm{DML}_{\mathrm{deep}}$, the different seasonal cycles in salinity (Fig. 4b) and thermocline depth (Fig. 4c) than at $\mathrm{DML}_{\mathrm{shallow}}$ indicate that local downwelling of ASW does not control the seasonal hydrography here: the salinity minimum in December cannot be explained by local surface freshwater input, as brine release during the freezing season from March to August (Fig. 4a) would increase the salinity, and freshwater from sea ice melt would cause a salinity minimum at the end (i.e. in March), not the beginning of the melt season. The drivers of the hydrographic seasonality at $\mathrm{DML}_{\mathrm{deep}}$ will be explored in section 4.2.

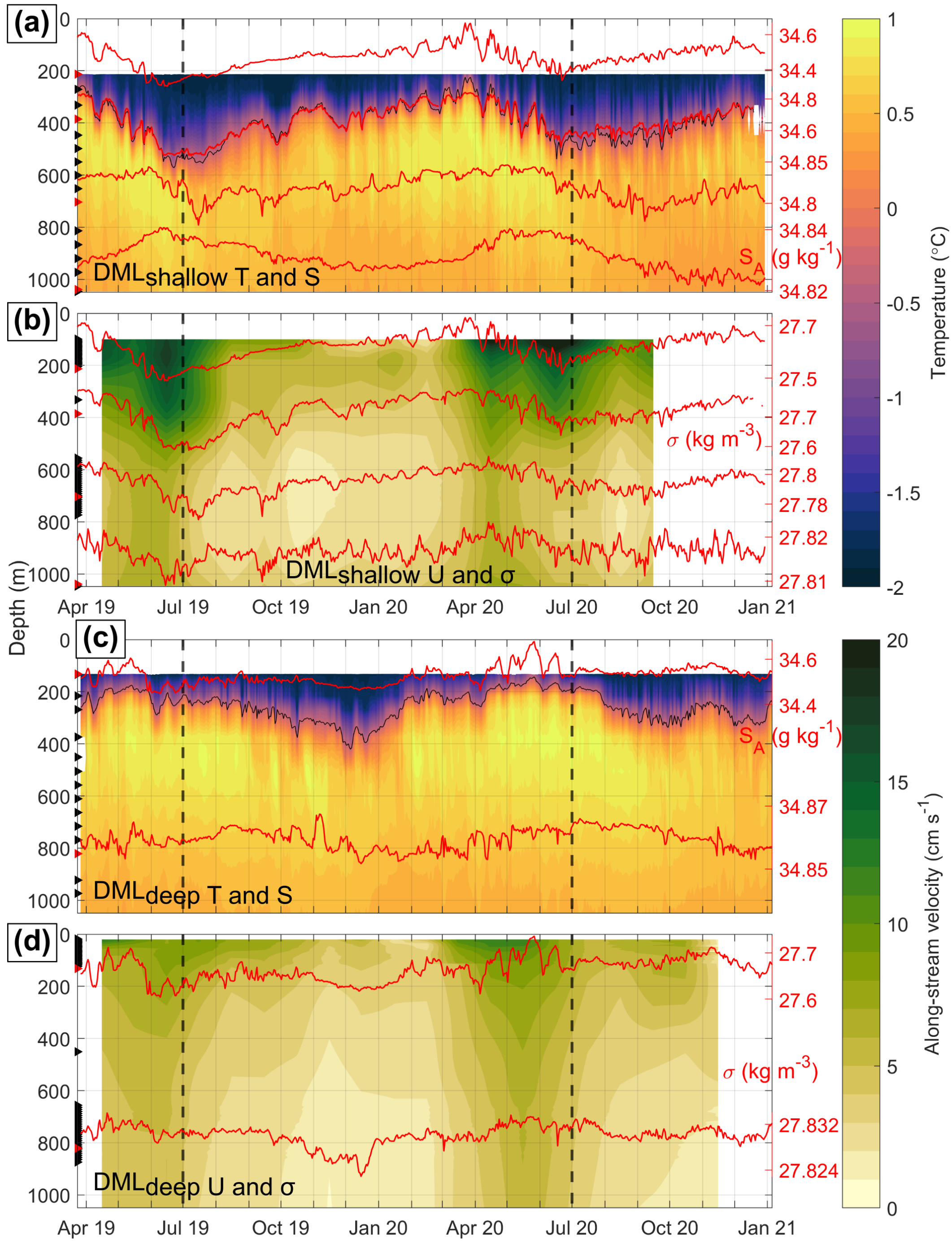

Figure 2. (a) Hovmöller diagram of daily averaged in-situ temperature at DML$_{\mathrm{shallow}}$. The black contour indicates the $-0.3\,^{\circ}$C isotherm. Black triangles denote the depths of temperature measurements. Red lines show daily averaged time series of absolute salinity (right axes) for the depths marked with red triangles. (b) Hovmöller diagram of monthly averaged along-stream velocity at DML$_{\mathrm{shallow}}$. Black triangles denote the depths of velocity measurements. Red lines show daily averaged time series of potential density anomaly (right axes) for the depths marked with red triangles. (c) Same as a, but for DML$_{\mathrm{deep}}$. (d) Same as b, but for DML$_{\mathrm{deep}}$. In c and d, the y-axis has been cut off at the bottom depth of DML$_{\mathrm{shallow}}$ for better comparability.

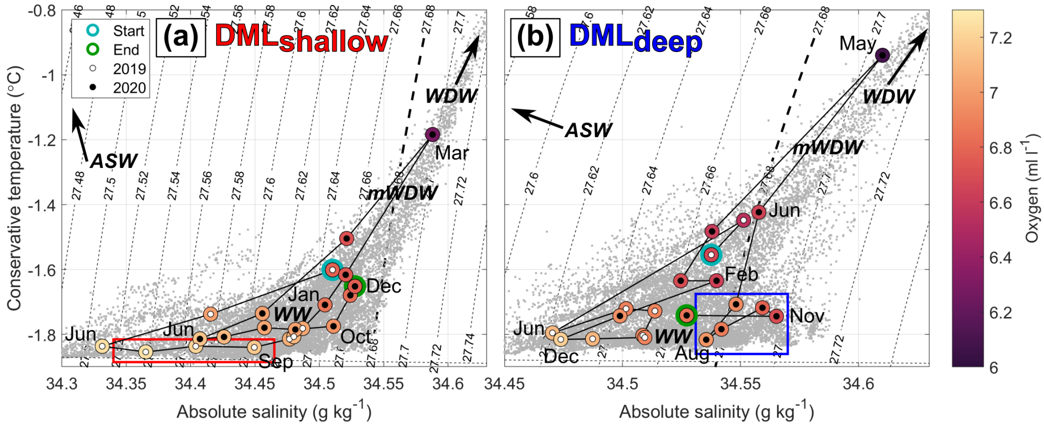

Figure 3. T-S diagrams with dissolved oxygen of the upper MicroCAT at (a) DML$_{\mathrm{shallow}}$ (210 m) and (b) DML$_{\mathrm{deep}}$ (130 m). Grey dots are the fully resolved hourly data, and colored dots are the monthly averaged data. Black lines connect the monthly points. The boxes show potential periods of convection. The thick black dotted line indicates the 27.68 kg m^{-3} isopycnal for better comparability between the two panels, as their x-axis ranges differ.

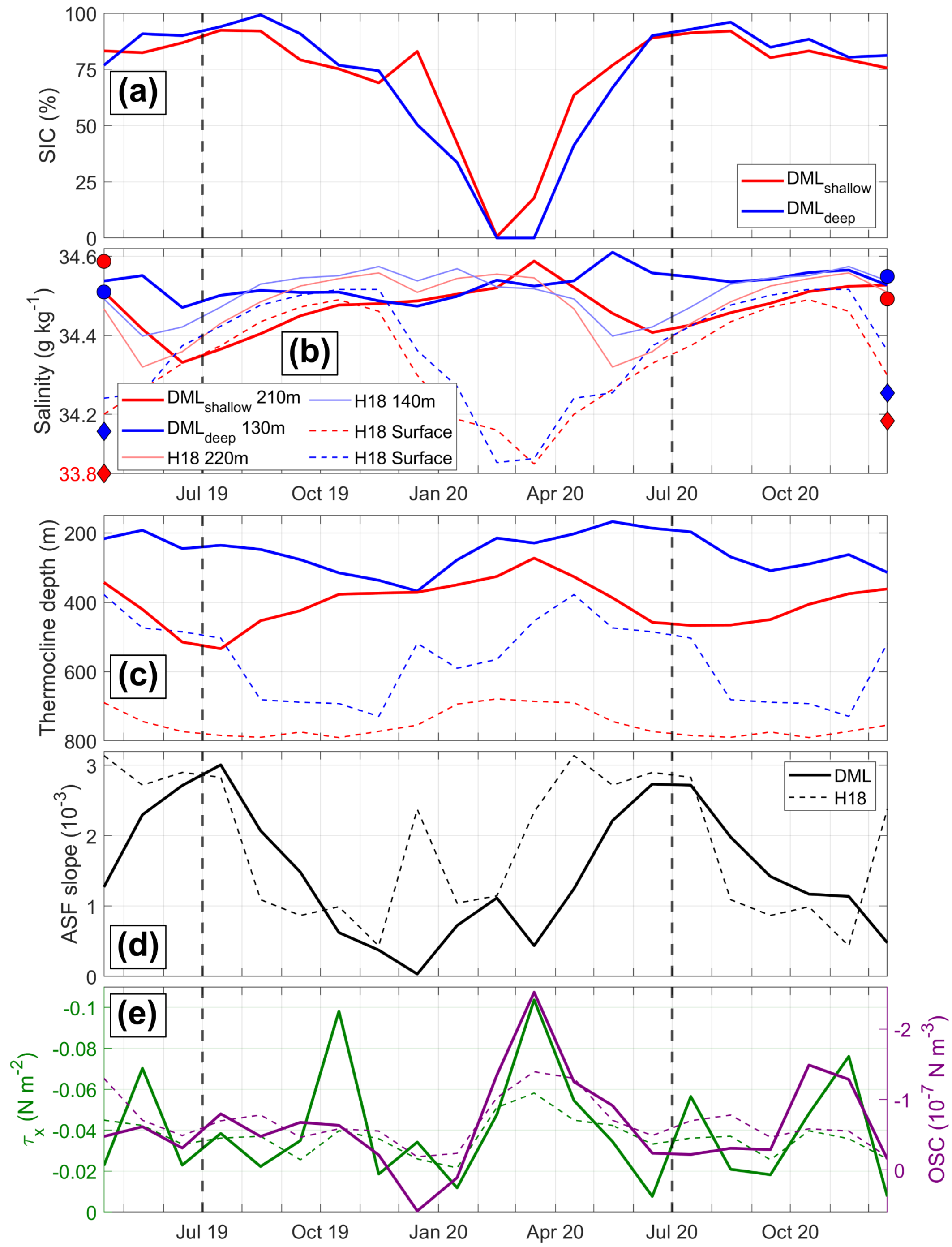

Figure 4. Monthly means of: (a) Sea ice concentration at both open-ocean mooring locations. (b) Salinity observed at the uppermost MicroCAT at both moorings (210 m at DML$_{\text{shallow}}$, 130 m at DML$_{\text{deep}}$), salinity from the H18 climatology over similar isobaths and at similar depths, and salinity from the H18 climatology over similar isobaths at the surface. Dots/diamonds indicate the salinity at the MicroCAT depth/surface from the CTD profiles of the deployment and recovery cruises. The red diamond on the left is off-scale. (c) Thermocline depth defined as the $-0.3\,^{\circ}$C isotherm at both moorings and from the H18 climatology over similar isobaths. (d) ASF slope estimated from the thermocline depths from panel c for the mooring data and the H18 climatology (Eqn. 1). (e) Regional zonal ocean stress (left axis) and ocean stress curl (right axis), averaged over 0−15°E and 69.5−70°S/67−69.5°S, respectively (solid lines), along with their climatology (2010-2021, dashed lines).

4.1.2 Velocity

At DML$_{\mathrm{shallow}}$, monthly mean velocities (Fig. 2b) show a surface-intensified current, which at 100 m is strongest in June in both years ($20\,\mathrm{cm\,s^{-1}}$). At 600-800 m, the velocity shows a vertical minimum throughout the length of the record. Toward the bottom, the velocity intensifies by $2\,\mathrm{cm\,s^{-1}}$. The vertical gradient, i.e. the baroclinic part, becomes more apparent in profiles when averaged over specific months (Fig. 5a): Toward the surface, the strongest vertical shear is observed in June. Below 500 m, there is smaller seasonal variability in the gradient. At DML$_{\mathrm{deep}}$ (Fig. 2d), velocities are generally smaller than at DML$_{\mathrm{shallow}}$ with maximum values of $10\,\mathrm{cm\,s^{-1}}$ at 20 m observed in May/June 2019 and April/May 2020. In contrast to DML$_{\mathrm{shallow}}$, the velocity at DML$_{\mathrm{deep}}$ continuously decreases toward the bottom (Fig. 5b). The seasonality of the upper-ocean vertical shear is weaker than at DML$_{\mathrm{shallow}}$ and strongest in March.

The estimated barotropic component (UBT_{obs}) at DML$_{\mathrm{shallow}}$ (Fig. 6b) is maximum ($6\,\mathrm{cm\,s^{-1}}$) in May/June 2019 and April 2020. At DML$_{\mathrm{deep}}$, the values are slightly smaller and the maximum occurs one month later than at DML$_{\mathrm{shallow}}$ in 2020, but not in 2019 when there is zero lag. The baroclinic velocity (UBC_{obs}) at DML$_{\mathrm{shallow}}$ at 100 m depth (Fig. 6d) shows a first seasonal maximum ($12\,\mathrm{cm\,s^{-1}}$) in April 2019. In 2020, a local maximum in April is followed by a higher seasonal maximum ($20\,\mathrm{cm\,s^{-1}}$) in June. The baroclinic velocity is close to $0\,\mathrm{cm\,s^{-1}}$ from December 2019 to February 2020. At DML$_{\mathrm{deep}}$ at 20 m depth (Fig. 6e), a maximum baroclinic velocity of $7\,\mathrm{cm\,s^{-1}}$ is observed in April in both years. Seasonal minima close to $0\,\mathrm{cm\,s^{-1}}$ occur in January and December 2020.

The ASF slope, derived from the thermocline depths at DML$_{\mathrm{shallow}}$ and DML$_{\mathrm{deep}}$ (Eqn. 1), is steepest in June/July (Fig. 4d). In 2020, this is around the same time as the maximum near-surface UBC_{obs} at DML$_{\mathrm{shallow}}$ (Fig. 6d), consistent with thermal wind balance. In 2019, however, a distinct maximum in ASF slope is found in July but no clear maximum in baroclinic velocity is observed (Fig. 6d). The weakest ASF slope occurs in December when the thermocline depths at the two moorings become equal due to a shoaling at DML$_{\mathrm{shallow}}$ and a deepening at DML$_{\mathrm{deep}}$ (Fig. 4c-d). Accordingly, UBC_{obs} at DML$_{\mathrm{shallow}}$ is close to its seasonal minimum between December and February (Fig. 6d). Despite some coinciding features, the ASF slope and the baroclinic velocities at the moorings are not directly comparable, since (i) most of baroclinic velocity shear occurs above the thermocline (Fig. 5), and (ii) the (assumed) linear ASF slope between the moorings may not represent the local ASF slope at the mooring locations.

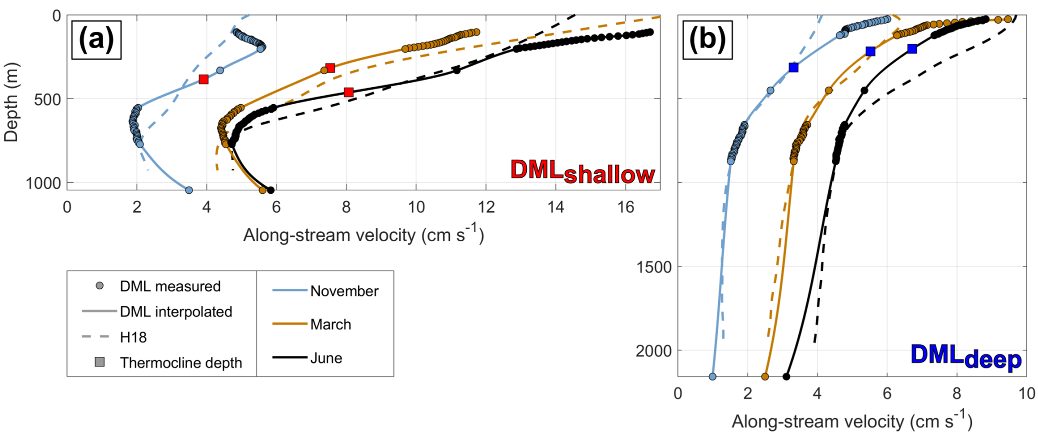

Figure 5. (a) Profiles of along-stream velocity at (a) $\mathrm{DML}_{\mathrm{shallow}}$ and (b) $\mathrm{DML}_{\mathrm{deep}}$, averaged over a three-month-window centered at three selected months. The velocities are vertically interpolated via a shape-preserving piecewise cubic interpolation. Additionally, the averages of the zonal baroclinic velocity profiles over the same time interval and for similar isobaths calculated from the H18 climatology are shown. For better comparability, the depth-constant UBT_{obs} has been added to the H18 profiles.

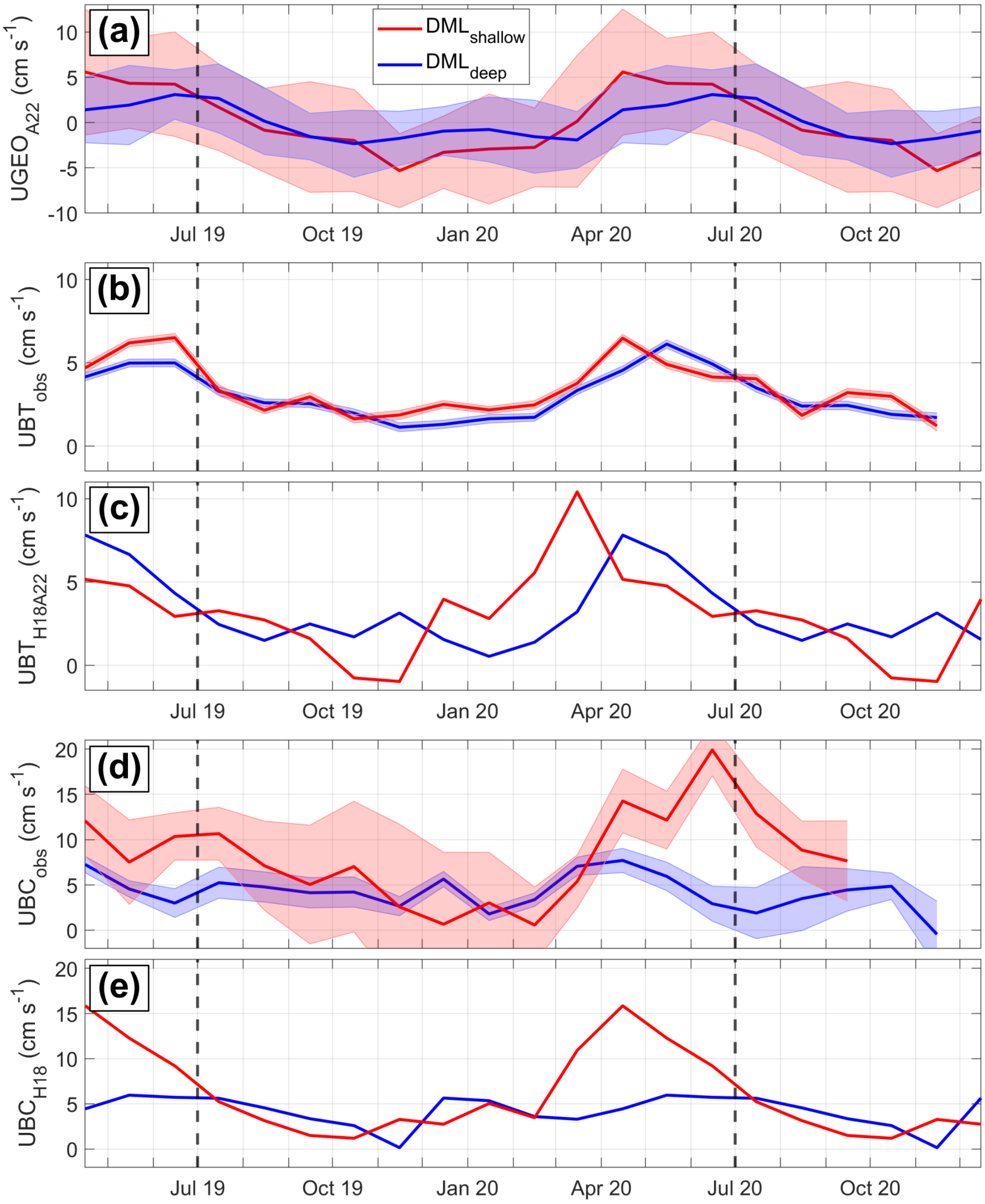

Figure 6. (a) Surface geostrophic velocity anomaly from A22 interpolated on the $\mathrm{DML}_{\mathrm{shallow}}$ and $\mathrm{DML}_{\mathrm{deep}}$ locations. (b) Barotropic velocity derived from mooring data. (c) Barotropic velocity derived from A22 and H18 data, obtained over the respective mooring isobaths. Shown are anomalies plus the respective time-mean of panel b. (d) Baroclinic velocity derived from mooring data at the uppermost ADCP bin depth (100 m at $\mathrm{DML}_{\mathrm{shallow}}$, 20 m at $\mathrm{DML}_{\mathrm{deep}}$). (e) Baroclinic velocity derived from the H18 climatology, taken over the mooring isobaths at the same depths as panel d. Details about the calculation of the error bars are given in Text S1 in Supporting Information S1.

4.1.3 Ocean Stress Forcing

To investigate the extent to which ocean stress contributes to the variability of the ASC at the moorings, we differentiate between regional (0−15°E, 67−70°S) and remote upstream (0−60°E and 50−70°S,) ocean stress and its curl.We further differentiate between the shallow (< 1000 m, more influenced by zonal ocean stress) and deep (> 1000 m, more influenced by ocean stress curl) regime suggested by Auger, Sallée, et al. (2022). We note that for both local and remote ocean stress, the modulation of the wind stress by sea ice causes the seasonal maximum in ocean stress to occur one month earlier than the maximum in wind stress.

Monthly mean regional ocean stress forcing does not show a distinct seasonal cycle during the mooring period, in contrast with the 12-year mean seasonality (Fig. 4e). The zonal ocean stress (meridionally averaged over 69.5−70°S, i.e. over the continental slope) is westward and strongest in October 2019 and March 2020. In April 2020, thermocline deepening starts at $\mathrm{DML}_{\mathrm{shallow}}$ (Fig. 4c), and a local maximum is found in the baroclinic velocity (Fig. 6e) at $\mathrm{DML}_{\mathrm{shallow}}$. This is consistent with coastal downwelling due to stronger onshore Ekman transport. However, no strong regional ocean stress occurred in early 2019 prior to the mooring deployment (not shown). In addition, the regional ocean stress maximum in October 2019 does not coincide with a thermocline deepening. The monthly mean regional ocean stress curl (meridionally averaged over 67−69.5°S, i.e. off the continental slope) is close to zero most of the time but has a clear maximum between February and April 2020 (Fig. 4e). Estimated Ekman upwelling of $w_{Ek} = \frac{OSC}{\rho_0 f} = 4\,\mathrm{m\,month^{-1}}$ (with ocean stress curl $OSC = -0.2 \times 10^{-7}\,\mathrm{N\,m^{-3}}$, background density $\rho_0 = 1028\,\mathrm{kg\,m^{-3}}$, Coriolis parameter $f = -1.36 \times 10^{-4}\,\mathrm{s^{-1}}$) can, however, not explain the thermocline shoaling and upper-ocean salinity increase observed at $\mathrm{DML}_{\mathrm{deep}}$ between January and May 2020 (Fig. 4b-c). Overall, the poor agreement between UBC_{obs} at $\mathrm{DML}_{\mathrm{shallow}}$ and regional ocean stress forcing indicates that the latter is not the main driver of the baroclinic velocity seasonality. This will be further investigated in section 4.2.

To investigate the forcing of the barotropic ASC, we correlate UBT_{obs} at $\mathrm{DML}_{\mathrm{shallow}}$ with zonal ocean stress (Fig. 7a) and UBT_{obs} at $\mathrm{DML}_{\mathrm{deep}}$ with ocean stress curl (Fig. 7b). The highest negative correlations are found along the East-Antarctic coast at 30−60°E with UBT_{obs} lagging the ocean stress by one month. The patterns are similar when correlating UBT_{obs} at $\mathrm{DML}_{\mathrm{deep}}$ with zonal ocean stress or UBT_{obs} at $\mathrm{DML}_{\mathrm{shallow}}$ with ocean stress curl. Therefore, the bands of high correlation are independent of the method differentiating the regimes from Auger, Sallée, et al. (2022). In contrast to the regional forcing (Fig. 4e), the remote ocean stress and its curl exhibit a distinct seasonal cycle during the mooring period over the areas of highest correlations along East Antarctica, similar to the multi-year climatology (Fig. 7c). Strong westward ocean stress and negative ocean stress curl seasonally increase the cross-shore SSH gradient in autumn (March-May). This gradient travels westward through coastal Kelvin waves (Webb et al., 2022), explaining the seasonal variability of the barotropic flow at the moorings (Fig. 6b). This can also explain the observed interannual variability like the maximum occurring later in 2019 than in 2020 in remote ocean stress (Fig. 7c) and UBT_{obs} (Fig. 6b).

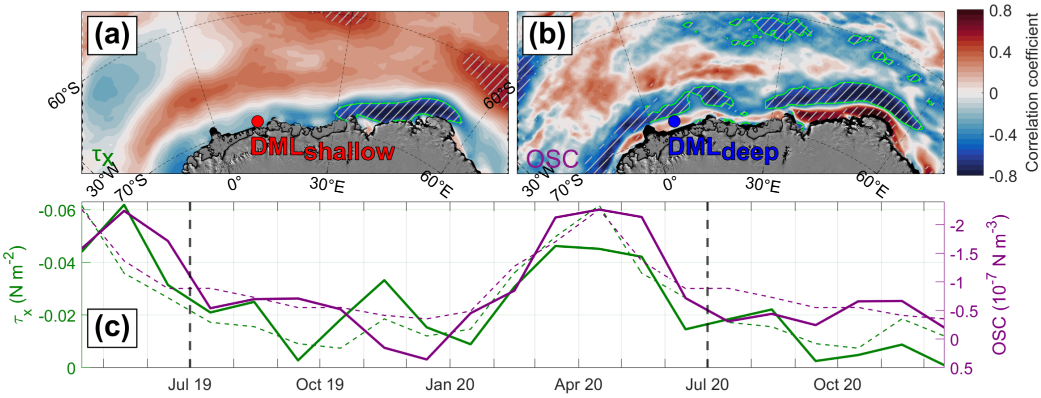

Figure 7. Correlation maps of (a) barotropic velocity UBT_{obs} at $\mathrm{DML_{shallow}}$ from Fig. 6b, lagged by one month, and zonal ocean stress, and (b) barotropic velocity UBT_{obs} at $\mathrm{DML_{deep}}$ from Fig. 6b, lagged by one month, and ocean stress curl at every grid point. Hatched areas indicate a significance of at least 95 %, and green lines mark areas of a correlation of at least -0.5 east of the prime meridian. The background satellite image is taken from Haran et al. (2018). (c) Zonal ocean stress (left axis) and ocean stress curl (right axis) averaged over 0−60°E and 50−70°S where the correlations from panels a and b, respectively, are at least -0.5, along with their climatology (2010-2021, dashed lines).

4.2 Seasonal Cycle from Auxiliary Data Sets

Our new mooring data show different processes governing the seasonal hydrographic and dynamic variability at $\mathrm{DML_{shallow}}$ and $\mathrm{DML_{deep}}$. As we will demonstrate in this section, these processes are consistent with the H18 data, providing information above the uppermost moored instruments and over multiple isobaths. We next use these data to investigate the forcing of the baroclinic seasonality and the delay in salinity and thermocline depth seasonality observed between $\mathrm{DML_{shallow}}$ and $\mathrm{DML_{deep}}$ in more detail.

4.2.1 The Role of ASW for the Hydrographic Seasonality

In both the mooring records (Fig. 4b) and the H18 data set (Fig. S2 in Supporting Information S1), the seasonal subsurface salinity minimum occurs later over deeper isobaths than over shallow isobaths. For the mooring isobaths, the delay in the H18 data increases from zero at the surface, where the salinity is determined directly by freshwater input from sea ice melt, to five months at 400 m depth. The freshwater content integrated down to this depth illustrates that the offshore delay in salinity minimum is a robust feature across multiple isobaths (Fig. 8a): in March, fresh ASW accumulates at the coast, and in the subsequent months, the ASW spreads and deepens offshore, delaying the timing of maximum offshore freshwater content well into the freezing season. This is most pronounced over isobaths shallower than 2000 m. As the offshore ASW spreading and deepening displaces WW to greater depths, the deepest thermocline follows the highest freshwater content and thus shows a similar offshore delay (Fig. S3 in Supporting Information S1). This is consistent with the mooring observations and explains the different seasonalities of and the robust link between salinity and thermocline depth over the two isobaths (Fig. 2a/c).

The seasonal offshore spreading and deepening of ASW moves the secondary front and the ASF, causing the maximum surface baroclinic velocity from H18 to move toward deeper isobaths throughout the season (Fig. 8b). This is again clearest over isobaths shallower than 2000 m. Consequently, over the mooring isobaths, time series of UBC_{H18} (Fig. 6e) agree well with UBC_{obs} (Fig. 6d), apart from the maximum occurring two months later at the $\mathrm{DML_{shallow}}$ mooring in 2020.

Next, we use the H18 data to estimate the contribution of the baroclinic component to the surface geostrophic velocity from A22. At the location of $\mathrm{DML_{shallow}}$, the surface geostrophic velocity shows a seasonal amplitude of $10\,\mathrm{cm\,s^{-1}}$ and a maximum in April (Fig. 6a). At the $\mathrm{DML_{deep}}$ location, the seasonal amplitude is $5\,\mathrm{cm\,s^{-1}}$ and the maximum occurs in June (Fig. 6a). This delay becomes clearer in time-latitude space, in which the surface geostrophic velocity seasonality from A22 at 6°E also shows an offshore delay (Fig. 8c). This time lag, however, is somewhat smaller than in the H18 surface baroclinic velocity (Fig. 8b). The barotropic velocity anomaly (UBT_{H18A22}) is then estimated as the difference between the A22 surface geostrophic and H18 surface baroclinic velocity (Fig. 8d). A moderate offshore delay is still visible in the seasonal cycle of UBT_{H18A22}, with a phase shift of one to two months between the mooring sites (Fig. 6d). Given the uncertainties in both data sets that UBT_{H18A22} is derived from, we cannot conclude if this remaining phase shift is realistic (see section 5).

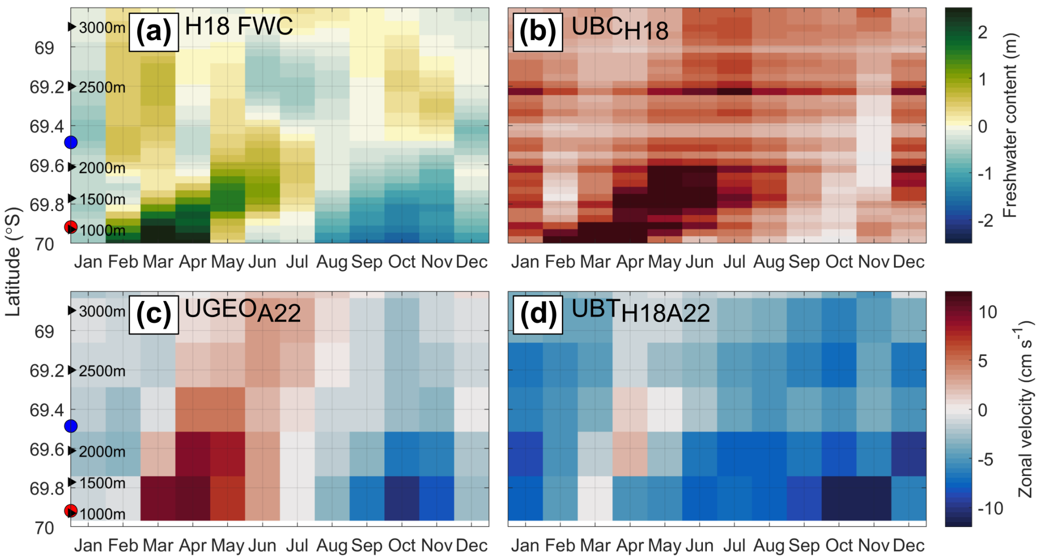

Figure 8. Hovmöller diagrams of (a) depth-integrated freshwater content within the upper 400 m referenced to a salinity of 34.6 g kg^{-1} from H18, (b) zonal surface baroclinic velocity derived from H18, (c) zonal surface geostrophic velocity anomaly from A22 at 6°E, (d) zonal barotropic velocity anomaly obtained by taking panel c minus panel b. The red/blue dots indicate the isobath of $\mathrm{DML_{shallow}}/\mathrm{DML_{deep}}$.

4.2.2 Implications for ASF/ASC Dynamics

The coastal freshwater content maximum in March (Fig. 8a) and the resulting surface baroclinic velocity (Fig. 8b) cannot originate from seasonally increased ocean stress (Fig. 4e). Instead, it is caused by the freshening of upper-ocean water masses through seasonal sea ice melt and their concurrent accumulation at the coast. These results align with observed seasonal cycles in hydrography (Fig. 2a and 4b-d) and baroclinic velocity (Fig. 5a, Fig. 6d) at $\mathrm{DML_{shallow}}$, despite a weak seasonality in local zonal ocean stress (Fig. 4e). Therefore, the mooring and H18 data are consistent in that seasonal freshwater input from sea ice melt is an essential forcing of the surface baroclinic velocity seasonality and magnitude, independent of any seasonality in ocean-stress-driven coastal downwelling.

The velocity shear toward the surface in March and June at the upper ADCPs of both moorings (reaching 110 m higher than the uppermost MicroCATs, Fig 5) indicates the presence of the secondary front between ASW and WW at the sites. Although the strongest upper-ocean velocity shear at $\mathrm{DML_{shallow}}$ is found in March in the H18 data, and in June in the mooring data, the shapes of the observed velocity profiles generally agree with the ones from H18 over similar isobaths. In addition, the offshore delay in thermocline depth maximum and salinity minimum at $\mathrm{DML_{deep}}$ is consistent between the mooring and H18 data (Fig. 4b-c, Fig. 8a, Fig. S3 in Supporting Information S1). We thus infer that the offshore spreading and deepening of ASW identified in Fig. 8a also takes place at the mooring longitude of 6°E.

We propose that eddy overturning, as demonstrated by Si et al. (2023) using an eddy-resolving model, drives the observed offshore delay in seasonal freshwater content (Fig 8a): after the phase of the freshest ASW at the coast in March and with slackening local and remote ocean stress forcing, eddy overturning acts to relax the secondary front, consistent with large eddy growth rate estimates from January to June (Hattermann, 2018). Thereby, the fresh signal spreads and deepens offshore during the course of the following months, causing the observed delay in offshore thermocline depth (Fig. 4c) and salinity (Fig. 4b) seasonality. Eddy overturning also transports salty WW from offshore toward the coast, contributing to the decrease in coastal freshwater content after June (Fig. 8a) in addition to convection.

We also identify some differences between the mooring records and the H18 data: the thermocline in the H18 data is consistently 200 m deeper than in the mooring observations (Fig. 4c). As a result of this vertical offset, the seasonal salinity minimum observed in December at 130 m and 810 m at $\mathrm{DML_{deep}}$ (Fig. 2c) shows up in November in the H18 data below 400 m, but not above (Fig. S2b in Supporting Information S1). In addition to this vertical offset, the seasonal extremes of salinity at $\mathrm{DML_{shallow}}$ (Fig. 4b), of the thermocline depth (Fig. 4c) and of the ASF slope (Fig. 4d) occur one to two months earlier in the H18 data than in the mooring observations. Advection of water masses within the ASC, as suggested by Graham et al. (2013), may explain the alongshore thermocline deepening, but not the delayed seasonal extremes at 6°E compared to 17°W. With the data sets being obtained in different years, we cannot conclude if the described offsets are a robust feature or the result of interannual variability, and if alongshore advection plays a role.

4.3 ASF/ASC Variability and Inflow below Fimbulisen

To assess the role of the variability of the ASF/ASC system on the deep inflow of mWDW into the cavity of Fimbulisen, we now compare the open-ocean mooring data from $DML_{shallow}$/DML_{deep} with the concurrent sub-ice-shelf mooring data from $M1_{lower}$ and $M3_{lower}$ (Fig. 1a). The open-ocean moorings are roughly 200 km upstream of Fimbulisen, but supported by the agreement between the the mooring and H18 data, we assume that the seasonality does not change considerably over this distance.

Mooring M1 is located on the main sill that connects the cavity to the open ocean (Fig. 1a). This sill is at 560 m depth and is directed across the continental slope. Here, the velocity alternates seasonally between a period of flow into the cavity between July/August and February and a period of flow out of the cavity between March and June/July (Fig. 9a). The seasonality of the cavity inflow at $M1_{lower}$ anticorrelates with the ASC strength: the current is directed into the cavity during periods of a weak barotropic and baroclinic (at 330 m, i.e. the depth of the velocity measuring instrument closest to the WDW core at $DML_{shallow}$) ASC, while it is directed out of the cavity during periods of a strong ASC. At $M3_{lower}$, located in the east of Fimbulisen on a second sill that is 480 m deep and directed more along the continental slope (Fig. 1a), the connection between inflow and the ASC strength is the opposite, i.e. inflow occurs during periods of a strong ASC, and outflow - or weak inflow - during periods of a weak ASC (Fig. 9a).

The temperature at $M1_{lower}$ (Fig. 9b) does not show a clear seasonality during the mooring period, and we do not find a significant correlation to the seasonally varying thermocline depth (Fig. 9c) on time scales from days to months. Instead, the $M1_{lower}$ temperature lies around the surface freezing point most of the time, showing irregular episodes with higher temperatures of up to almost 0 °C. These temperature extremes are not, as one would expect, associated with a particularly shallow thermocline and high WDW temperatures at $DML_{shallow}$. Similarly, the cavity temperature at $M3_{lower}$ does not correlate with the thermocline depth: the lowest temperatures occur shortly after the minimum in thermocline depth in March 2020. Interestingly, despite the opposing inflow and outflow velocities at the two sub-ice-shelf mooring sites, peak temperatures occur simultaneously at $M1_{lower}$ and $M3_{lower}$ in August/September 2019, suggesting a forcing driving mWDW inflow over a larger area. At most times, however, the temperatures at M1$_{lower}$ and M3$_{lower}$ appear to be unrelated. Further interpretations of the observed variability below Fimbulisen with regard to the ASC are given in section 5.

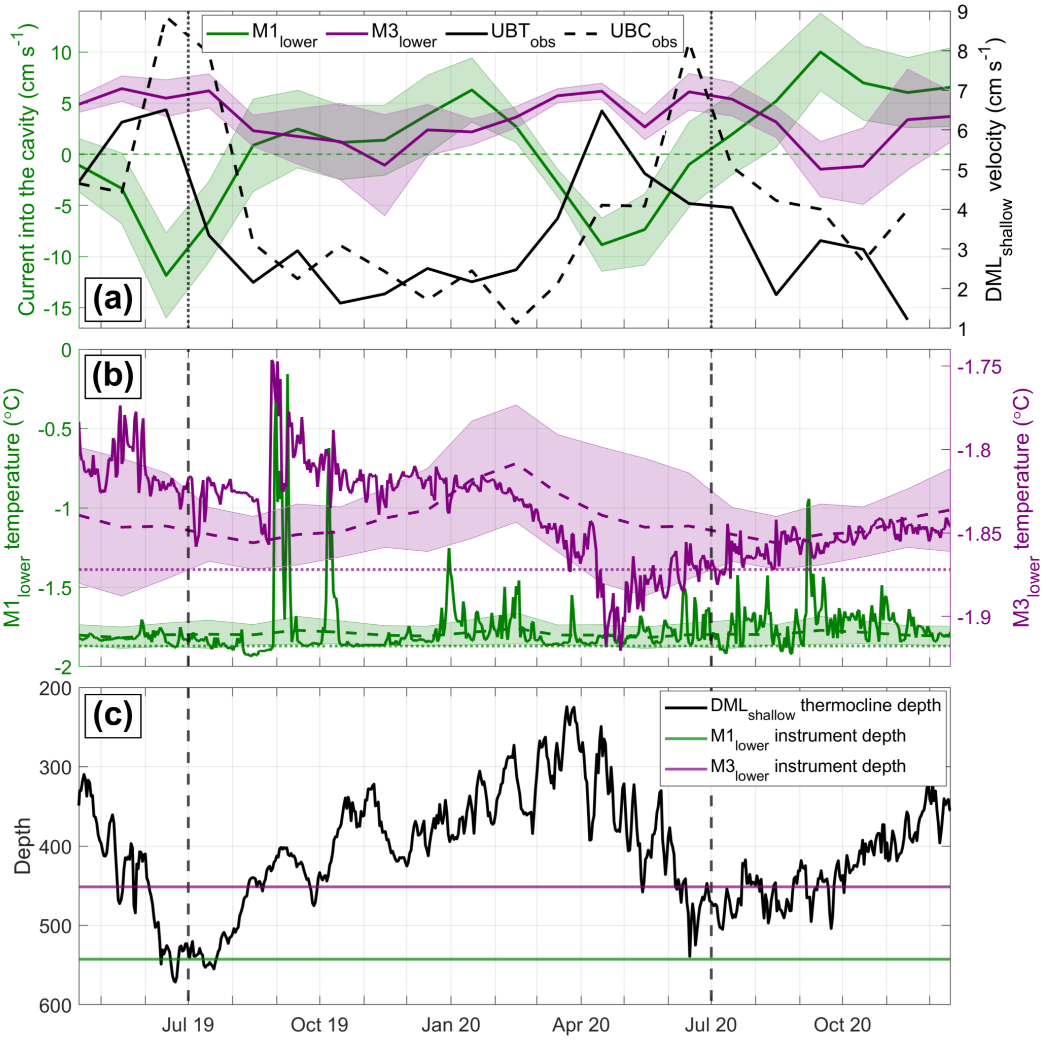

Figure 9. (a) Monthly averages of the currents at M1$_{lower}$ and M3$_{lower}$ (left axis), rotated into the cavity as described in section 3, together with UBT_{obs} (same as the red line in Fig. 6b) and UBC_{obs} at 330 m depth at DML$_{shallow}$ (right axis). Envelopes denote the standard deviation of the monthly climatology (2010-2021). (b) Daily averages of in-situ temperature at M1$_{lower}$ (left axis) and M3$_{lower}$ (right axis, solid lines), along with their monthly climatology and standard deviation (2010-2021, dashed lines and envelope, respectively). Dotted lines are the surface freezing temperature for a salinity of 34.4 g kg^{-1} (c) Daily average of the thermocline depth at DML$_{shallow}$ (same data as the solid red line in Fig. 4c), together with the mean depths of M1$_{lower}$ and M3$_{lower}$.

5 Discussion

Our findings - the seasonal spreading of ASW offshore and the role of freshwater input - help to refine the seasonality of the baroclinic component of the ASF/ASC, complementing previous findings. Based on our observations, we summarize the seasonality in three phases (Fig. 10):

In November (Fig. 10a), the ASF is weak (Fig. 10e), as the thermocline is shoaling at $\mathrm{DML_{shallow}}$ and deepening at $\mathrm{DML_{deep}}$. At the same time, the absence of ASW results in a weak meridional density gradient at all depths and thus a baroclinic velocity minimum (Fig. 10f and Fig. 5a). Sea ice melt from September and on provides freshwater to the upper ocean and leads to the formation of ASW (Fig. 10d). The regional ocean stress is weak (Fig. 10g), resulting in reduced ASF steepening.

In March (Fig. 10b), sea ice concentration and surface salinity are around their seasonal minima (Fig. 10d), and ASW has been accumulated at the coast to form a secondary front, resulting in an increase in upper-ocean baroclinic velocity (Fig. 10f and Fig. 5a). Maximum ocean stress (Fig. 10g) further aids in steepening the isopycnals. Due to the large density difference between ASW and WW, strong eddy overturning may happen at the secondary front.

The secondary front weakens in June (Fig. 10c) since no new ASW is formed after March. The remainder of the ASW spreads and deepens offshore, possibly via eddy overturning of the secondary front when ocean stress forcing weakens (Fig. 10g). Brine release from sea ice formation (Fig. 10d) along the coast as of March also starts to erode the ASW through convection, as described in section 4.1.1 and corroborated by small vertical salinity gradients between surface and depth between July and November in the H18 data (Fig. 4b). The ASF is around its steepest state, as the thermocline deepens at $\mathrm{DML_{shallow}}$ and shoals at $\mathrm{DML_{deep}}$ (Fig. 10e). The maximum upper-ocean baroclinic velocity is reached around April (H18) to June (mooring data, Fig. 10f and Fig. 5a). After this phase, weak ocean stress and further brine release cause a relaxation of the ASF and form the transition back to the first phase (Fig. 10a).

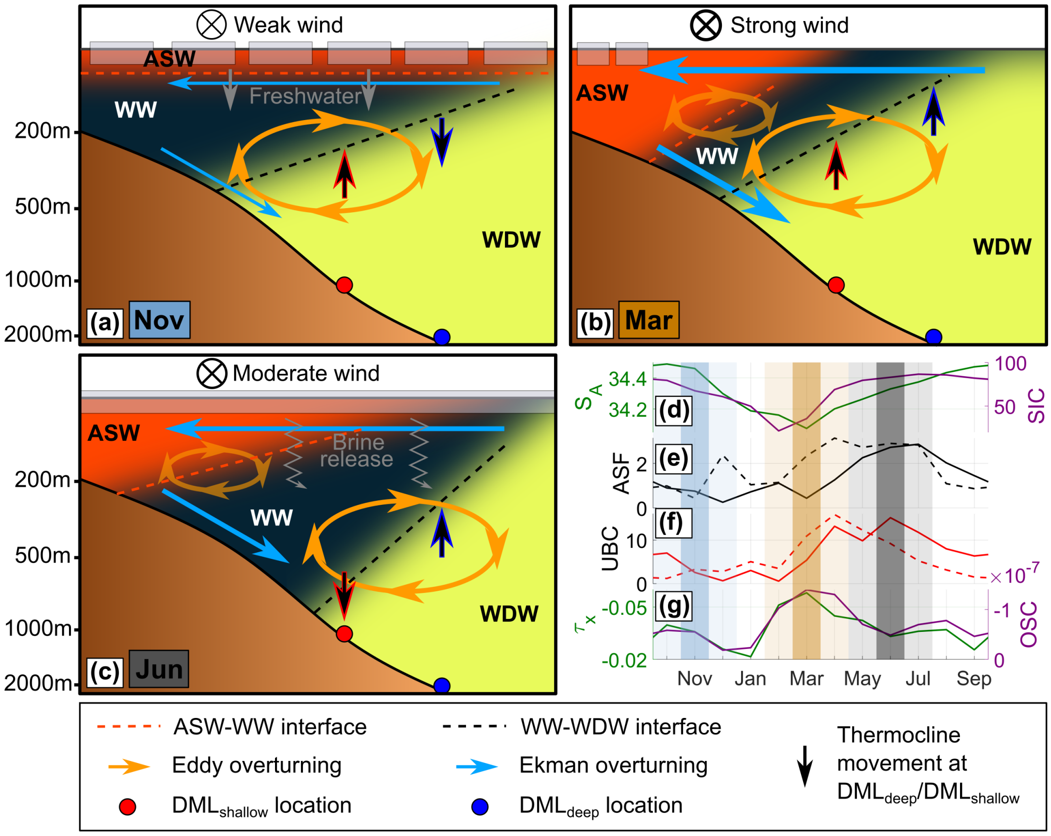

Figure 10. Sketches of different phases of the baroclinic seasonal cycle during (a) November, (b) March, and (c) June. Seasonal time series of relevant variables, i.e. (d) surface absolute salinity over $DML_{shallow}$ isobath from H18 data and sea ice concentration climatology (2010-2021) at $DML_{shallow}$, (e) mean seasonal ASF slope between DML_{deep} and $DML_{shallow}$ from mooring observations and H18 data, (f) mean seasonal mooring and H18 baroclinic velocity at $DML_{shallow}$ at 100 m depth, and (g) zonal ocean stress (left axis) and ocean stress curl (right axis) climatology (2010-2021) averaged over $0-15°$E and $69.5-70°$S/$67-69.5°$S, respectively. Colored shadings indicate the timing of the sketches in panels a-c.

We find the barotropic component of the ASC at 6°E to be forced by upstream ocean stress, consistent with results from earlier studies (Núñez-Riboni & Fahrbach, 2009; Graham et al., 2013; Le Paih et al., 2020). However, in contrast to Núñez-Riboni and Fahrbach (2009) at the prime meridian, we do not find a conclusive offshore lag in the seasonality of the barotropic component in the mooring records or H18 data. Instead, we observe a clear offshore lag in subsurface salinity, thermocline depth, and resulting surface baroclinic velocity seasonality in both data sets. Interestingly, the moorings from Núñez-Riboni and Fahrbach (2009) show a delay of one to three months in long-term temperature seasonality at 200 m and 700 m depth over the 3500 m isobath compared to the 2000 m isobath (Fig. S4 in Supporting Information S1 and Fig. 5 in Le Paih et al., 2020). This is in agreement with our observed temperature seasonalities at the DML moorings and therefore consistent with the offshore lag in thermocline depth seasonality at 6°E and 17°W. In fact, Núñez-Riboni and Fahrbach (2009) assumed the depth-weighted average of the total observed velocity to be the barotropic component, to which the observed offshore delay in ASC strength was attributed. With this approach, however, the barotropic velocity may still contain a significant baroclinic component. Our study shows that the largest offshore delay occurs in the baroclinic component and not, or at least to a lesser extent, in the barotropic component. We therefore suggest that sea ice causes the observed offshore delay in the ASC seasonality mainly in the baroclinc component through seasonal meltwater input and offshore spreading.

There is an apparent link between seasonal variations in both the baroclinic and barotropic ASC strength and flow into the Fimbulisen cavity. While not investigated here in detail, this link may include an intricate interplay between the local bathymetry at the sills (Nøst, 2004; Eisermann et al., 2020), a seasonal counter-current at depth (Heywood et al., 1998; Smedsrud et al., 2006; Núñez-Riboni & Fahrbach, 2009; Chavanne et al., 2010), bottom Ekman transport anomalies (Smedsrud et al., 2006; Núñez-Riboni & Fahrbach, 2009) and potential vorticity constraints (Daae et al., 2017; Wåhlin et al., 2020; Steiger et al., 2022). The absence of a clear relation between the observed offshore thermocline depth and the inflow temperature is surprising and points to that warm inflows are rather controlled by local sub-monthly variations in thermocline depth, forced by variability in winds, sea ice and SSH (Lauber, Hattermann, et al., 2023). In addition, the internal cavity circulation likely also affects the hydrography at the sill, and the seasonal oceanic variability below Fimbulisen will be investigated in more detail in a follow-up study.

6 Summary and Conclusions

Our combined analyses of new mooring observations, climatological hydrography, and satellite-derived surface geostrophic currents have shown that the cross-slope processes controlling the ASF/ASC seasonality are consistent along the DML coast across independent data sets over multiple years in isobath-depth space: in the mooring data at 6°E, we found the seasonal upper-ocean salinity minimum and thermocline depth maximum to occur up to six months later over 2200 m isobath than over 1100 m isobath. The same feature occurs in climatological hydrography at 17°W and translates onto satellite-derived surface geostrophic currents. Our analyses suggest that this offshore delay originates from a seasonal offshore spreading of ASW through eddy overturning at the ASF and the secondary front above. We found the seasonal production of ASW via sea ice melt and subsequent shoreward accumulation to govern the timing of the baroclinic ASC maximum, while variations in ocean stress forcing can additionally modulate the baroclinic seasonality. These findings led us to define three distinct phases describing the seasonality of the ASF/ASC (Fig. 10). These phases may be regarded as generally valid in the Fresh Shelf regime along the East Antarctic coast. Below Fimbulisen, seasonal flow into and out of the cavity is associated with seasonal variations in ASC strength, but the inflow temperature does not follow the offshore thermocline depth. The results of this study contribute to a better understanding of the seasonal variability of the ASF/ASC system along the DML coast and will aid in assessing the impacts of a changing climate on the ASF/ASC.

Data Availability Statement

The DML mooring data will be made available via `https://data.npolar.no` during the revisions. The sub-ice-shelf mooring data will be updated at `https://doi.org/10.21334/npolar.2023.4a6c36f5` (Lauber, de Steur, et al., 2023). The H18 climatology is available at `https://doi.org/10.1594/PANGAEA.893199` (Hattermann & Rohardt, 2018). Sea surface height is available at `https://doi.org/10.17882/81032` (Auger et al., 2021). Sea ice concentration is available at `https://doi.org/10.5067/MPYG15WAA4WX` (DiGirolamo et al., 2022) and sea ice velocity at `https://doi.org/10.5067/INAWUWO7QH7B` (Tschudi et al., 2019). ERA5 wind data are available at `https://doi.org/10.24381/cds.f17050d7` (Hersbach et al., 2023). Bathymetric data are available at `https://doi.org/10.1594/PANGAEA.937574` (Dorschel et al., 2022).

Acknowledgments

This research was funded by the Research Council of Norway through the KLIMAFORSK program (iMelt, 295075). The DML moorings were financed and installed by the Norwegian Polar Institute. The installation of the M1 and M3 moorings through the project "ICE Fimbulisen – top to bottom" was financed by the Centre for Ice, Climate and Ecosystems (ICE), Norwegian Polar Institute (NPI). The latter moorings were maintained by NPI through ICE, the Norwegian Antarctic Research Expedition (IceRises 759, 3801-103), and iMelt. J.L. was funded by iMelt, and T.H. by the European Union's Horizon 2020 programme (CRiceS, 101003826). We thank the sections Maritime and Technical Support and Operations and Logistics Antarctica from NPI for all their support involving the moorings.

References

Armitage, T. W. K., Kwok, R., Thompson, A. F., & Cunningham, G. (2018). Dynamic Topography and Sea Level Anomalies of the Southern Ocean: Variability and Teleconnections. *Journal of Geophysical Research: Oceans*, *123*, 613-630.

Auger, M., Prandi, P., & Sallée, J.-B. (2022). Southern ocean sea level anomaly in the sea ice-covered sector from multimission satellite observations. *Scientific Data*, *9*(70), 1-10.

Auger, M., Prandi, P., & Sallée, J.-B. (2021). Daily Southern Ocean Sea Level Anomaly And Geostrophic Currents from multimission altimetry, 2013-2019. *SEANOE*. (URL: `https://doi.org/10.17882/81032`. Last accessed: 13.06.2022)

Auger, M., Sallée, J.-B., Prandi, P., & Naveira Garabato, A. C. (2022). Subpolar Southern Ocean Seasonal Variability of the Geostrophic Circulation From Multi-Mission Satellite Altimetry. *Journal of Geophysical Research: Oceans*, *127*, 1-16.

Chavanne, C. P., Heywood, K. J., Nicholls, K. W., & Fer, I. (2010). Observations of the Antarctic Slope Undercurrent in the southeastern Weddell Sea. *Geophysical Research Letters*, *37*(L13601), 1-5. Retrieved from `https://agupubs.onlinelibrary.wiley.com/doi/abs/10.1029/2010GL043603` doi: https://doi.org/10.1029/2010GL043603

Daae, K., Hattermann, T., Darelius, E., & Fer, I. (2017). On the effect of topography and wind on warm water inflow — An idealized study of the southern Weddell Sea continental shelf system. *Journal of Geophysical Research: Oceans*, *122*(3), 2622-2641. Retrieved from `https://agupubs.onlinelibrary.wiley.com/doi/abs/10.1002/2016JC012541` doi:

https://doi.org/10.1002/2016JC012541

Deacon, G. (1979). The Weddell gyre. *Deep Sea Research Part A. Oceanographic Research Papers*, *26*(9), 981-995. Retrieved from `https://www.sciencedirect.com/science/article/pii/019801497990044X` doi: 10.1016/0198-0149(79)90044-X

DiGirolamo, N., Parkinson, C. L., Cavalieri, D. J., Gloersen, P., & Zwally, H. J. (2022). Sea Ice Concentrations from Nimbus-7 SMMR and DMSP SSM/I-SSMIS Passive Microwave Data, Version 2. [March 2019 to January 2021, 180°W - 180°E and 90°S - 40°S]. *NASA National Snow and Ice Data Center Distributed Active Archive Center. Boulder/Colorado/USA.*. (URL: `https://doi.org/10.5067/MPYG15WAA4WX`. Last accessed: 21.11.2022)

Dorschel, B., Hehemann, L., Viquerat, S., Warnke, F., Dreutter, S., Schulze Tenberge, Y., … Arndt, J. E. (2022). The International Bathymetric Chart of the Southern Ocean Version 2 (IBCSO v2). *PANGAEA.* (URL: `https://doi.org/10.1594/PANGAEA.937574`. Last accessed: 15.06.2022)

Dorschel, B., Hehemann, L., Viquerat, S., Warnke, F., Dreutter, S., Tenberge, Y. S., … others (2022). The International Bathymetric Chart of the Southern Ocean Version 2. *Scientific Data*, *9*(275), 1-13.

Dotto, T. S., Naveira Garabato, A., Bacon, S., Tsamados, M., Holland, P. R., Hooley, J., … Meredith, M. P. (2018). Variability of the Ross Gyre, Southern Ocean: Drivers and Responses Revealed by Satellite Altimetry. *Geophysical Research Letters*, *45*, 6195-6204.

Eisermann, H., Eagles, G., Ruppel, A., Smith, E. C., & Jokat, W. (2020). Bathymetry Beneath Ice Shelves of Western Dronning Maud Land, East Antarctica, and Implications on Ice Shelf Stability. *Geophysical Research Letters*, *47*(12), 1-10.

Gordon, A., Martinson, D., & Taylor, H. (1981). The wind-driven circulation in the Weddell-Enderby Basin. *Deep Sea Research Part A. Oceanographic Research Papers*, *28*(2), 151-163. Retrieved from `https://www.sciencedirect.com/science/article/pii/019801498190087X` doi: 10.1016/0198-0149(81)90087-X

Graham, J. A., Heywood, K. J., Chavanne, C. P., & Holland, P. R. (2013). Seasonal variability of water masses and transport on the Antarctic continental shelf and slope in the southeastern Weddell Sea. *Journal of Geophysical Research: Oceans*, *118*(4), 2201-2214.

Haran, T., Klinger, M., Bohlander, J., Fahnestock, M., Painter, T., & Scambos, T. (2018). MEaSUREs MODIS Mosaic of Antarctica 2013-2014 (MOA2014) Image Map, Version 1. [moa750_2014_hp1_v01.tif]. *NASA National Snow and Ice Data Center Distributed Active Archive Center. Boulder/Colorado/USA.*. (URL: https://nsidc.org/data/NSIDC-0730/versions/1. Last accessed: 25.08.2021)

Hattermann, T. (2018). Antarctic Thermocline Dynamics along a Narrow Shelf with Easterly Winds. *Journal of Physical Oceanography*, *48*(10), 2419-2443.

Hattermann, T., Nøst, O. A., Lilly, J. M., & Smedsrud, L. H. (2012). Two years of oceanic observations below the Fimbul Ice Shelf, Antarctica. *Geophysical Research Letters*, *39*(12), 1-6.

Hattermann, T., & Rohardt, G. (2018). Kapp Norvegia Antarctic Slope Front climatology. *Alfred Wegener Institute, Helmholtz Centre for Polar and Marine Research, Bremerhaven, PANGAEA.* (URL: https://doi.org/10.1594/PANGAEA.893199. Last accessed: 24.08.2022)

Hersbach, H., Bell, B., Berrisford, P., Biavati, G., Horányi, A., Muñoz Sabater, J., … Thépaut, J.-N. (2023). ERA5 monthly averaged data on single levels from 1940 to present. *Copernicus Climate Change Service (C3S) Climate Data Store (CDS).* (URL: https://doi.org/10.24381/cds.f17050d7. Last accessed: 02.11.2021)

Heywood, K. J., Locarnini, R. A., Frew, R. D., Dennis, P. F., & King, B. A. (1998). Transport and Water Masses of the Antarctic Slope Front System in The Eastern Weddell Sea. In S. S. Jacobs & R. F. Weiss (Eds.). *Ocean, ice, and atmosphere: Interactions at the Antartic continental margin, Antarctic Research Series.*, *75*, 203-214. Retrieved from https://agupubs.onlinelibrary.wiley.com/doi/abs/10.1029/AR075p0203 (Washington, DC: American Geophysical Union) doi: https://doi.org/10.1029/AR075p0203

Huneke, W. G. C., Morrison, A. K., & Hogg, A. M. (2022). Spatial and Subannual Variability of the Antarctic Slope Current in an Eddying Ocean–Sea Ice Model. *Journal of Physical Oceanography*, *52*(3), 347 - 361. Retrieved from https://journals.ametsoc.org/view/journals/phoc/52/

3/JPO-D-21-0143.1.xml doi: https://doi.org/10.1175/JPO-D-21-0143.1

Isachsen, P. E., LaCasce, J. H., Mauritzen, C., & Häkkinen, S. (2003). Wind-Driven Variability of the Large-Scale Recirculating Flow in the Nordic Seas and Arctic Ocean. *Journal of Physical Oceanography*, *33*(12), 2534 - 2550. Retrieved from https://journals.ametsoc.org/view/journals/phoc/33/12/1520-0485_2003_033_2534_wvotlr_2.0.co_2.xml doi: 10.1175/1520-0485(2003)033⟨2534:WVOTLR⟩2.0.CO;2

Jacobs, S. S. (1991). On the nature and significance of the Antarctic Slope Front. *Marine Chemistry*, *35*(1), 9-24. doi: https://doi.org/10.1016/S0304-4203(09)90005-6

Lauber, J., de Steur, L., Hattermann, T., & Nøst, O. A. (2023). Daily averages of physical oceanography and current meter data from sub-ice-shelf moorings M1, M2 and M3 at Fimbulisen, East Antarctica since 2009. *Norwegian Polar Institute, Tromsø*. (URL: https://doi.org/10.21334/npolar.2023.4a6c36f5. Last accessed: 07.07.2023)

Lauber, J., Hattermann, T., de Steur, L., Darelius, E., Auger, M., Nøst, O., & Moholdt, G. (2023). Warming beneath an East Antarctic ice shelf due to increased subpolar westerlies and reduced sea ice. *Nature Geoscience*. doi: 10.1038/s41561-023-01273-5

Le Paih, N., Hattermann, T., Boebel, O., Kanzow, T., Lüpkes, C., Rohardt, G., … Herbette, S. (2020). Coherent Seasonal Acceleration of the Weddell Sea Boundary Current System Driven by Upstream Winds. *Journal of Geophysical Research: Oceans*, *125*(e2020JC016316), 1-20.

Martin, T., Tsamados, M., Schroeder, D., & Feltham, D. L. (2016). The impact of variable sea ice roughness on changes in Arctic Ocean surface stress: A model study. *Journal of Geophysical Research: Oceans*, *121*, 1931-1952.

Mathiot, P., Goosse, H., Fichefet, T., Barnier, B., & Gallée, H. (2011). Modelling the seasonal variability of the Antarctic Slope Current. *Ocean Science*, *7*, 455-470. doi: https://doi.org/10.5194/os-7-455-2011

McDougall, T. J., & Barker, P. M. (2011). Getting started with TEOS-10 and the Gibbs Seawater (GSW) Oceanographic Toolbox. *Scor/Iapso WG127*, 1-32.

Nakayama, Y., Greene, C. A., Paolo, F. S., Mensah, V., Zhang, H., Kashiwase, H., … Aoki, S. (2021). Antarctic Slope Current Modulates Ocean Heat Intrusions

Towards Totten Glacier. *Geophysical Research Letters*, *48*(17), 1-10.

Naveira Garabato, A. C., Dotto, T. S., Hooley, J., Bacon, S., Tsamados, M., Ridout, A., ... Meredith, M. P. (2019). Phased Response of the Subpolar Southern Ocean to Changes in Circumpolar Winds. *Geophysical Research Letters*, *46*(11), 6024-6033.

Neme, J., England, M. H., & Hogg, A. M. (2021). Seasonal and Interannual Variability of the Weddell Gyre From a High-Resolution Global Ocean-Sea Ice Simulation During 1958–2018. *Journal of Geophysical Research: Oceans*, *126*, 1-19.

Nøst, O. A. (2004). Measurements of ice thickness and seabed topography under the Fimbul Ice Shelf, Dronning Maud Land, Antarctica. *Journal of Geophysical Research: Oceans*, *109*, 1-14.

Nøst, O. A., Biuw, M., Tverberg, V., Lydersen, C., Hattermann, T., Zhou, Q., ... Kovacs, K. M. (2011). Eddy overturning of the Antarctic Slope Front controls glacial melting in the Eastern Weddell Sea. *Journal of Geophysical Research: Oceans*, *116*, 1-17.

Núñez-Riboni, I., & Fahrbach, E. (2009). Seasonal variability of the Antarctic Coastal Current and its driving mechanisms in the Weddell Sea. *Deep Sea Research Part I: Oceanographic Research Papers*, *56*(11), 1927-1941.

Pauthenet, E., Sallée, J.-B., Schmidtko, S., & Nerini, D. (2021). Seasonal Variation of the Antarctic Slope Front Occurrence and Position Estimated from an Interpolated Hydrographic Climatology. *Journal of Physical Oceanography*, *51*(5), 1539 - 1557. Retrieved from `https://journals.ametsoc.org/view/journals/phoc/51/5/JPO-D-20-0186.1.xml` doi: https://doi.org/10.1175/JPO-D-20-0186.1

Si, Y., Stewart, A. L., & Eisenman, I. (2023). Heat transport across the Antarctic Slope Front controlled by cross-slope salinity gradients. *Science Advances*, *9*(18), 1-12. Retrieved from `https://www.science.org/doi/abs/10.1126/sciadv.add7049` doi: 10.1126/sciadv.add7049

Smedsrud, L. H., Jenkins, A., Holland, D. M., & Nøst, O. A. (2006). Modeling ocean processes below Fimbulisen, Antarctica. *Journal of Geophysical Research: Oceans*, *111*, 1-13.

Steiger, N., Darelius, E., Kimura, S., Patmore, R. D., & Wåhlin, A. K. (2022).

The Dynamics of a Barotropic Current Impinging on an Ice Front. *Journal of Physical Oceanography*, *52*(12), 2957 - 2973. Retrieved from `https://journals.ametsoc.org/view/journals/phoc/52/12/JPO-D-21-0312.1.xml` doi: 10.1175/JPO-D-21-0312.1

Stewart, A. L., Klocker, A., & Menemenlis, D. (2019). Acceleration and Overturning of the Antarctic Slope Current by Winds, Eddies, and Tides. *Journal of Physical Oceanography*, *49*(8), 2043 - 2074. Retrieved from `https://journals.ametsoc.org/view/journals/phoc/49/8/jpo-d-18-0221.1.xml` doi: 10.1175/JPO-D-18-0221.1

Stewart, A. L., & Thompson, A. F. (2015). Eddy-mediated transport of warm Circumpolar Deep Water across the Antarctic Shelf Break. *Geophysical Research Letters*, *42*(2), 432-440. Retrieved from `https://agupubs.onlinelibrary.wiley.com/doi/abs/10.1002/2014GL062281` doi: 10.1002/2014GL062281

Sverdrup, H. U. (1954). The Currents off the Coast of Queen Maud Land. *Norsk Geografisk Tidsskrift*, *14*(1-4), 239-249.

Thompson, A. F., Heywood, K. J., Schmidtko, S., & Stewart, A. L. (2014). Eddy transport as a key component of the Antarctic overturning circulation. *Nature Geosciences*, *7*, 879-884.

Thompson, A. F., Stewart, A. L., Spence, P., & Heywood, K. J. (2018). The Antarctic Slope Current in a Changing Climate. *Reviews of Geophysics*, *56*, 741-770.

Tsamados, M., Feltham, D. L., Schroeder, D., Flocco, D., Farrell, S. L., Kurtz, N., … Bacon, S. (2014). Impact of Variable Atmospheric and Oceanic Form Drag on Simulations of Arctic Sea Ice. *Journal of Physical Oceanography*, *44*(5), 1329 - 1353.

Tschudi, M., Meier, W. N., Stewart, J. S., Fowler, C., & Maslanik, J. (2019). Polar Pathfinder Daily 25 km EASE-Grid Sea Ice Motion Vectors, Version 4. [March 2019 to January 2021, 180°W - 180°E and 90°S - 37°S]. *NASA National Snow and Ice Data Center Distributed Active Archive Center. Boulder/Colorado/USA.*. (URL: `https://doi.org/10.5067/INAWUWO7QH7B`. Last accessed: 08.03.2022)

Vernet, M., Geibert, W., Hoppema, M., Brown, P. J., Haas, C., Hellmer, H. H., … Verdy, A. (2019). The Weddell Gyre, Southern Ocean: Present Knowledge and Future Challenges. *Reviews of Geophysics*, *57*(3), 623-708. Retrieved from https://agupubs.onlinelibrary.wiley.com/doi/abs/10.1029/2018RG000604 doi: 10.1029/2018RG000604

Wåhlin, A. K., Steiger, N., Darelius, E., Assmann, K. M., Glessmer, M. S., Ha, H. K., ... Viboud, S. (2020). Ice front blocking of ocean heat transport to an Antarctic ice shelf. *Nature*, *578*(7796), 568-571.

Webb, D. J., Holmes, R. M., Spence, P., & England, M. H. (2022). Propagation of barotropic Kelvin waves around Antarctica. *Ocean Dynamics*, *72*, 405-419.

Zhou, Q., Hattermann, T., Nøst, O. A., Biuw, M., Kovacs, K. M., & Lydersen, C. (2014). Wind-driven spreading of fresh surface water beneath ice shelves in the Eastern Weddell Sea. *Journal of Geophysical Research: Oceans*, *119*, 3818-3833.

Observed Seasonal Evolution of the Antarctic Slope Current System off the Coast of Dronning Maud Land, East Antarctica

Julius Lauber[1,2], Laura de Steur[1], Tore Hattermann[1], Elin Darelius[2,3]

[1]Norwegian Polar Institute, Tromsø, Norway
[2]Geophysical Institute, University of Bergen, Bergen, Norway
[3]Bjerknes Centre for Climate Research, Bergen, Norway

Key Points:

- The seasonal maximum in thermocline depth and minimum in subsurface salinity occurs up to six months later over 2200 m than 1100 m isobath
- Buoyancy fluxes from sea ice melt play an important role in seasonal variations in the baroclinic slope current strength
- Flow into the Fimbulisen cavity is strongest in spring/summer when the Antarctic Slope Current is weakest

Corresponding author: Julius Lauber, `julius.lauber@npolar.no`

Abstract

The access of heat to the Antarctic ice shelf cavities is regulated by the Antarctic Slope Front, separating relatively warm offshore water masses from cold water masses on the continental slope and inside the cavity. Previous observational studies along the East Antarctic continental slope have identified the drivers and variability of the front and the associated current, but a complete description of their seasonal cycle is currently lacking. In this study, we utilize two years (2019-2020) of observations from two oceanographic moorings east of the prime meridian to further detail the slope front and current seasonality. In combination with climatological hydrography and satellite-derived surface velocity, we identify processes that explain the hydrographic variability observed at the moorings. These processes include (i) an offshore spreading of seasonally formed Antarctic Surface Water, resulting in a lag in salinity and thermocline depth seasonality toward deeper isobaths, and (ii) the crucial role of buoyancy fluxes from sea ice melt and formation for the baroclinic seasonal cycle. Finally, data from two sub-ice-shelf moorings below Fimbulisen show that flow at the main sill into the cavity seasonally coincides with a weaker slope current in spring/summer. The flow is directed out of the cavity in autumn/winter when the slope current is strongest. The refined description of the variability of the slope current and front contributes to a more complete understanding of processes important for ice-shelf-ocean interactions in East Antarctica.

Plain Language Summary

Ice shelves are the floating extensions of a land ice sheet. Along most of the East Antarctic coast, the water temperature below the ice shelves is close to the freezing point ($-2\,^{\circ}$C). This limits the melting of the ice from below. In front of the ice shelves, relatively warm water ($1\,^{\circ}$C) is located, but it usually cannot reach the ice due to a strong alongshore current, the Antarctic Slope Current. Here, we use temperature, salinity, and velocity observations from moored instruments at two locations within this current to investigate how it changes throughout the year. Our analyses are supported by two other data sets. We observe that changes in temperature, salinity, and velocity during the year happen earlier at the coast than offshore. In addition, we find that yearly sea ice melt during austral summer contributes to speeding up the Antarctic Slope Current in autumn. When the current is weakest, we observe a southward flow close to the seafloor toward Fimbulisen Ice Shelf, and a northward flow away from the shelf when the slope current is strongest. A better understanding of the Antarctic Slope Current is important to predict ice shelf melting in the future.

1 Introduction

The Antarctic Slope Front (ASF) is a key feature regulating offshore-onshore exchanges along most of the Antarctic coast (Jacobs, 1991; Thompson et al., 2018). Easterly alongshore winds drive onshore Ekman transport that accumulates surface water at the coast; due to continuity, this water is downwelled (Sverdrup, 1954; Mathiot et al., 2011), creating the ASF. The resulting meridional sea surface height (SSH) and density gradients balance a geostrophic current, the Antarctic Slope Current (ASC). The strength of the ASF/ASC controls the extent to which offshore Circumpolar Deep Water, capable of increasing basal melting, can access the continental shelf and the ice shelf cavities (Smedsrud et al., 2006; Nøst et al., 2011; Nakayama et al., 2021).

In the Weddell Sea, the large-scale circulation is dominated by the clockwise Weddell Gyre (Deacon, 1979; Vernet et al., 2019; Neme et al., 2021), driven by the large-scale wind stress curl (Gordon et al., 1981; Armitage et al., 2018; Auger, Sallée, et al., 2022) modulated by sea ice (Naveira Garabato et al., 2019). The southern limb of the gyre represents the ASC which in Dronning Maud Land (DML, 20°W-45°E) flows along the narrow continental shelf in close proximity to the ice shelves (Smedsrud et al., 2006; Nøst et al., 2011). In this region, the meridional SSH and density gradients lead to a westward ASC (Thompson et al., 2018) that decreases with depth (Huneke et al., 2022; Le Paih et al., 2020). In summer, a counter-current near the bottom has been observed (Heywood et al., 1998; Núñez-Riboni & Fahrbach, 2009; Chavanne et al., 2010). Warm Deep Water (WDW), a derivative of Circumpolar Deep Water in the Weddell Sea, is located close to the coast, but suppressed below the shelf break depth due to a steep ASF (Heywood et al., 1998; Hattermann, 2018; Thompson et al., 2018). This regime has been labeled as the Fresh Shelf regime by Thompson et al. (2018). Despite the steep ASF, modified WDW (mWDW) may cross the continental slope toward the ice shelf cavities via baroclinic eddies (Nøst et al., 2011; Hattermann et al., 2012; Thompson et al., 2014). As opposed to the West Antarctic ice shelves, however, no continuous warm water presence has yet been observed in the DML ice shelf cavities (Hattermann et al., 2012; Lauber, Hattermann, et al., 2023).

Previous analyses of the ASF/ASC system have revealed both the hydrography (Hattermann, 2018; Pauthenet et al., 2021) and the currents (Le Paih et al., 2020) to evolve coherently along the southern rim of the Weddell Sea, following isobaths due to the conservation of potential vorticity (Thompson et al., 2018). Auger, Sallée, et al. (2022) proposed that the SSH is seasonally forced by the zonal ocean stress (wind stress modulated by sea ice) over shallow isobaths ($< 1000\,\mathrm{m}$) and by ocean stress curl over deep isobaths ($> 1000\,\mathrm{m}$). The strongest depth-mean currents from moored instruments at the prime meridian have been observed in April/May over 2000 m depth, and in June over 3500 m depth, i.e. delayed by one to two months (Núñez-Riboni & Fahrbach, 2009; Le Paih et al., 2020). A similar delay in ASC seasonality between shallow and deep isobaths was found in circum-Antarctic satellite-derived geostrophic surface velocities (Auger, Sallée, et al., 2022). This feature has been hypothesized to originate from the sea ice edge seasonally moving offshore and associated changes in atmosphere-ocean momentum transfer (Núñez-Riboni & Fahrbach, 2009; Auger, Sallée, et al., 2022).

The baroclinic variability of the ASC on seasonal timescales in the Weddell Sea is associated with a steepening of the ASF from March to July and a relaxing from August to February (Pauthenet et al., 2021), caused by buoyancy forcing (Heywood et al., 1998) and wind (Graham et al., 2013): sea ice melt and surface warming from October/November on create a fresh and warm, and thus buoyant, water mass called Antarctic Surface Water (ASW). It accumulates at the coast via wind-driven onshore Ekman transport, seasonally forming a secondary, relatively shallow ($< 250\,\mathrm{m}$) front near the surface around February to April (Heywood et al., 1998; Hattermann, 2018). It is, however, unclear to what extent the seasonal production of ASW, which is accumulated at the coast, drives the ASC, independently of a seasonal ocean stress increase. Eddy overturning counteracts the steepening of the ASF and secondary front (Nøst et al., 2011; Zhou et al., 2014; Stewart & Thompson, 2015) and eddy-resolving models indicate that this is associated with an offshore spreading of ASW (Si et al., 2023). Following the sea ice minimum, which typically occurs in March, the ASW is gradually transformed into more saline Winter Water (WW) via brine release due to sea ice formation (Nøst et al., 2011). Overall, our knowledge of the ASF/ASC is based on a limited amount of observations and idealized models and hence it is incomplete. As a consequence, it is unknown how the ASF/ASC seasonality relates to warm inflow under the ice shelves along the eastern Weddell Sea.

In this study, we present new time series of temperature, salinity, oxygen, and velocity from April 2019 to December 2020, obtained from two oceanographic moorings located over isobaths of 1100 m and 2200 m east of the prime meridian. These data are introduced in section 2, along with a CTD section at 6°E, climatological hydrography (Hattermann, 2018), satellite-derived surface geostrophic velocities (Auger, Prandi, & Sallée, 2022), and mooring observations from the ice shelf cavity of Fimbulisen (located 200 km downstream). Methods to analyze these data are described in section 3. The new ASF/ASC observations are presented in section 4.1, and seasonal drivers of ASF/ASC seasonality are refined using the mentioned auxiliary data sets in section 4.2. In section 4.3, we assess how the seasonal ASF/ASC variability relates to the inflow into the ice shelf cavity of Fimbulisen. Finally, the results are discussed in light of the existing literature in section 5, and final conclusions are given in section 6.

2 Data

Two oceanographic moorings were deployed from R/V Kronprins Haakon in March 2019 during the Southern Ocean Ecosystem cruise off the DML coast and recovered from M/V Malik Arctica in December 2020 and January 2021 during the Troll Transect cruise. One mooring ($\mathrm{DML_{deep}}$) was located at 6.0°E, 69.1°S over a water depth of 2166 m. The other mooring ($\mathrm{DML_{shallow}}$) was located at 10.6°E, 69.4°S over a water depth of 1059 m, on the eastern flank of "Astrid Ridge" (Fig. 1a). Both moorings were equipped with one Teledyne 300 kHz ADCP and one Teledyne 150 kHz ADCP, two Nortek Aquadopp current meters, three/four Sea-Bird SBE37 MicroCATs, and 11/10 Sea-Bird SBE56 thermistors ($\mathrm{DML_{deep}}$/$\mathrm{DML_{shallow}}$). Details about the instrumentation are given in Table S1 and S2 in Supporting Information S1.

The mooring data are complemented by a CTD section that was taken between 70°S and 68°S along 6°E during the Troll Transect cruise in December 2020 and January 2021 using an SBE 911plus CTD.

A climatology of temperature and salinity sections with monthly resolution obtained from instrumented seals and ship sections around 17°W between 1977 and 2016 was used (Hattermann, 2018, referred to as H18 hereafter) to support and extend the analyses from our mooring observations.

We also include a data set of satellite-derived SSH and surface geostrophic current anomalies (Auger, Prandi, & Sallée, 2022, referred to as A22 hereafter), spanning the period from April 2013 to July 2019. These data overlap only partly with the open-ocean mooring period starting in late March 2019, and instead of comparing the time series directly, monthly mean climatologies of the SSH and geostrophic currents were calculated for the grid points along 6°E.

Monthly mean sea ice concentration (DiGirolamo et al., 2022) and velocity (Tschudi et al., 2019) data at 25 km resolution were obtained from the National Snow and Ice Data Centre. Monthly mean 10 m wind velocities were taken from the fifth generation of European Center for Medium-Range Weather Forecasts atmospheric reanalyses (ERA5, Hersbach et al., 2023).

In addition, data from two sub-ice-shelf moorings installed under Fimbulisen (Hattermann et al., 2012; Lauber, Hattermann, et al., 2023) were used. These moorings are located along expected major deep inflow pathways of WDW into the cavity (M1 and M3, Fig. 1a) and have delivered temperature and velocity data at two depths each from 2009 to 2021.

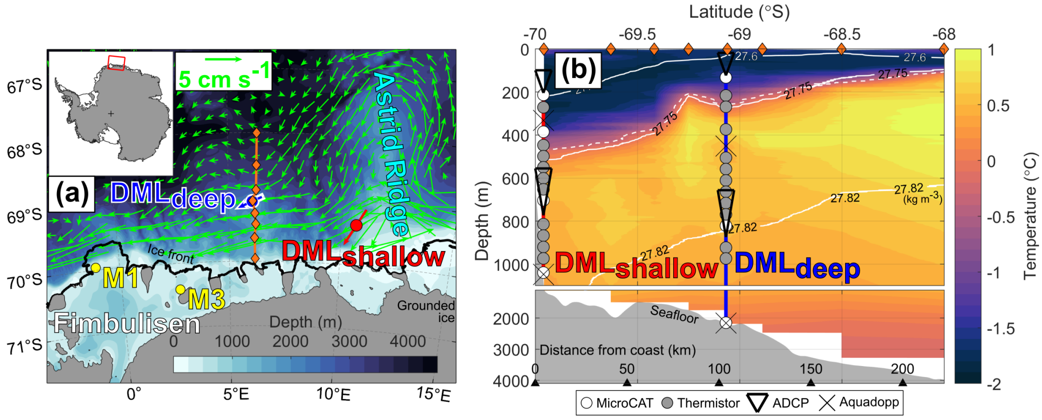

Figure 1. (a) Map of the study region. $\mathrm{DML_{deep}}$/$\mathrm{DML_{shallow}}$ denote the open-ocean moorings, and M1/3 denote the sub-ice shelf moorings. The orange line shows the location of the CTD section in panel b, with stations marked by diamonds. Colors show the bathymetry (IBCSO v2, Dorschel et al., 2022). Arrows at the offshore mooring locations show the direction and strength of the depth- and time-averaged currents, and green arrows show the difference between April to July and August to March in surface geostrophic currents (Auger, Prandi, & Sallée, 2022). The scale arrow is valid for all arrows. (b) In-situ temperature of the CTD section indicated by the orange line in panel a. Solid white lines show selected isopycnals (potential density anomaly) and the single dashed white line shows the $-0.3\,^{\circ}\mathrm{C}$ isotherm. Diamonds at the top are the station locations. The vertical blue line shows the location of $\mathrm{DML_{deep}}$, and the vertical red line shows the isobath-projected location of $\mathrm{DML_{shallow}}$.

3 Methods

To simplify investigations across the ASF/ASC, the data of $\mathrm{DML_{shallow}}$ were projected on the same isobath at the longitude of $\mathrm{DML_{deep}}$ (Fig. 1b). When doing this, we assumed that the flow (green arrows in Fig. 1a) is oriented along isobaths, as has been observed by Le Paih et al. (2020) for the Weddell Sea and is corroborated by theoretical considerations of Isachsen et al. (2003). Therefore, for all velocity data, the component in the direction of the time- and depth-mean (red/blue arrow in Fig. 1a) will be shown in the following. The original location of $\mathrm{DML_{deep}}$ (105 km distance from the coast) and the projected location of $\mathrm{DML_{shallow}}$ (10 km distance from the coast) within the ASF with their instruments are shown in Fig. 1b.

Daily and monthly averages of the mooring time series were computed for use in subsequent analysis. Hydrographic properties like absolute salinity, conservative temperature, and potential density were computed using the Gibbs Seawater Toolbox (McDougall & Barker, 2011). Temporary gaps in some of the ADCP bins due to seasonally reduced backscatter intensity were filled or extrapolated via a vertical linear regression of all available bins.

Vertical profiles of temperature and salinity of the H18 data, provided as a function of isobath, were projected on the bathymetry at 6°E, where the continental slope is less steep than at the original longitude of the climatology of 17°W. For this purpose, the bathymetry at 6°E was taken as a longitudinal average from 3°E to 9°E, based on IBCSO v2 data (Dorschel et al., 2022), to smooth out small-scale features.

Based on the general water mass distribution, the thermocline depth (TCD), i.e. the depth of the interface between WDW and WW, at the open-ocean moorings was defined as the depth of the $-0.3\,^{\circ}$C isotherm after linear interpolation. Due to the vertically densely spaced thermistors (Fig. 1b), this depth was determined with an uncertainty of less than 50 m. The ASF slope was then calculated by combining the two thermocline depths:

$$slope_{ASF} = \frac{TCD_{shallow} - TCD_{deep}}{\Delta y} \tag{1}$$

Here, $TCD_{shallow}$ and TCD_{deep} are the thermocline depths for $\mathrm{DML_{shallow}}$ and $\mathrm{DML_{deep}}$, respectively, and $\Delta y = 100$ km is the horizontal distance between the position of $\mathrm{DML_{deep}}$ and the projected position of $\mathrm{DML_{shallow}}$. The same calculation was conducted for the H18 data over the corresponding isobaths.

The barotropic velocity, i.e. the depth-independent component, was estimated from the mooring data (UBT_{obs}) via averages over the depth ranges where the vertical gradient in velocity is the smallest:

$$UBT_{obs} = \overline{U_{obs,\Delta z}} \tag{2}$$

Here, $U_{obs,\Delta z}$ is the observed along-stream velocity of the lowermost 12 bins of the lower ADCP at each mooring (683-773 m at $\mathrm{DML_{shallow}}$, 784-874 m at $\mathrm{DML_{deep}}$), selected after inspecting the profiles. The bar indicates an average over this depth range. For comparison, the barotropic velocity was also estimated from the auxiliary data by taking the difference between the A22 surface geostrophic velocity at 6°E ($UGEO_{A22}$, containing both barotropic and baroclinic current components) and the surface baroclinic velocity from the H18 data (UBC_{H18}, defined in Eqn. 5) after binning them on the same grid:

$$UBT_{H18A22} = UGEO_{A22} - UBC_{H18} \tag{3}$$

From the resulting time-latitude field of velocity, time series at the mooring isobaths were extracted.

The near-surface baroclinic velocity, i.e. the depth-varying component, was estimated from the mooring data (UBC_{obs}) by subtracting UBT_{obs} from the measured velocity at the uppermost ADCP bin (100 m at $\mathrm{DML_{shallow}}$, 20 m at $\mathrm{DML_{deep}}$):

$$UBC_{obs} = U_{obs} - UBT_{obs} \tag{4}$$

Here, U_{obs} is the observed along-stream velocity at the uppermost ADCP bin. The baroclinic velocity was also calculated from the H18 climatology for 6°E (UBC_{H18}) using the thermal wind equation:

$$UBC^{i}_{H18} = \frac{\Delta z}{\rho_0 f}\frac{\rho^{i}_{j+1} - \rho^{i}_{j}}{\Delta y} + UBC^{i-1}_{j} \tag{5}$$

Here, $\Delta z = 20\,\mathrm{m}$ is the depth increment, $\rho_0 = 1028\,\mathrm{kg\,m^{-3}}$ is a background density, f is the Coriolis parameter, i is the upward increasing depth index, j is the northward increasing meridional index, and $\Delta y = 4\,\mathrm{km}$ is the meridional increment. Zero velocity was assumed at the bottom or the lowest depth with data available. From the resulting depth-isobath-time field, time series were extracted over the isobaths and at the upper ADCP bin depths of $\mathrm{DML_{deep}}$ and $\mathrm{DML_{shallow}}$ to compare to UBC_{obs}.

Sea ice concentration and velocity, as well as wind data were interpolated on a common polar stereographic grid and combined to yield an estimate of the ocean stress (Martin et al., 2016; Dotto et al., 2018):

$$\vec{\tau} = \alpha\vec{\tau}_{ice-water} + (1-\alpha)\vec{\tau}_{air-water} \tag{6}$$

with

$$\vec{\tau}_{ice-water} = \rho_{water} C_{iw} \left| \vec{U}_{ice} \right| \vec{U}_{ice} \quad (7)$$
$$\vec{\tau}_{air-water} = \rho_{air} C_d \left| \vec{U}_{air} \right| \vec{U}_{air} \quad (8)$$

Here, α is the sea ice concentration, $\rho_{air} = 1.25\,\mathrm{kg\,m^{-3}}$ is the background density of air, $\rho_{water} = 1028\,\mathrm{kg\,m^{-3}}$ is the background density of seawater, $\vec{U}_{ice}$ is the horizontal sea ice velocity, $\vec{U}_{air}$ is the 10 m horizontal wind and $C_d = 1.25\times10^{-3}$ and $C_{iw} = 5.50\times10^{-3}$ (Tsamados et al., 2014) are the drag coefficients for the air-water and ice-water interface, respectively. Stresses from the ocean currents on the ice from below were not included here, possibly creating biases close to the coast where the sea ice velocity is similar to the ocean velocity (Stewart et al., 2019). Le Paih et al. (2020), however, show that the ocean stress in this region can still be qualitatively valid despite neglecting the ocean currents. The curl was calculated from the ocean stress, with positive (negative) values indicating downwelling (upwelling) favorable conditions.

To assess the relationship between the ASF/ASC dynamics and inflow of mWDW below Fimbulisen, the data from the lower M1 and M3 instruments (at 540 m and 450 m, respectively) close to the seabed were used, referred to as $\mathrm{M1_{lower}}$ and $\mathrm{M3_{lower}}$ hereafter. The velocity was rotated to be oriented into the cavity along the bathymetry, that is $-30°$ at $\mathrm{M1_{lower}}$ and $-120°$ at $\mathrm{M3_{lower}}$ (0° is directed toward the east and negative values indicate a clockwise rotation).

4 Results

4.1 Mooring Observations

4.1.1 Hydrography

The CTD section from December 2020 and January 2021 (Fig. 1b) shows the typical southward down-sloping isopycnals of the ASF and the offshore core of the WDW at the northern edge of the section at a depth of around 300-400 m. The section represents a snapshot of the ASF during summertime.

A Hovmöller diagram of temperature at $\mathrm{DML_{shallow}}$ (Fig. 2a) shows a layer of cold water with temperatures down to $-1.9\,°\mathrm{C}$ over a layer of warm water with temperatures up to $1\,°\mathrm{C}$. The thermocline depth ($-0.3\,°\mathrm{C}$ isotherm) shows a systematic seasonality, deepening between April and June to 500 m, and shoaling between July and March to

200 m. At $\mathrm{DML_{deep}}$, the thermocline is on average 100 m shallower than at $\mathrm{DML_{shallow}}$ (Fig. 2c) and deepens between June and December to 400 m, i.e. it reaches its maximum depth six months later compared to $\mathrm{DML_{shallow}}$. In 2020, the deepening is interrupted by a period of shoaling in October/November. The thermocline continues to shoal to 200 m from January to May, and reaches its minimum depth two months later compared to $\mathrm{DML_{shallow}}$. The warmest WDW is seen at both sites when the thermocline is shallowest.

The upper-ocean water masses (of which the densities are almost entirely determined by salinity) at $\mathrm{DML_{shallow}}$ are characterized in a temperature-salinity (T-S) diagram (Fig. 3a): the upper water mass is cold ($\approx -1.8\,^{\circ}\mathrm{C}$) and fresh ($\approx 34.5\,\mathrm{g\,kg^{-1}}$) WW, transforming into mWDW by mixing with the lower water mass which is warm ($\approx 1\,^{\circ}\mathrm{C}$) and saline ($\approx 34.8\,\mathrm{g\,kg^{-1}}$) WDW. Oxygen (colors in Fig. 3 and time series in Fig. S1 in Supporting Information S1) is a measure of the origin of the water masses. The freshest and oxygen-richest WW is observed at the uppermost MicroCAT (210 m) at the time of the deepest thermocline in winter in June. This water mass is similar to Eastern Shelf Water, a mix between ASW and WW. The observed WW in June 2019 is almost $0.1\,\mathrm{g\,kg^{-1}}$ fresher and richer in oxygen than in June 2020. During the period of thermocline shoaling from July onward, mWDW gradually appears. The most saline, warm, and oxygen-poor mWDW is observed in March when the thermocline is shallowest (see also Fig. 2a). At the uppermost MicroCAT (130 m) at $\mathrm{DML_{deep}}$, the WDW shows similar properties as at $\mathrm{DML_{shallow}}$, but the WW is generally more saline (Fig. 3b). A first seasonal salinity minimum and oxygen maximum are observed in June 2019. After that, temperature and salinity first increase toward mWDW, but then decrease back to WW. This yields a second seasonal salinity minimum and oxygen maximum at the time of the deepest thermocline in December 2019. During the period of thermocline shoaling, the water mass properties change toward mWDW until May 2020. After that, when the thermocline deepens, WW appears again, which is $0.05\,\mathrm{g\,kg^{-1}}$ more saline and has a lower oxygen concentration than in 2019. This is similar to the higher salinities and reduced oxygen observed at $\mathrm{DML_{shallow}}$ in 2020 (relative to 2019).

The observed seasonal deepening and freshening of the WW layer at $\mathrm{DML_{shallow}}$ (Fig. 2a) is attributed to the wind-driven accumulation of ASW at the coast (Zhou et al., 2014; Hattermann, 2018): summer sea ice melt between September and February (Fig. 4a) adds freshwater to form ASW. The latter is downwelled at the coast due to the prevailing easterly winds, explaining the salinity minimum and oxygen maximum at 210 m at $DML_{shallow}$ in June 2019 and 2020 (Fig. 3a and 4b) and the deepest thermocline one month later in July (Fig. 4c). Sea ice formation between March and August (Fig. 4a) releases brine into the upper ocean and leads to a salinity increase between July and September. With temperatures almost at the freezing point and oxygen close to its maximum value, this indicates that convection takes place down to 210 m depth during this period at $DML_{shallow}$ in 2019 (box in Fig. 3a). In 2020, the temperature is higher and the oxygen concentration is lower during the sea ice formation period, suggesting that convection did not reach down to this depth.

We also identify a period of convection at DML_{deep}: From June to August 2020, the water mass evolution from mWDW to similarly cold, but more saline and less oxygen-rich WW than in 2019 shows a mixing between mWDW and WW salinified by convection (box in Fig. 3b). In October/November 2020, the increase in temperature and salinity (off the direct mixing line toward WDW) and decrease in oxygen indicate that the convection reached through the thermocline, mixing WDW upward. This is neither observed in 2019 nor at $DML_{shallow}$. At 130 m at DML_{deep}, the different seasonal cycles in salinity (Fig. 4b) and thermocline depth (Fig. 4c) than at $DML_{shallow}$ indicate that local downwelling of ASW does not control the seasonal hydrography here: the salinity minimum in December cannot be explained by local surface freshwater input, as brine release during the freezing season from March to August (Fig. 4a) would increase the salinity, and freshwater from sea ice melt would cause a salinity minimum at the end (i.e. in March), not the beginning of the melt season. The drivers of the hydrographic seasonality at DML_{deep} will be explored in section 4.2.

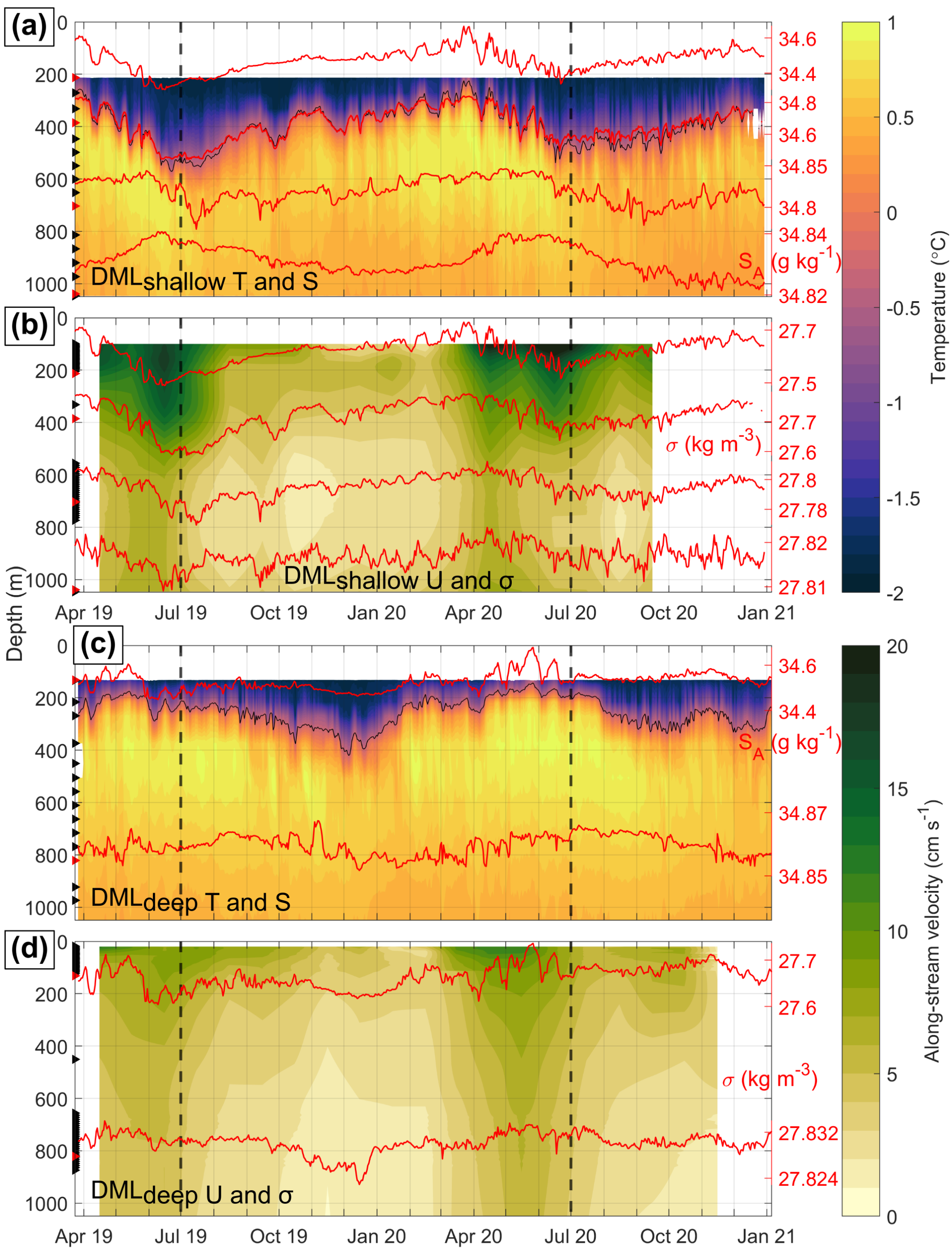

Figure 2. (a) Hovmöller diagram of daily averaged in-situ temperature at DML$_{shallow}$. The black contour indicates the $-0.3\,^{\circ}$C isotherm. Black triangles denote the depths of temperature measurements. Red lines show daily averaged time series of absolute salinity (right axes) for the depths marked with red triangles. (b) Hovmöller diagram of monthly averaged along-stream velocity at DML$_{shallow}$. Black triangles denote the depths of velocity measurements. Red lines show daily averaged time series of potential density anomaly (right axes) for the depths marked with red triangles. (c) Same as a, but for DML$_{deep}$. (d) Same as b, but for DML$_{deep}$. In c and d, the y-axis has been cut off at the bottom depth of DML$_{shallow}$ for better comparability.

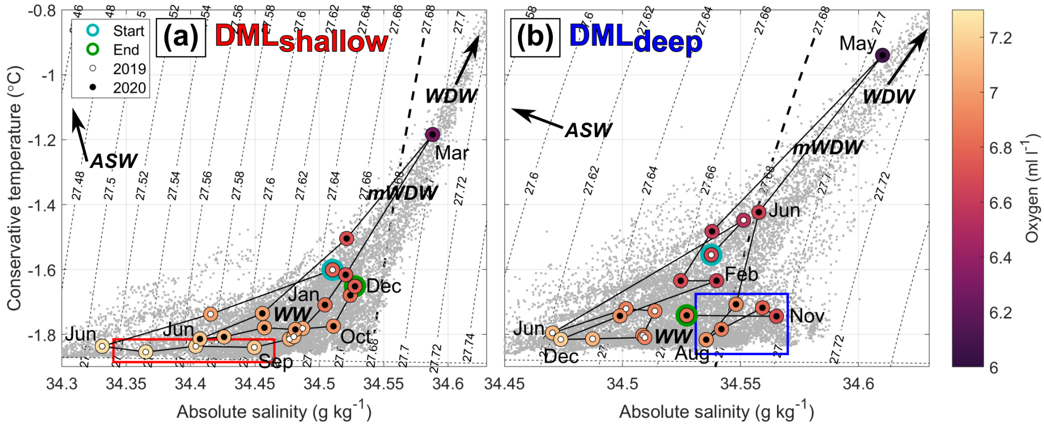

Figure 3. T-S diagrams with dissolved oxygen of the upper MicroCAT at (a) $\mathrm{DML_{shallow}}$ (210 m) and (b) $\mathrm{DML_{deep}}$ (130 m). Grey dots are the fully resolved hourly data, and colored dots are the monthly averaged data. Black lines connect the monthly points. The boxes show potential periods of convection. The thick black dotted line indicates the $27.68\,\mathrm{kg\,m^{-3}}$ isopycnal for better comparability between the two panels, as their x-axis ranges differ.

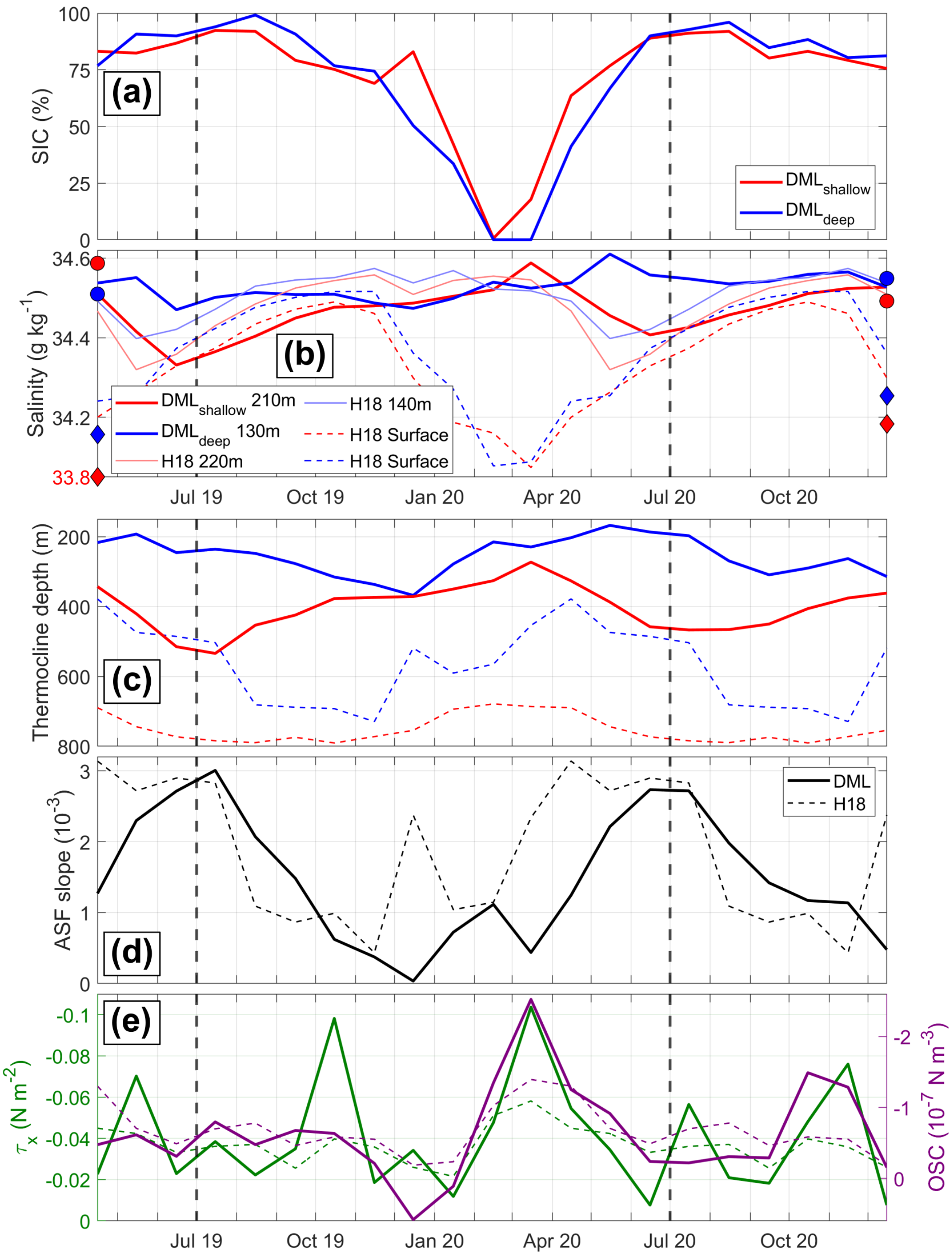

Figure 4. Monthly means of: (a) Sea ice concentration at both open-ocean mooring locations. (b) Salinity observed at the uppermost MicroCAT at both moorings (210 m at $\mathrm{DML_{shallow}}$, 130 m at $\mathrm{DML_{deep}}$), salinity from the H18 climatology over similar isobaths and at similar depths, and salinity from the H18 climatology over similar isobaths at the surface. Dots/diamonds indicate the salinity at the MicroCAT depth/surface from the CTD profiles of the deployment and recovery cruises. The red diamond on the left is off-scale. (c) Thermocline depth defined as the $-0.3\,^{\circ}$C isotherm at both moorings and from the H18 climatology over similar isobaths. (d) ASF slope estimated from the thermocline depths from panel c for the mooring data and the H18 climatology (Eqn. 1). (e) Regional zonal ocean stress (left axis) and ocean stress curl (right axis), averaged over 0–15°E and 69.5–70°S/67–69.5°S, respectively (solid lines), along with their climatology (2010-2021, dashed lines).

4.1.2 Velocity

At $\mathrm{DML_{shallow}}$, monthly mean velocities (Fig. 2b) show a surface-intensified current, which at 100 m is strongest in June in both years ($20\,\mathrm{cm\,s^{-1}}$). At 600-800 m, the velocity shows a vertical minimum throughout the length of the record. Toward the bottom, the velocity intensifies by $2\,\mathrm{cm\,s^{-1}}$. The vertical gradient, i.e. the baroclinic part, becomes more apparent in profiles when averaged over specific months (Fig. 5a): Toward the surface, the strongest vertical shear is observed in June. Below 500 m, there is smaller seasonal variability in the gradient. At $\mathrm{DML_{deep}}$ (Fig. 2d), velocities are generally smaller than at $\mathrm{DML_{shallow}}$ with maximum values of $10\,\mathrm{cm\,s^{-1}}$ at 20 m observed in May/June 2019 and April/May 2020. In contrast to $\mathrm{DML_{shallow}}$, the velocity at $\mathrm{DML_{deep}}$ continuously decreases toward the bottom (Fig. 5b). The seasonality of the upper-ocean vertical shear is weaker than at $\mathrm{DML_{shallow}}$ and strongest in March.

The estimated barotropic component (UBT_{obs}) at $\mathrm{DML_{shallow}}$ (Fig. 6b) is maximum ($6\,\mathrm{cm\,s^{-1}}$) in May/June 2019 and April 2020. At $\mathrm{DML_{deep}}$, the values are slightly smaller and the maximum occurs one month later than at $\mathrm{DML_{shallow}}$ in 2020, but not in 2019 when there is zero lag. The baroclinic velocity (UBC_{obs}) at $\mathrm{DML_{shallow}}$ at 100 m depth (Fig. 6d) shows a first seasonal maximum ($12\,\mathrm{cm\,s^{-1}}$) in April 2019. In 2020, a local maximum in April is followed by a higher seasonal maximum ($20\,\mathrm{cm\,s^{-1}}$) in June. The baroclinic velocity is close to $0\,\mathrm{cm\,s^{-1}}$ from December 2019 to February 2020. At $\mathrm{DML_{deep}}$ at 20 m depth (Fig. 6e), a maximum baroclinic velocity of $7\,\mathrm{cm\,s^{-1}}$ is observed in April in both years. Seasonal minima close to $0\,\mathrm{cm\,s^{-1}}$ occur in January and December 2020.

The ASF slope, derived from the thermocline depths at $\mathrm{DML_{shallow}}$ and $\mathrm{DML_{deep}}$ (Eqn. 1), is steepest in June/July (Fig. 4d). In 2020, this is around the same time as the maximum near-surface UBC_{obs} at $\mathrm{DML_{shallow}}$ (Fig. 6d), consistent with thermal wind balance. In 2019, however, a distinct maximum in ASF slope is found in July but no clear maximum in baroclinic velocity is observed (Fig. 6d). The weakest ASF slope occurs in December when the thermocline depths at the two moorings become equal due to a shoaling at $\mathrm{DML_{shallow}}$ and a deepening at $\mathrm{DML_{deep}}$ (Fig. 4c-d). Accordingly, UBC_{obs} at $\mathrm{DML_{shallow}}$ is close to its seasonal minimum between December and February (Fig. 6d). Despite some coinciding features, the ASF slope and the baroclinic velocities at the moorings are not directly comparable, since (i) most of baroclinic velocity shear occurs above the thermocline (Fig. 5), and (ii) the (assumed) linear ASF slope between the moorings may not represent the local ASF slope at the mooring locations.

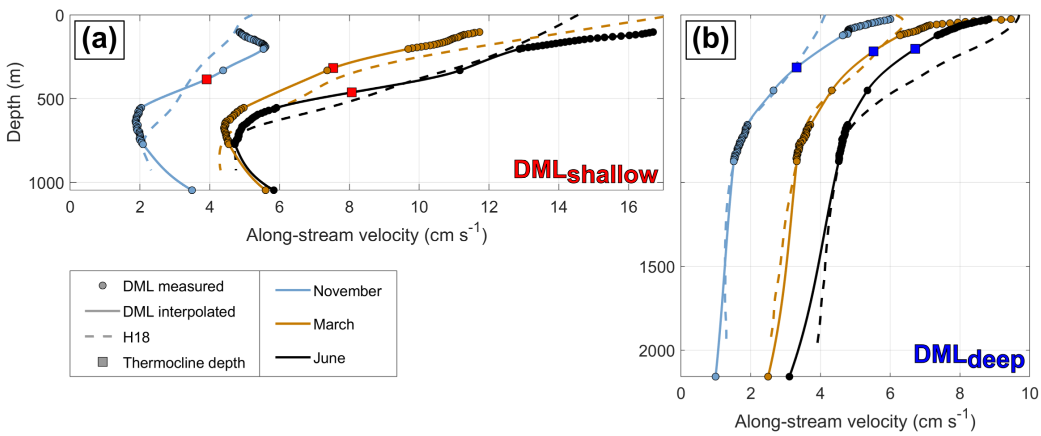

Figure 5. (a) Profiles of along-stream velocity at (a) DML$_{\mathrm{shallow}}$ and (b) DML$_{\mathrm{deep}}$, averaged over a three-month-window centered at three selected months. The velocities are vertically interpolated via a shape-preserving piecewise cubic interpolation. Additionally, the averages of the zonal baroclinic velocity profiles over the same time interval and for similar isobaths calculated from the H18 climatology are shown. For better comparability, the depth-constant UBT_{obs} has been added to the H18 profiles.

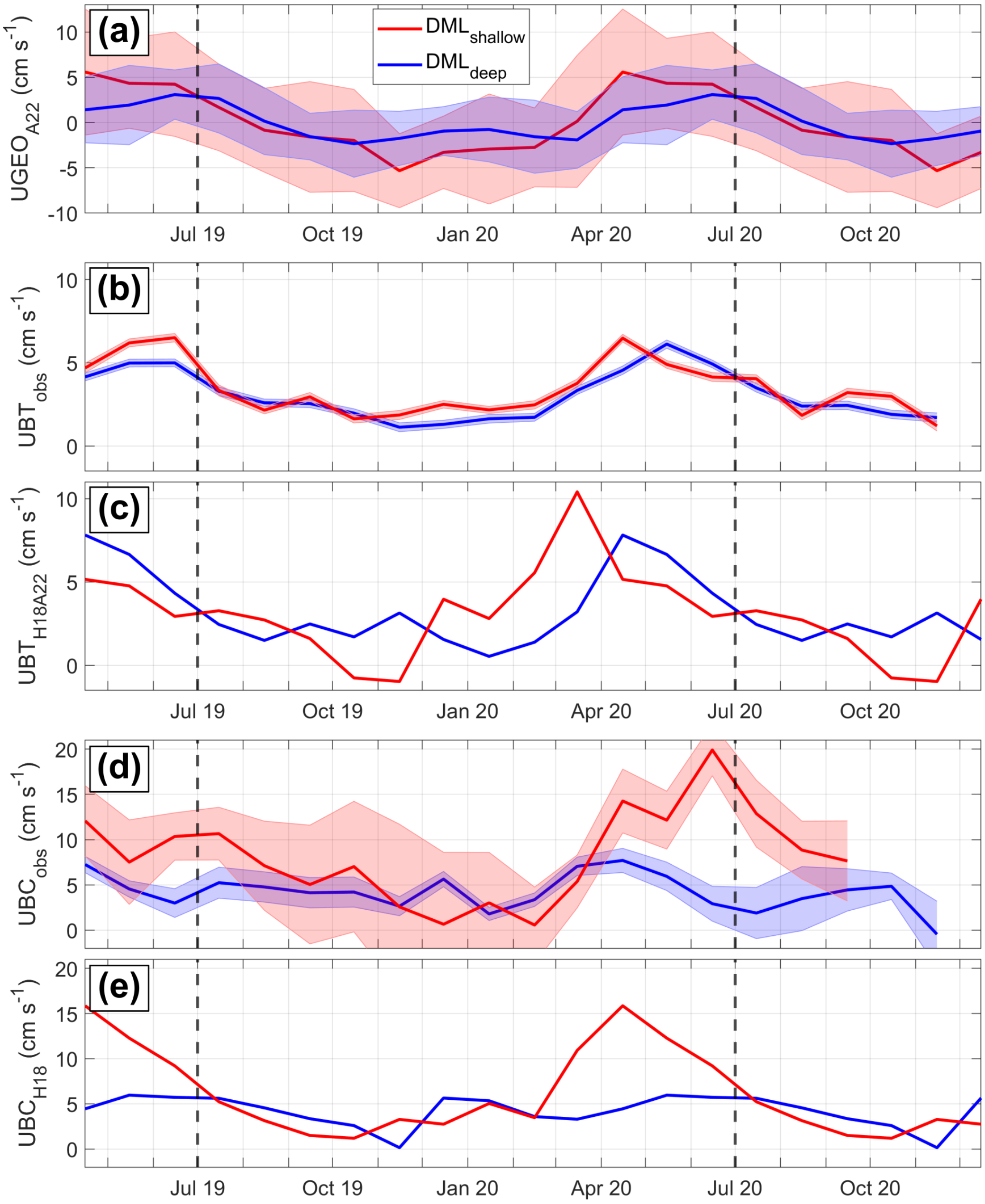

Figure 6. (a) Surface geostrophic velocity anomaly from A22 interpolated on the DML$_{shallow}$ and DML$_{deep}$ locations. (b) Barotropic velocity derived from mooring data. (c) Barotropic velocity derived from A22 and H18 data, obtained over the respective mooring isobaths. Shown are anomalies plus the respective time-mean of panel b. (d) Baroclinic velocity derived from mooring data at the uppermost ADCP bin depth (100 m at DML$_{shallow}$, 20 m at DML$_{deep}$). (e) Baroclinic velocity derived from the H18 climatology, taken over the mooring isobaths at the same depths as panel d. Details about the calculation of the error bars are given in Text S1 in Supporting Information S1.

4.1.3 Ocean Stress Forcing

To investigate the extent to which ocean stress contributes to the variability of the ASC at the moorings, we differentiate between regional (0−15°E, 67−70°S) and remote upstream (0−60°E and 50−70°S,) ocean stress and its curl.We further differentiate between the shallow (< 1000 m, more influenced by zonal ocean stress) and deep (> 1000 m, more influenced by ocean stress curl) regime suggested by Auger, Sallée, et al. (2022). We note that for both local and remote ocean stress, the modulation of the wind stress by sea ice causes the seasonal maximum in ocean stress to occur one month earlier than the maximum in wind stress.

Monthly mean regional ocean stress forcing does not show a distinct seasonal cycle during the mooring period, in contrast with the 12-year mean seasonality (Fig. 4e). The zonal ocean stress (meridionally averaged over 69.5−70°S, i.e. over the continental slope) is westward and strongest in October 2019 and March 2020. In April 2020, thermocline deepening starts at $\mathrm{DML_{shallow}}$ (Fig. 4c), and a local maximum is found in the baroclinic velocity (Fig. 6e) at $\mathrm{DML_{shallow}}$. This is consistent with coastal downwelling due to stronger onshore Ekman transport. However, no strong regional ocean stress occurred in early 2019 prior to the mooring deployment (not shown). In addition, the regional ocean stress maximum in October 2019 does not coincide with a thermocline deepening. The monthly mean regional ocean stress curl (meridionally averaged over 67−69.5°S, i.e. off the continental slope) is close to zero most of the time but has a clear maximum between February and April 2020 (Fig. 4e). Estimated Ekman upwelling of $w_{Ek} = \frac{OSC}{\rho_0 f} = 4\,\mathrm{m\,month^{-1}}$ (with ocean stress curl $OSC = -0.2 \times 10^{-7}\,\mathrm{N\,m^{-3}}$, background density $\rho_0 = 1028\,\mathrm{kg\,m^{-3}}$, Coriolis parameter $f = -1.36 \times 10^{-4}\,\mathrm{s^{-1}}$) can, however, not explain the thermocline shoaling and upper-ocean salinity increase observed at $\mathrm{DML_{deep}}$ between January and May 2020 (Fig. 4b-c). Overall, the poor agreement between UBC_{obs} at $\mathrm{DML_{shallow}}$ and regional ocean stress forcing indicates that the latter is not the main driver of the baroclinic velocity seasonality. This will be further investigated in section 4.2.

To investigate the forcing of the barotropic ASC, we correlate UBT_{obs} at $\mathrm{DML_{shallow}}$ with zonal ocean stress (Fig. 7a) and UBT_{obs} at $\mathrm{DML_{deep}}$ with ocean stress curl (Fig. 7b). The highest negative correlations are found along the East-Antarctic coast at 30−60°E with UBT_{obs} lagging the ocean stress by one month. The patterns are similar when correlating UBT_{obs} at $\mathrm{DML_{deep}}$ with zonal ocean stress or UBT_{obs} at $\mathrm{DML_{shallow}}$ with ocean stress curl. Therefore, the bands of high correlation are independent of the method differentiating the regimes from Auger, Sallée, et al. (2022). In contrast to the regional forcing (Fig. 4e), the remote ocean stress and its curl exhibit a distinct seasonal cycle during the mooring period over the areas of highest correlations along East Antarctica, similar to the multi-year climatology (Fig. 7c). Strong westward ocean stress and negative ocean stress curl seasonally increase the cross-shore SSH gradient in autumn (March-May). This gradient travels westward through coastal Kelvin waves (Webb et al., 2022), explaining the seasonal variability of the barotropic flow at the moorings (Fig. 6b). This can also explain the observed interannual variability like the maximum occurring later in 2019 than in 2020 in remote ocean stress (Fig. 7c) and UBT_{obs} (Fig. 6b).

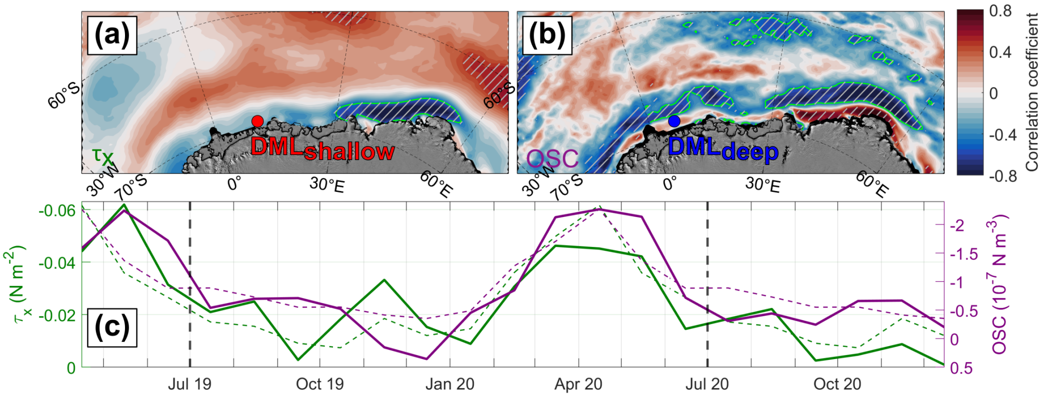

Figure 7. Correlation maps of (a) barotropic velocity UBT_{obs} at DML$_{\text{shallow}}$ from Fig. 6b, lagged by one month, and zonal ocean stress, and (b) barotropic velocity UBT_{obs} at DML$_{\text{deep}}$ from Fig. 6b, lagged by one month, and ocean stress curl at every grid point. Hatched areas indicate a significance of at least 95 %, and green lines mark areas of a correlation of at least -0.5 east of the prime meridian. The background satellite image is taken from Haran et al. (2018). (c) Zonal ocean stress (left axis) and ocean stress curl (right axis) averaged over 0−60°E and 50−70°S where the correlations from panels a and b, respectively, are at least -0.5, along with their climatology (2010-2021, dashed lines).

4.2 Seasonal Cycle from Auxiliary Data Sets

Our new mooring data show different processes governing the seasonal hydrographic and dynamic variability at DML$_{\text{shallow}}$ and DML$_{\text{deep}}$. As we will demonstrate in this section, these processes are consistent with the H18 data, providing information above the uppermost moored instruments and over multiple isobaths. We next use these data to investigate the forcing of the baroclinic seasonality and the delay in salinity and thermocline depth seasonality observed between $DML_{shallow}$ and DML_{deep} in more detail.

4.2.1 The Role of ASW for the Hydrographic Seasonality

In both the mooring records (Fig. 4b) and the H18 data set (Fig. S2 in Supporting Information S1), the seasonal subsurface salinity minimum occurs later over deeper isobaths than over shallow isobaths. For the mooring isobaths, the delay in the H18 data increases from zero at the surface, where the salinity is determined directly by freshwater input from sea ice melt, to five months at 400 m depth. The freshwater content integrated down to this depth illustrates that the offshore delay in salinity minimum is a robust feature across multiple isobaths (Fig. 8a): in March, fresh ASW accumulates at the coast, and in the subsequent months, the ASW spreads and deepens offshore, delaying the timing of maximum offshore freshwater content well into the freezing season. This is most pronounced over isobaths shallower than 2000 m. As the offshore ASW spreading and deepening displaces WW to greater depths, the deepest thermocline follows the highest freshwater content and thus shows a similar offshore delay (Fig. S3 in Supporting Information S1). This is consistent with the mooring observations and explains the different seasonalities of and the robust link between salinity and thermocline depth over the two isobaths (Fig. 2a/c).

The seasonal offshore spreading and deepening of ASW moves the secondary front and the ASF, causing the maximum surface baroclinic velocity from H18 to move toward deeper isobaths throughout the season (Fig. 8b). This is again clearest over isobaths shallower than 2000 m. Consequently, over the mooring isobaths, time series of UBC_{H18} (Fig. 6e) agree well with UBC_{obs} (Fig. 6d), apart from the maximum occurring two months later at the $DML_{shallow}$ mooring in 2020.

Next, we use the H18 data to estimate the contribution of the baroclinic component to the surface geostrophic velocity from A22. At the location of $DML_{shallow}$, the surface geostrophic velocity shows a seasonal amplitude of $10\,\mathrm{cm\,s^{-1}}$ and a maximum in April (Fig. 6a). At the DML_{deep} location, the seasonal amplitude is $5\,\mathrm{cm\,s^{-1}}$ and the maximum occurs in June (Fig. 6a). This delay becomes clearer in time-latitude space, in which the surface geostrophic velocity seasonality from A22 at 6°E also shows an offshore delay (Fig. 8c). This time lag, however, is somewhat smaller than in the H18 surface baroclinic velocity (Fig. 8b). The barotropic velocity anomaly (UBT_{H18A22}) is then estimated as the difference between the A22 surface geostrophic and H18 surface baroclinic velocity (Fig. 8d). A moderate offshore delay is still visible in the seasonal cycle of UBT_{H18A22}, with a phase shift of one to two months between the mooring sites (Fig. 6d). Given the uncertainties in both data sets that UBT_{H18A22} is derived from, we cannot conclude if this remaining phase shift is realistic (see section 5).

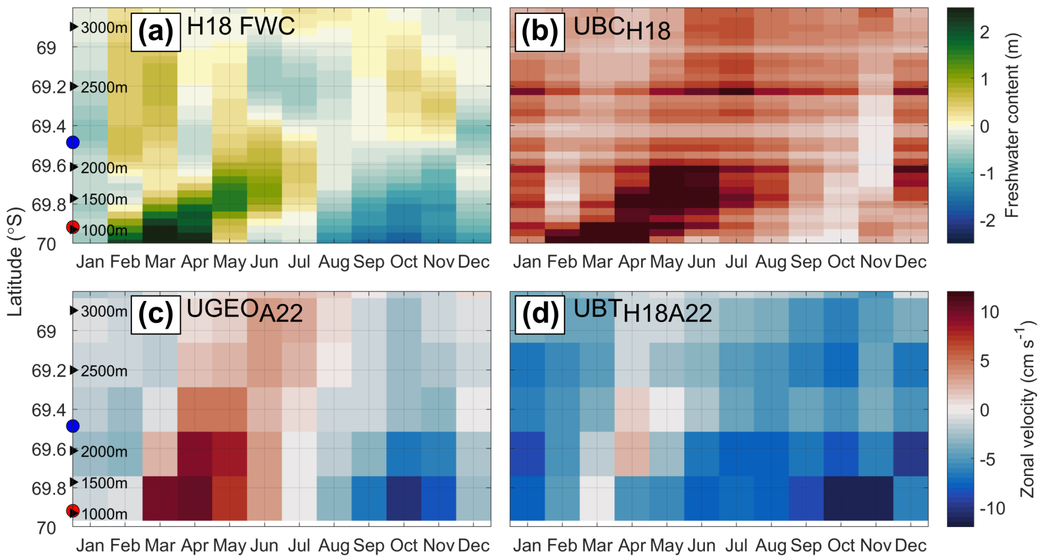

Figure 8. Hovmöller diagrams of (a) depth-integrated freshwater content within the upper 400 m referenced to a salinity of 34.6 g kg^{-1} from H18, (b) zonal surface baroclinic velocity derived from H18, (c) zonal surface geostrophic velocity anomaly from A22 at 6°E, (d) zonal barotropic velocity anomaly obtained by taking panel c minus panel b. The red/blue dots indicate the isobath of $\mathrm{DML_{shallow}}/\mathrm{DML_{deep}}$.

4.2.2 Implications for ASF/ASC Dynamics

The coastal freshwater content maximum in March (Fig. 8a) and the resulting surface baroclinic velocity (Fig. 8b) cannot originate from seasonally increased ocean stress (Fig. 4e). Instead, it is caused by the freshening of upper-ocean water masses through seasonal sea ice melt and their concurrent accumulation at the coast. These results align with observed seasonal cycles in hydrography (Fig. 2a and 4b-d) and baroclinic velocity (Fig. 5a, Fig. 6d) at $\mathrm{DML_{shallow}}$, despite a weak seasonality in local zonal ocean stress (Fig. 4e). Therefore, the mooring and H18 data are consistent in that seasonal freshwater input from sea ice melt is an essential forcing of the surface baroclinic velocity seasonality and magnitude, independent of any seasonality in ocean-stress-driven coastal downwelling.

The velocity shear toward the surface in March and June at the upper ADCPs of both moorings (reaching 110 m higher than the uppermost MicroCATs, Fig 5) indicates the presence of the secondary front between ASW and WW at the sites. Although the strongest upper-ocean velocity shear at $DML_{shallow}$ is found in March in the H18 data, and in June in the mooring data, the shapes of the observed velocity profiles generally agree with the ones from H18 over similar isobaths. In addition, the offshore delay in thermocline depth maximum and salinity minimum at DML_{deep} is consistent between the mooring and H18 data (Fig. 4b-c, Fig. 8a, Fig. S3 in Supporting Information S1). We thus infer that the offshore spreading and deepening of ASW identified in Fig. 8a also takes place at the mooring longitude of 6°E.

We propose that eddy overturning, as demonstrated by Si et al. (2023) using an eddy-resolving model, drives the observed offshore delay in seasonal freshwater content (Fig 8a): after the phase of the freshest ASW at the coast in March and with slackening local and remote ocean stress forcing, eddy overturning acts to relax the secondary front, consistent with large eddy growth rate estimates from January to June (Hattermann, 2018). Thereby, the fresh signal spreads and deepens offshore during the course of the following months, causing the observed delay in offshore thermocline depth (Fig. 4c) and salinity (Fig. 4b) seasonality. Eddy overturning also transports salty WW from offshore toward the coast, contributing to the decrease in coastal freshwater content after June (Fig. 8a) in addition to convection.

We also identify some differences between the mooring records and the H18 data: the thermocline in the H18 data is consistently 200 m deeper than in the mooring observations (Fig. 4c). As a result of this vertical offset, the seasonal salinity minimum observed in December at 130 m and 810 m at DML_{deep} (Fig. 2c) shows up in November in the H18 data below 400 m, but not above (Fig. S2b in Supporting Information S1). In addition to this vertical offset, the seasonal extremes of salinity at $DML_{shallow}$ (Fig. 4b), of the thermocline depth (Fig. 4c) and of the ASF slope (Fig. 4d) occur one to two months earlier in the H18 data than in the mooring observations. Advection of water masses within the ASC, as suggested by Graham et al. (2013), may explain the alongshore thermocline deepening, but not the delayed seasonal extremes at 6°E compared to 17°W. With the data sets being obtained in different years, we cannot conclude if the described offsets are a robust feature or the result of interannual variability, and if alongshore advection plays a role.

4.3 ASF/ASC Variability and Inflow below Fimbulisen

To assess the role of the variability of the ASF/ASC system on the deep inflow of mWDW into the cavity of Fimbulisen, we now compare the open-ocean mooring data from $\mathrm{DML_{shallow}}/\mathrm{DML_{deep}}$ with the concurrent sub-ice-shelf mooring data from $\mathrm{M1_{lower}}$ and $\mathrm{M3_{lower}}$ (Fig. 1a). The open-ocean moorings are roughly 200 km upstream of Fimbulisen, but supported by the agreement between the the mooring and H18 data, we assume that the seasonality does not change considerably over this distance.

Mooring M1 is located on the main sill that connects the cavity to the open ocean (Fig. 1a). This sill is at 560 m depth and is directed across the continental slope. Here, the velocity alternates seasonally between a period of flow into the cavity between July/August and February and a period of flow out of the cavity between March and June/July (Fig. 9a). The seasonality of the cavity inflow at $\mathrm{M1_{lower}}$ anticorrelates with the ASC strength: the current is directed into the cavity during periods of a weak barotropic and baroclinic (at 330 m, i.e. the depth of the velocity measuring instrument closest to the WDW core at $\mathrm{DML_{shallow}}$) ASC, while it is directed out of the cavity during periods of a strong ASC. At $\mathrm{M3_{lower}}$, located in the east of Fimbulisen on a second sill that is 480 m deep and directed more along the continental slope (Fig. 1a), the connection between inflow and the ASC strength is the opposite, i.e. inflow occurs during periods of a strong ASC, and outflow - or weak inflow - during periods of a weak ASC (Fig. 9a).

The temperature at $\mathrm{M1_{lower}}$ (Fig. 9b) does not show a clear seasonality during the mooring period, and we do not find a significant correlation to the seasonally varying thermocline depth (Fig. 9c) on time scales from days to months. Instead, the $\mathrm{M1_{lower}}$ temperature lies around the surface freezing point most of the time, showing irregular episodes with higher temperatures of up to almost 0 °C. These temperature extremes are not, as one would expect, associated with a particularly shallow thermocline and high WDW temperatures at $\mathrm{DML_{shallow}}$. Similarly, the cavity temperature at $\mathrm{M3_{lower}}$ does not correlate with the thermocline depth: the lowest temperatures occur shortly after the minimum in thermocline depth in March 2020. Interestingly, despite the opposing inflow and outflow velocities at the two sub-ice-shelf mooring sites, peak temperatures occur simultaneously at $\mathrm{M1_{lower}}$ and $\mathrm{M3_{lower}}$ in August/September 2019, suggesting a forcing driving mWDW inflow over a larger area. At most times, however, the temperatures at M1$_{lower}$ and M3$_{lower}$ appear to be unrelated. Further interpretations of the observed variability below Fimbulisen with regard to the ASC are given in section 5.

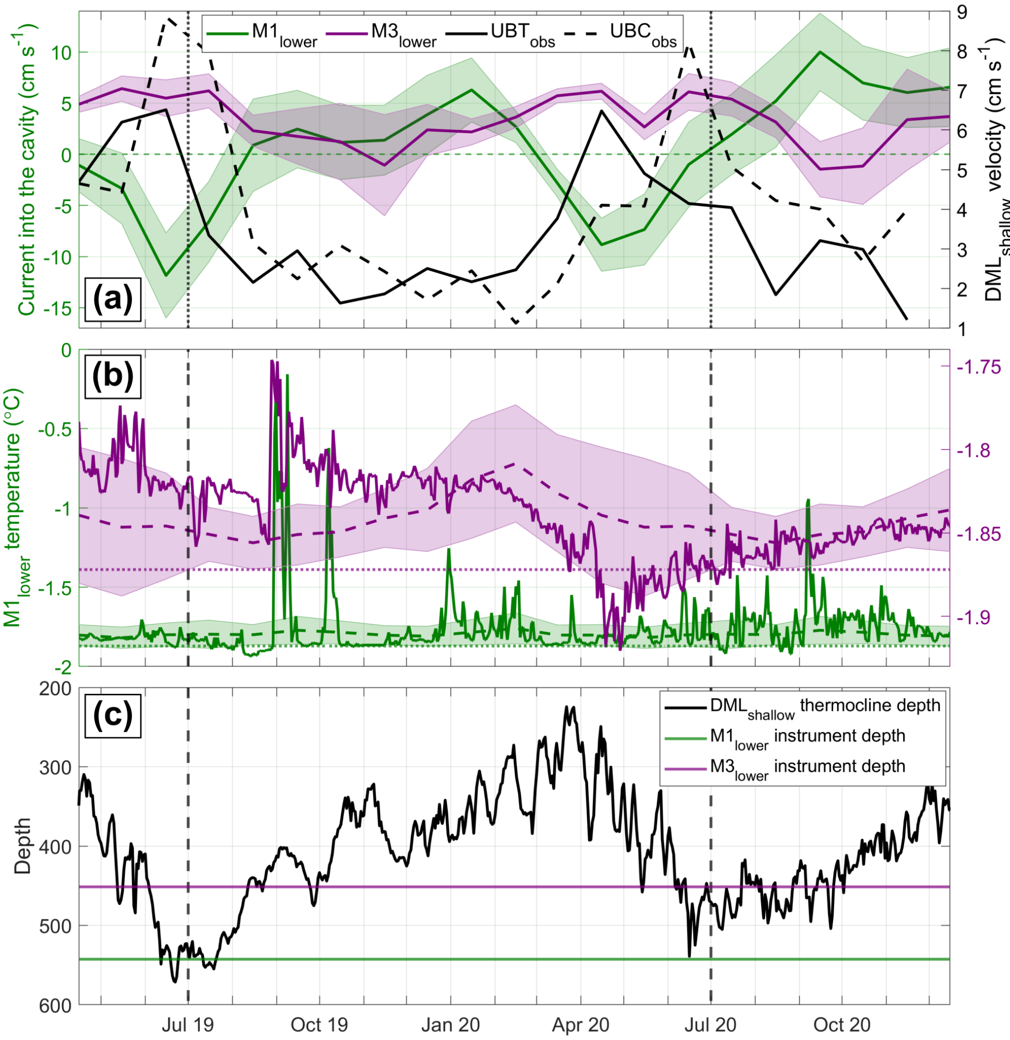

Figure 9. (a) Monthly averages of the currents at M1$_{lower}$ and M3$_{lower}$ (left axis), rotated into the cavity as described in section 3, together with UBT_{obs} (same as the red line in Fig. 6b) and UBC_{obs} at 330 m depth at DML$_{shallow}$ (right axis). Envelopes denote the standard deviation of the monthly climatology (2010-2021). (b) Daily averages of in-situ temperature at M1$_{lower}$ (left axis) and M3$_{lower}$ (right axis, solid lines), along with their monthly climatology and standard deviation (2010-2021, dashed lines and envelope, respectively). Dotted lines are the surface freezing temperature for a salinity of 34.4 g kg^{-1} (c) Daily average of the thermocline depth at DML$_{shallow}$ (same data as the solid red line in Fig. 4c), together with the mean depths of M1$_{lower}$ and M3$_{lower}$.

5 Discussion

Our findings - the seasonal spreading of ASW offshore and the role of freshwater input - help to refine the seasonality of the baroclinic component of the ASF/ASC, complementing previous findings. Based on our observations, we summarize the seasonality in three phases (Fig. 10):

In November (Fig. 10a), the ASF is weak (Fig. 10e), as the thermocline is shoaling at $\mathrm{DML_{shallow}}$ and deepening at $\mathrm{DML_{deep}}$. At the same time, the absence of ASW results in a weak meridional density gradient at all depths and thus a baroclinic velocity minimum (Fig. 10f and Fig. 5a). Sea ice melt from September and on provides freshwater to the upper ocean and leads to the formation of ASW (Fig. 10d). The regional ocean stress is weak (Fig. 10g), resulting in reduced ASF steepening.

In March (Fig. 10b), sea ice concentration and surface salinity are around their seasonal minima (Fig. 10d), and ASW has been accumulated at the coast to form a secondary front, resulting in an increase in upper-ocean baroclinic velocity (Fig. 10f and Fig. 5a). Maximum ocean stress (Fig. 10g) further aids in steepening the isopycnals. Due to the large density difference between ASW and WW, strong eddy overturning may happen at the secondary front.

The secondary front weakens in June (Fig. 10c) since no new ASW is formed after March. The remainder of the ASW spreads and deepens offshore, possibly via eddy overturning of the secondary front when ocean stress forcing weakens (Fig. 10g). Brine release from sea ice formation (Fig. 10d) along the coast as of March also starts to erode the ASW through convection, as described in section 4.1.1 and corroborated by small vertical salinity gradients between surface and depth between July and November in the H18 data (Fig. 4b). The ASF is around its steepest state, as the thermocline deepens at $\mathrm{DML_{shallow}}$ and shoals at $\mathrm{DML_{deep}}$ (Fig. 10e). The maximum upper-ocean baroclinic velocity is reached around April (H18) to June (mooring data, Fig. 10f and Fig. 5a). After this phase, weak ocean stress and further brine release cause a relaxation of the ASF and form the transition back to the first phase (Fig. 10a).

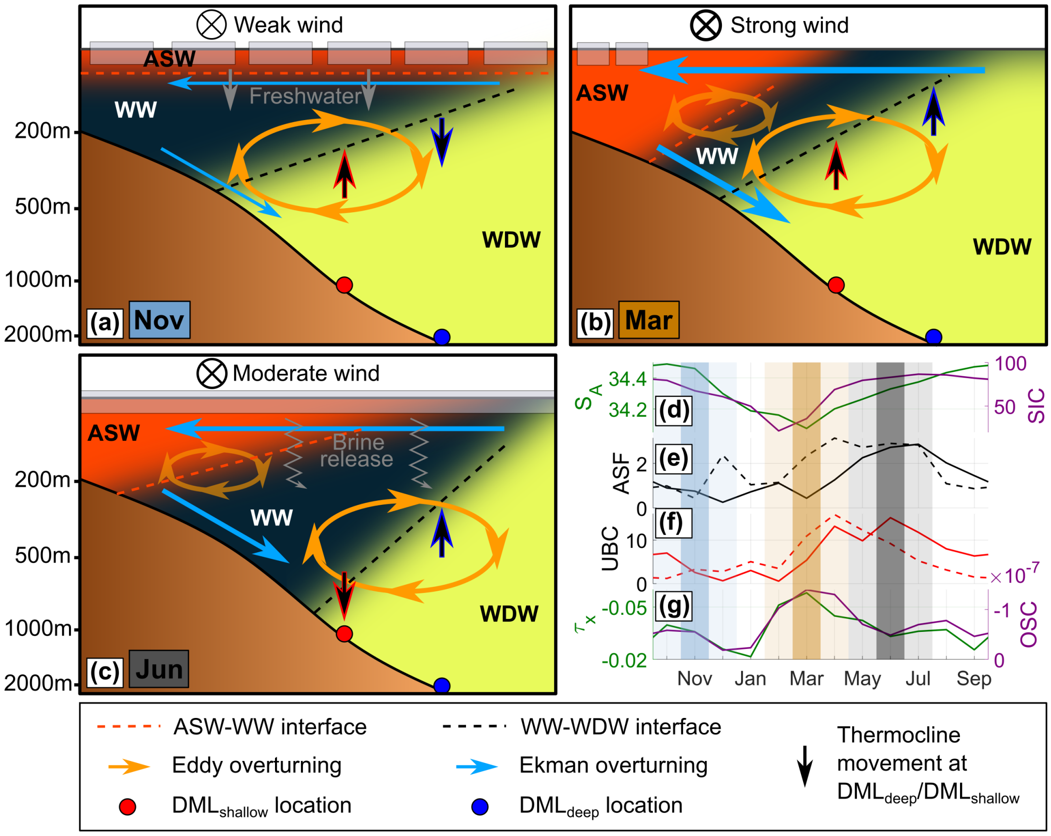

Figure 10. Sketches of different phases of the baroclinic seasonal cycle during (a) November, (b) March, and (c) June. Seasonal time series of relevant variables, i.e. (d) surface absolute salinity over $DML_{shallow}$ isobath from H18 data and sea ice concentration climatology (2010-2021) at $DML_{shallow}$, (e) mean seasonal ASF slope between DML_{deep} and $DML_{shallow}$ from mooring observations and H18 data, (f) mean seasonal mooring and H18 baroclinic velocity at $DML_{shallow}$ at 100 m depth, and (g) zonal ocean stress (left axis) and ocean stress curl (right axis) climatology (2010-2021) averaged over 0−15°E and 69.5−70°S/67−69.5°S, respectively. Colored shadings indicate the timing of the sketches in panels a-c.

We find the barotropic component of the ASC at 6°E to be forced by upstream ocean stress, consistent with results from earlier studies (Núñez-Riboni & Fahrbach, 2009; Graham et al., 2013; Le Paih et al., 2020). However, in contrast to Núñez-Riboni and Fahrbach (2009) at the prime meridian, we do not find a conclusive offshore lag in the seasonality of the barotropic component in the mooring records or H18 data. Instead, we observe a clear offshore lag in subsurface salinity, thermocline depth, and resulting surface baroclinic velocity seasonality in both data sets. Interestingly, the moorings from Núñez-Riboni and Fahrbach (2009) show a delay of one to three months in long-term temperature seasonality at 200 m and 700 m depth over the 3500 m isobath compared to the 2000 m isobath (Fig. S4 in Supporting Information S1 and Fig. 5 in Le Paih et al., 2020). This is in agreement with our observed temperature seasonalities at the DML moorings and therefore consistent with the offshore lag in thermocline depth seasonality at 6°E and 17°W. In fact, Núñez-Riboni and Fahrbach (2009) assumed the depth-weighted average of the total observed velocity to be the barotropic component, to which the observed offshore delay in ASC strength was attributed. With this approach, however, the barotropic velocity may still contain a significant baroclinic component. Our study shows that the largest offshore delay occurs in the baroclinic component and not, or at least to a lesser extent, in the barotropic component. We therefore suggest that sea ice causes the observed offshore delay in the ASC seasonality mainly in the baroclinc component through seasonal meltwater input and offshore spreading.

There is an apparent link between seasonal variations in both the baroclinic and barotropic ASC strength and flow into the Fimbulisen cavity. While not investigated here in detail, this link may include an intricate interplay between the local bathymetry at the sills (Nøst, 2004; Eisermann et al., 2020), a seasonal counter-current at depth (Heywood et al., 1998; Smedsrud et al., 2006; Núñez-Riboni & Fahrbach, 2009; Chavanne et al., 2010), bottom Ekman transport anomalies (Smedsrud et al., 2006; Núñez-Riboni & Fahrbach, 2009) and potential vorticity constraints (Daae et al., 2017; Wåhlin et al., 2020; Steiger et al., 2022). The absence of a clear relation between the observed offshore thermocline depth and the inflow temperature is surprising and points to that warm inflows are rather controlled by local sub-monthly variations in thermocline depth, forced by variability in winds, sea ice and SSH (Lauber, Hattermann, et al., 2023). In addition, the internal cavity circulation likely also affects the hydrography at the sill, and the seasonal oceanic variability below Fimbulisen will be investigated in more detail in a follow-up study.

6 Summary and Conclusions

Our combined analyses of new mooring observations, climatological hydrography, and satellite-derived surface geostrophic currents have shown that the cross-slope processes controlling the ASF/ASC seasonality are consistent along the DML coast across independent data sets over multiple years in isobath-depth space: in the mooring data at 6°E, we found the seasonal upper-ocean salinity minimum and thermocline depth maximum to occur up to six months later over 2200 m isobath than over 1100 m isobath. The same feature occurs in climatological hydrography at 17°W and translates onto satellite-derived surface geostrophic currents. Our analyses suggest that this offshore delay originates from a seasonal offshore spreading of ASW through eddy overturning at the ASF and the secondary front above. We found the seasonal production of ASW via sea ice melt and subsequent shoreward accumulation to govern the timing of the baroclinic ASC maximum, while variations in ocean stress forcing can additionally modulate the baroclinic seasonality. These findings led us to define three distinct phases describing the seasonality of the ASF/ASC (Fig. 10). These phases may be regarded as generally valid in the Fresh Shelf regime along the East Antarctic coast. Below Fimbulisen, seasonal flow into and out of the cavity is associated with seasonal variations in ASC strength, but the inflow temperature does not follow the offshore thermocline depth. The results of this study contribute to a better understanding of the seasonal variability of the ASF/ASC system along the DML coast and will aid in assessing the impacts of a changing climate on the ASF/ASC.

Data Availability Statement

The DML mooring data will be made available via `https://data.npolar.no` during the revisions. The sub-ice-shelf mooring data will be updated at `https://doi.org/10.21334/npolar.2023.4a6c36f5` (Lauber, de Steur, et al., 2023). The H18 climatology is available at `https://doi.org/10.1594/PANGAEA.893199` (Hattermann & Rohardt, 2018). Sea surface height is available at `https://doi.org/10.17882/81032` (Auger et al., 2021). Sea ice concentration is available at `https://doi.org/10.5067/MPYG15WAA4WX` (DiGirolamo et al., 2022) and sea ice velocity at `https://doi.org/10.5067/INAWUWO7QH7B` (Tschudi et al., 2019). ERA5 wind data are available at `https://doi.org/10.24381/cds.f17050d7` (Hersbach et al., 2023). Bathymetric data are available at `https://doi.org/10.1594/PANGAEA.937574` (Dorschel et al., 2022).

Acknowledgments

This research was funded by the Research Council of Norway through the KLIMAFORSK program (iMelt, 295075). The DML moorings were financed and installed by the Norwegian Polar Institute. The installation of the M1 and M3 moorings through the project "ICE Fimbulisen – top to bottom" was financed by the Centre for Ice, Climate and Ecosystems (ICE), Norwegian Polar Institute (NPI). The latter moorings were maintained by NPI through ICE, the Norwegian Antarctic Research Expedition (IceRises 759, 3801-103), and iMelt. J.L. was funded by iMelt, and T.H. by the European Union's Horizon 2020 programme (CRiceS, 101003826). We thank the sections Maritime and Technical Support and Operations and Logistics Antarctica from NPI for all their support involving the moorings.

References

Armitage, T. W. K., Kwok, R., Thompson, A. F., & Cunningham, G. (2018). Dynamic Topography and Sea Level Anomalies of the Southern Ocean: Variability and Teleconnections. *Journal of Geophysical Research: Oceans*, *123*, 613-630.

Auger, M., Prandi, P., & Sallée, J.-B. (2022). Southern ocean sea level anomaly in the sea ice-covered sector from multimission satellite observations. *Scientific Data*, *9*(70), 1-10.

Auger, M., Prandi, P., & Sallée, J.-B. (2021). Daily Southern Ocean Sea Level Anomaly And Geostrophic Currents from multimission altimetry, 2013-2019. *SEANOE*. (URL: https://doi.org/10.17882/81032. Last accessed: 13.06.2022)

Auger, M., Sallée, J.-B., Prandi, P., & Naveira Garabato, A. C. (2022). Subpolar Southern Ocean Seasonal Variability of the Geostrophic Circulation From Multi-Mission Satellite Altimetry. *Journal of Geophysical Research: Oceans*, *127*, 1-16.

Chavanne, C. P., Heywood, K. J., Nicholls, K. W., & Fer, I. (2010). Observations of the Antarctic Slope Undercurrent in the southeastern Weddell Sea. *Geophysical Research Letters*, *37*(L13601), 1-5. Retrieved from https://agupubs.onlinelibrary.wiley.com/doi/abs/10.1029/2010GL043603 doi: https://doi.org/10.1029/2010GL043603

Daae, K., Hattermann, T., Darelius, E., & Fer, I. (2017). On the effect of topography and wind on warm water inflow — An idealized study of the southern Weddell Sea continental shelf system. *Journal of Geophysical Research: Oceans*, *122*(3), 2622-2641. Retrieved from https://agupubs.onlinelibrary.wiley.com/doi/abs/10.1002/2016JC012541 doi:

https://doi.org/10.1002/2016JC012541

Deacon, G. (1979). The Weddell gyre. *Deep Sea Research Part A. Oceanographic Research Papers*, *26*(9), 981-995. Retrieved from `https://www.sciencedirect.com/science/article/pii/019801497990044X` doi: 10.1016/0198-0149(79)90044-X

DiGirolamo, N., Parkinson, C. L., Cavalieri, D. J., Gloersen, P., & Zwally, H. J. (2022). Sea Ice Concentrations from Nimbus-7 SMMR and DMSP SSM/I-SSMIS Passive Microwave Data, Version 2. [March 2019 to January 2021, 180°W - 180°E and 90°S - 40°S]. *NASA National Snow and Ice Data Center Distributed Active Archive Center. Boulder/Colorado/USA.*. (URL: `https://doi.org/10.5067/MPYG15WAA4WX`. Last accessed: 21.11.2022)

Dorschel, B., Hehemann, L., Viquerat, S., Warnke, F., Dreutter, S., Schulze Tenberge, Y., ... Arndt, J. E. (2022). The International Bathymetric Chart of the Southern Ocean Version 2 (IBCSO v2). *PANGAEA.* (URL: `https://doi.org/10.1594/PANGAEA.937574`. Last accessed: 15.06.2022)

Dorschel, B., Hehemann, L., Viquerat, S., Warnke, F., Dreutter, S., Tenberge, Y. S., ... others (2022). The International Bathymetric Chart of the Southern Ocean Version 2. *Scientific Data*, *9*(275), 1-13.

Dotto, T. S., Naveira Garabato, A., Bacon, S., Tsamados, M., Holland, P. R., Hooley, J., ... Meredith, M. P. (2018). Variability of the Ross Gyre, Southern Ocean: Drivers and Responses Revealed by Satellite Altimetry. *Geophysical Research Letters*, *45*, 6195-6204.

Eisermann, H., Eagles, G., Ruppel, A., Smith, E. C., & Jokat, W. (2020). Bathymetry Beneath Ice Shelves of Western Dronning Maud Land, East Antarctica, and Implications on Ice Shelf Stability. *Geophysical Research Letters*, *47*(12), 1-10.

Gordon, A., Martinson, D., & Taylor, H. (1981). The wind-driven circulation in the Weddell-Enderby Basin. *Deep Sea Research Part A. Oceanographic Research Papers*, *28*(2), 151-163. Retrieved from `https://www.sciencedirect.com/science/article/pii/019801498190087X` doi: 10.1016/0198-0149(81)90087-X

Graham, J. A., Heywood, K. J., Chavanne, C. P., & Holland, P. R. (2013). Seasonal variability of water masses and transport on the Antarctic continental shelf and slope in the southeastern Weddell Sea. *Journal of Geophysical Research: Oceans*, *118*(4), 2201-2214.

Haran, T., Klinger, M., Bohlander, J., Fahnestock, M., Painter, T., & Scambos, T. (2018). MEaSUREs MODIS Mosaic of Antarctica 2013-2014 (MOA2014) Image Map, Version 1. [moa750_2014_hp1_v01.tif]. *NASA National Snow and Ice Data Center Distributed Active Archive Center. Boulder/Colorado/USA.*. (URL: `https://nsidc.org/data/NSIDC-0730/versions/1`. Last accessed: 25.08.2021)

Hattermann, T. (2018). Antarctic Thermocline Dynamics along a Narrow Shelf with Easterly Winds. *Journal of Physical Oceanography*, *48*(10), 2419-2443.

Hattermann, T., Nøst, O. A., Lilly, J. M., & Smedsrud, L. H. (2012). Two years of oceanic observations below the Fimbul Ice Shelf, Antarctica. *Geophysical Research Letters*, *39*(12), 1-6.

Hattermann, T., & Rohardt, G. (2018). Kapp Norvegia Antarctic Slope Front climatology. *Alfred Wegener Institute, Helmholtz Centre for Polar and Marine Research, Bremerhaven, PANGAEA*. (URL: `https://doi.org/10.1594/PANGAEA.893199`. Last accessed: 24.08.2022)

Hersbach, H., Bell, B., Berrisford, P., Biavati, G., Horányi, A., Muñoz Sabater, J., . . . Thépaut, J.-N. (2023). ERA5 monthly averaged data on single levels from 1940 to present. *Copernicus Climate Change Service (C3S) Climate Data Store (CDS).* (URL: `https://doi.org/10.24381/cds.f17050d7`. Last accessed: 02.11.2021)

Heywood, K. J., Locarnini, R. A., Frew, R. D., Dennis, P. F., & King, B. A. (1998). Transport and Water Masses of the Antarctic Slope Front System in The Eastern Weddell Sea. In S. S. Jacobs & R. F. Weiss (Eds.). *Ocean, ice, and atmosphere: Interactions at the Antartic continental margin, Antarctic Research Series.*, *75*, 203-214. Retrieved from `https://agupubs.onlinelibrary.wiley.com/doi/abs/10.1029/AR075p0203` (Washington, DC: American Geophysical Union) doi: https://doi.org/10.1029/AR075p0203

Huneke, W. G. C., Morrison, A. K., & Hogg, A. M. (2022). Spatial and Subannual Variability of the Antarctic Slope Current in an Eddying Ocean–Sea Ice Model. *Journal of Physical Oceanography*, *52*(3), 347 - 361. Retrieved from `https://journals.ametsoc.org/view/journals/phoc/52/`

3/JPO-D-21-0143.1.xml doi: https://doi.org/10.1175/JPO-D-21-0143.1

Isachsen, P. E., LaCasce, J. H., Mauritzen, C., & Häkkinen, S. (2003). Wind-Driven Variability of the Large-Scale Recirculating Flow in the Nordic Seas and Arctic Ocean. *Journal of Physical Oceanography*, *33*(12), 2534 - 2550. Retrieved from https://journals.ametsoc.org/view/journals/phoc/33/12/1520-0485_2003_033_2534_wvotlr_2.0.co_2.xml doi: 10.1175/1520-0485(2003)033⟨2534:WVOTLR⟩2.0.CO;2

Jacobs, S. S. (1991). On the nature and significance of the Antarctic Slope Front. *Marine Chemistry*, *35*(1), 9-24. doi: https://doi.org/10.1016/S0304-4203(09)90005-6

Lauber, J., de Steur, L., Hattermann, T., & Nøst, O. A. (2023). Daily averages of physical oceanography and current meter data from sub-ice-shelf moorings M1, M2 and M3 at Fimbulisen, East Antarctica since 2009. *Norwegian Polar Institute, Tromsø*. (URL: https://doi.org/10.21334/npolar.2023.4a6c36f5. Last accessed: 07.07.2023)

Lauber, J., Hattermann, T., de Steur, L., Darelius, E., Auger, M., Nøst, O., & Moholdt, G. (2023). Warming beneath an East Antarctic ice shelf due to increased subpolar westerlies and reduced sea ice. *Nature Geoscience*. doi: 10.1038/s41561-023-01273-5

Le Paih, N., Hattermann, T., Boebel, O., Kanzow, T., Lüpkes, C., Rohardt, G., ... Herbette, S. (2020). Coherent Seasonal Acceleration of the Weddell Sea Boundary Current System Driven by Upstream Winds. *Journal of Geophysical Research: Oceans*, *125*(e2020JC016316), 1-20.

Martin, T., Tsamados, M., Schroeder, D., & Feltham, D. L. (2016). The impact of variable sea ice roughness on changes in Arctic Ocean surface stress: A model study. *Journal of Geophysical Research: Oceans*, *121*, 1931-1952.

Mathiot, P., Goosse, H., Fichefet, T., Barnier, B., & Gallée, H. (2011). Modelling the seasonal variability of the Antarctic Slope Current. *Ocean Science*, *7*, 455-470. doi: https://doi.org/10.5194/os-7-455-2011

McDougall, T. J., & Barker, P. M. (2011). Getting started with TEOS-10 and the Gibbs Seawater (GSW) Oceanographic Toolbox. *Scor/Iapso WG127*, 1-32.

Nakayama, Y., Greene, C. A., Paolo, F. S., Mensah, V., Zhang, H., Kashiwase, H., ... Aoki, S. (2021). Antarctic Slope Current Modulates Ocean Heat Intrusions

Towards Totten Glacier. *Geophysical Research Letters*, *48*(17), 1-10.

Naveira Garabato, A. C., Dotto, T. S., Hooley, J., Bacon, S., Tsamados, M., Ridout, A., ... Meredith, M. P. (2019). Phased Response of the Subpolar Southern Ocean to Changes in Circumpolar Winds. *Geophysical Research Letters*, *46*(11), 6024-6033.

Neme, J., England, M. H., & Hogg, A. M. (2021). Seasonal and Interannual Variability of the Weddell Gyre From a High-Resolution Global Ocean-Sea Ice Simulation During 1958–2018. *Journal of Geophysical Research: Oceans*, *126*, 1-19.

Nøst, O. A. (2004). Measurements of ice thickness and seabed topography under the Fimbul Ice Shelf, Dronning Maud Land, Antarctica. *Journal of Geophysical Research: Oceans*, *109*, 1-14.

Nøst, O. A., Biuw, M., Tverberg, V., Lydersen, C., Hattermann, T., Zhou, Q., ... Kovacs, K. M. (2011). Eddy overturning of the Antarctic Slope Front controls glacial melting in the Eastern Weddell Sea. *Journal of Geophysical Research: Oceans*, *116*, 1-17.

Núñez-Riboni, I., & Fahrbach, E. (2009). Seasonal variability of the Antarctic Coastal Current and its driving mechanisms in the Weddell Sea. *Deep Sea Research Part I: Oceanographic Research Papers*, *56*(11), 1927-1941.

Pauthenet, E., Sallée, J.-B., Schmidtko, S., & Nerini, D. (2021). Seasonal Variation of the Antarctic Slope Front Occurrence and Position Estimated from an Interpolated Hydrographic Climatology. *Journal of Physical Oceanography*, *51*(5), 1539 - 1557. Retrieved from `https://journals.ametsoc.org/view/journals/phoc/51/5/JPO-D-20-0186.1.xml` doi: https://doi.org/10.1175/JPO-D-20-0186.1

Si, Y., Stewart, A. L., & Eisenman, I. (2023). Heat transport across the Antarctic Slope Front controlled by cross-slope salinity gradients. *Science Advances*, *9*(18), 1-12. Retrieved from `https://www.science.org/doi/abs/10.1126/sciadv.add7049` doi: 10.1126/sciadv.add7049

Smedsrud, L. H., Jenkins, A., Holland, D. M., & Nøst, O. A. (2006). Modeling ocean processes below Fimbulisen, Antarctica. *Journal of Geophysical Research: Oceans*, *111*, 1-13.

Steiger, N., Darelius, E., Kimura, S., Patmore, R. D., & Wåhlin, A. K. (2022).

The Dynamics of a Barotropic Current Impinging on an Ice Front. *Journal of Physical Oceanography*, *52*(12), 2957 - 2973. Retrieved from `https://journals.ametsoc.org/view/journals/phoc/52/12/JPO-D-21-0312.1.xml` doi: 10.1175/JPO-D-21-0312.1

Stewart, A. L., Klocker, A., & Menemenlis, D. (2019). Acceleration and Overturning of the Antarctic Slope Current by Winds, Eddies, and Tides. *Journal of Physical Oceanography*, *49*(8), 2043 - 2074. Retrieved from `https://journals.ametsoc.org/view/journals/phoc/49/8/jpo-d-18-0221.1.xml` doi: 10.1175/JPO-D-18-0221.1

Stewart, A. L., & Thompson, A. F. (2015). Eddy-mediated transport of warm Circumpolar Deep Water across the Antarctic Shelf Break. *Geophysical Research Letters*, *42*(2), 432-440. Retrieved from `https://agupubs.onlinelibrary.wiley.com/doi/abs/10.1002/2014GL062281` doi: 10.1002/2014GL062281

Sverdrup, H. U. (1954). The Currents off the Coast of Queen Maud Land. *Norsk Geografisk Tidsskrift*, *14*(1-4), 239-249.

Thompson, A. F., Heywood, K. J., Schmidtko, S., & Stewart, A. L. (2014). Eddy transport as a key component of the Antarctic overturning circulation. *Nature Geosciences*, *7*, 879-884.

Thompson, A. F., Stewart, A. L., Spence, P., & Heywood, K. J. (2018). The Antarctic Slope Current in a Changing Climate. *Reviews of Geophysics*, *56*, 741-770.

Tsamados, M., Feltham, D. L., Schroeder, D., Flocco, D., Farrell, S. L., Kurtz, N., … Bacon, S. (2014). Impact of Variable Atmospheric and Oceanic Form Drag on Simulations of Arctic Sea Ice. *Journal of Physical Oceanography*, *44*(5), 1329 - 1353.

Tschudi, M., Meier, W. N., Stewart, J. S., Fowler, C., & Maslanik, J. (2019). Polar Pathfinder Daily 25 km EASE-Grid Sea Ice Motion Vectors, Version 4. [March 2019 to January 2021, 180°W - 180°E and 90°S - 37°S]. *NASA National Snow and Ice Data Center Distributed Active Archive Center. Boulder/Colorado/USA.*. (URL: `https://doi.org/10.5067/INAWUWO7QH7B`. Last accessed: 08.03.2022)

Vernet, M., Geibert, W., Hoppema, M., Brown, P. J., Haas, C., Hellmer, H. H., … Verdy, A. (2019). The Weddell Gyre, Southern Ocean: Present Knowledge and Future Challenges. *Reviews of Geophysics*, *57*(3), 623-708. Retrieved from https://agupubs.onlinelibrary.wiley.com/doi/abs/10.1029/2018RG000604 doi: 10.1029/2018RG000604

Wåhlin, A. K., Steiger, N., Darelius, E., Assmann, K. M., Glessmer, M. S., Ha, H. K., … Viboud, S. (2020). Ice front blocking of ocean heat transport to an Antarctic ice shelf. *Nature*, *578*(7796), 568-571.

Webb, D. J., Holmes, R. M., Spence, P., & England, M. H. (2022). Propagation of barotropic Kelvin waves around Antarctica. *Ocean Dynamics*, *72*, 405-419.

Zhou, Q., Hattermann, T., Nøst, O. A., Biuw, M., Kovacs, K. M., & Lydersen, C. (2014). Wind-driven spreading of fresh surface water beneath ice shelves in the Eastern Weddell Sea. *Journal of Geophysical Research: Oceans*, *119*, 3818-3833.

JOURNAL OF GEOPHYSICAL RESEARCH

Supporting Information for "Observed Seasonal Evolution of the Antarctic Slope Current System at the Coast of Dronning Maud Land, East Antarctica"

Julius Lauber[1,2], Laura de Steur[1], Tore Hattermann[1], Elin Darelius[2,3]

[1]Norwegian Polar Institute, Tromsø, Norway

[2]Geophysical Institute, University of Bergen, Bergen, Norway

[3]Bjerknes Centre for Climate Research, Bergen, Norway

Contents of this file

Introduction This file contains one text and several figures and tables that supplement the analyses presented in the main text: Text S1 describes how uncertainties of the velocity estimates were calculated. Fig. S1 shows time series of oxygen in comparison with salinity. Fig. S2 shows the seasonal time-depth evolution of salinity at the mooring bathymetries for the H18 data. Fig. S3 shows the seasonal thermocline depth evolution in time-bathymetry space for the H18 data. Fig. S4 shows the $\mathrm{DML_{shallow}}$ and $\mathrm{DML_{shallow}}$

Corresponding author: J. Lauber, Norwegian Polar Institute, Hjalmar Johansens gate 14, 9296 Tromsø, Norway. (julius.lauber@npolar.no)

temperature time series in comparison to the climatological temperature from moorings AWI233 and AWI232 at the prime meridian. Tables S1 and S2 show details of all instruments at $\mathrm{DML}_{\mathrm{shallow}}$ and $\mathrm{DML}_{\mathrm{deep}}$, respectively.

Text S1: Uncertainties of velocity estimates

The uncertainty of the satellite-derived surface geostrophic velocity climatology (Fig. 6a) is obtained by taking the standard deviation at the respective data point and for all available data during respective month from April 2013 to July 2019.

The uncertainty of UBT_{obs} (Fig. 6b, Eqn. 2 in the main text) is estimated as follows: First, the error of the velocity measured by the two 150 kHz ADCPs at depth is obtained as given by the manufacturer (Teledyne Marine, 2023):

$$\sigma_{U_{ADCP}} = 0.005\, U_{ADCP} + 0.5\,\mathrm{cm\,s^{-1}} \tag{1}$$

Here, U_{ADCP} is the velocity measured by the ADCPs. This error is propagated to UBT_{obs}, which is the average of the lowermost 12 ADCP bins at depth, according to Gauss' law of error propagation:

$$\sigma_{UBT_{obs_{prelim}}} = \frac{1}{N}\sqrt{\sum_{i=1}^{N} \sigma^2_{U_{ADCP_i}}} \tag{2}$$

Here, $N = 12$ is the number of bins over which the average is taken. To also take into account the fact that the vertical gradient in velocity is not exactly zero at the ADCP depths, as seen in Fig. 5, the standard deviation over the 12 bins, $\sigma_{U_{ADCP_{\Delta z}}}$, is added to $\sigma_{UBT_{obs_{prelim}}}$, so that the final uncertainty of UBT_{obs} is

$$\sigma_{UBT_{obs}} = \frac{1}{N}\sqrt{\sum_{i=1}^{N}\sigma^2_{U_{ADCP_i}}} + \sigma_{U_{ADCP_{\Delta z}}}. \tag{3}$$

The uncertainty of UBC_{obs} (Fig. 6d, Eqn. 4 in the main text), calculated as the difference between the observed velocity at the uppermost bin of the near-surface ADCPs (U_{ADCP}) and UBT_{obs}, is estimated as follows: During times when measurements at this bin are available, the uncertainty of U_{ADCP} is calculated according to Eqn. 1. When no measurements are available, mostly during the winter months due to reduced primary production and resulting reduced backscatter, the uncertainty of the extrapolated value is obtained from the uncertainty of the vertical linear regression according to

$$\sigma_{U_{ADCP}} = \sqrt{\sigma_a^2 + d^2\sigma_b^2}. \tag{4}$$

Here, σ_a and σ_b are the uncertainties of the axis intercept and slope of the linear regression, respectively, and d is the depth of the uppermost ADCP bin, i.e. 100 m at $\mathrm{DML_{shallow}}$ and 20 m at $\mathrm{DML_{deep}}$. The error propagation from the uncertainty of the linear regression is sufficient to estimate the uncertainty of the extrapolated value since, tested during periods when all bins were available, the extrapolation generally did not lead to an overestimate of the velocity at the depth of the uppermost bin. Again from error propagation, the final uncertainty of UBC_{obs} is then

$$\sigma_{UBC_{obs}} = \sqrt{\sigma^2_{U_{ADCP}} + \sigma^2_{UBT_{obs}}}. \tag{5}$$

We refrain from estimating uncertainties for UBC_{H18} since the H18 data are based on over 40 years of data across different observational platforms. Since UBT_{H18A22} is derived from UBC_{H18}, we also do not provide uncertainty for this velocity estimate.

References

Fahrbach, E., & Rohardt, G. (2012a). Physical oceanography and current meter data from mooring AWI232-1. *Alfred Wegener Institute, Helmholtz Centre for Polar and Marine Research, Bremerhaven, PANGAEA.* (URL: `https://doi.org/10.1594/PANGAEA.793090`. Last accessed: 11.06.2022)

Fahrbach, E., & Rohardt, G. (2012b). Physical oceanography and current meter data from mooring AWI232-2. *Alfred Wegener Institute, Helmholtz Centre for Polar and Marine Research, Bremerhaven, PANGAEA.* (URL: `https://doi.org/10.1594/PANGAEA.793091`. Last accessed: 11.06.2022)

Fahrbach, E., & Rohardt, G. (2012c). Physical oceanography and current meter data from mooring AWI232-3. *Alfred Wegener Institute, Helmholtz Centre for Polar and Marine Research, Bremerhaven, PANGAEA.* (URL: `https://doi.org/10.1594/PANGAEA.793092`. Last accessed: 11.06.2022)

Fahrbach, E., & Rohardt, G. (2012d). Physical oceanography and current meter data from mooring AWI232-4. *Alfred Wegener Institute, Helmholtz Centre for Polar and Marine Research, Bremerhaven, PANGAEA.* (URL: `https://doi.org/10.1594/PANGAEA.793093`. Last accessed: 11.06.2022)

Fahrbach, E., & Rohardt, G. (2012e). Physical oceanography and current meter data from mooring AWI232-5. *Alfred Wegener Institute, Helmholtz Centre for Polar and Marine Research, Bremerhaven, PANGAEA.* (URL: `https://doi.org/10.1594/`

PANGAEA.793094. Last accessed: 11.06.2022)

Fahrbach, E., & Rohardt, G. (2012f). Physical oceanography and current meter data from mooring AWI232-6. *Alfred Wegener Institute, Helmholtz Centre for Polar and Marine Research, Bremerhaven, PANGAEA.* (URL: https://doi.org/10.1594/PANGAEA.793095. Last accessed: 11.06.2022)

Fahrbach, E., & Rohardt, G. (2012g). Physical oceanography and current meter data from mooring AWI233-1. *Alfred Wegener Institute, Helmholtz Centre for Polar and Marine Research, Bremerhaven, PANGAEA.* (URL: https://doi.org/10.1594/PANGAEA.793096. Last accessed: 11.06.2022)

Fahrbach, E., & Rohardt, G. (2012h). Physical oceanography and current meter data from mooring AWI233-2. *Alfred Wegener Institute, Helmholtz Centre for Polar and Marine Research, Bremerhaven, PANGAEA.* (URL: https://doi.org/10.1594/PANGAEA.793097. Last accessed: 11.06.2022)

Fahrbach, E., & Rohardt, G. (2012i). Physical oceanography and current meter data from mooring AWI233-3. *Alfred Wegener Institute, Helmholtz Centre for Polar and Marine Research, Bremerhaven, PANGAEA.* (URL: https://doi.org/10.1594/PANGAEA.793098. Last accessed: 11.06.2022)

Fahrbach, E., & Rohardt, G. (2012j). Physical oceanography and current meter data from mooring AWI233-4. *Alfred Wegener Institute, Helmholtz Centre for Polar and Marine Research, Bremerhaven, PANGAEA.* (URL: https://doi.org/10.1594/PANGAEA.793099. Last accessed: 11.06.2022)

Fahrbach, E., & Rohardt, G. (2012k). Physical oceanography and current meter data from mooring AWI233-5. *Alfred Wegener Institute, Helmholtz Centre for Polar and*

Marine Research, Bremerhaven, PANGAEA. (URL: https://doi.org/10.1594/PANGAEA.793100. Last accessed: 11.06.2022)

Fahrbach, E., & Rohardt, G. (2012l). Physical oceanography and current meter data from mooring AWI233-6. *Alfred Wegener Institute, Helmholtz Centre for Polar and Marine Research, Bremerhaven, PANGAEA.* (URL: https://doi.org/10.1594/PANGAEA.793101. Last accessed: 11.06.2022)

Fahrbach, E., & Rohardt, G. (2012m). Physical oceanography and current meter data from mooring AWI233-7a. *Alfred Wegener Institute, Helmholtz Centre for Polar and Marine Research, Bremerhaven, PANGAEA.* (URL: https://doi.org/10.1594/PANGAEA.793102. Last accessed: 11.06.2022)

Fahrbach, E., & Rohardt, G. (2012n). Physical oceanography and current meter data from mooring AWI233-7b. *Alfred Wegener Institute, Helmholtz Centre for Polar and Marine Research, Bremerhaven, PANGAEA.* (URL: https://doi.org/10.1594/PANGAEA.793103. Last accessed: 11.06.2022)

Fahrbach, E., & Rohardt, G. (2013a). Physical oceanography and current meter data from mooring AWI232-7. *Alfred Wegener Institute, Helmholtz Centre for Polar and Marine Research, Bremerhaven, PANGAEA.* (URL: https://doi.org/10.1594/PANGAEA.818634. Last accessed: 11.06.2022)

Fahrbach, E., & Rohardt, G. (2013b). Physical oceanography and current meter data from mooring AWI232-8. *Alfred Wegener Institute, Helmholtz Centre for Polar and Marine Research, Bremerhaven, PANGAEA.* (URL: https://doi.org/10.1594/PANGAEA.818635. Last accessed: 11.06.2022)

Fahrbach, E., & Rohardt, G. (2013c). Physical oceanography and current meter data from mooring AWI232-9. *Alfred Wegener Institute, Helmholtz Centre for Polar and Marine Research, Bremerhaven, PANGAEA.* (URL: `https://doi.org/10.1594/PANGAEA.818636`. Last accessed: 11.06.2022)

Rohardt, G., & Boebel, O. (2015). Physical oceanography and current meter data from mooring AWI232-11. *Alfred Wegener Institute, Helmholtz Centre for Polar and Marine Research, Bremerhaven, PANGAEA.* (URL: `https://doi.org/10.1594/PANGAEA.846341`. Last accessed: 11.06.2022)

Rohardt, G., & Boebel, O. (2017a). Physical oceanography and current meter data from mooring AWI232-10. *Alfred Wegener Institute, Helmholtz Centre for Polar and Marine Research, Bremerhaven, PANGAEA.* (URL: `https://doi.org/10.1594/PANGAEA.875134`. Last accessed: 11.06.2022)

Rohardt, G., & Boebel, O. (2017b). Physical oceanography and current meter data from mooring AWI232-12. *Alfred Wegener Institute, Helmholtz Centre for Polar and Marine Research, Bremerhaven, PANGAEA.* (URL: `https://doi.org/10.1594/PANGAEA.875135`. Last accessed: 11.06.2022)

Teledyne Marine. (2023). Workhorse II Data Sheet. *Teledyne RD Instruments*.

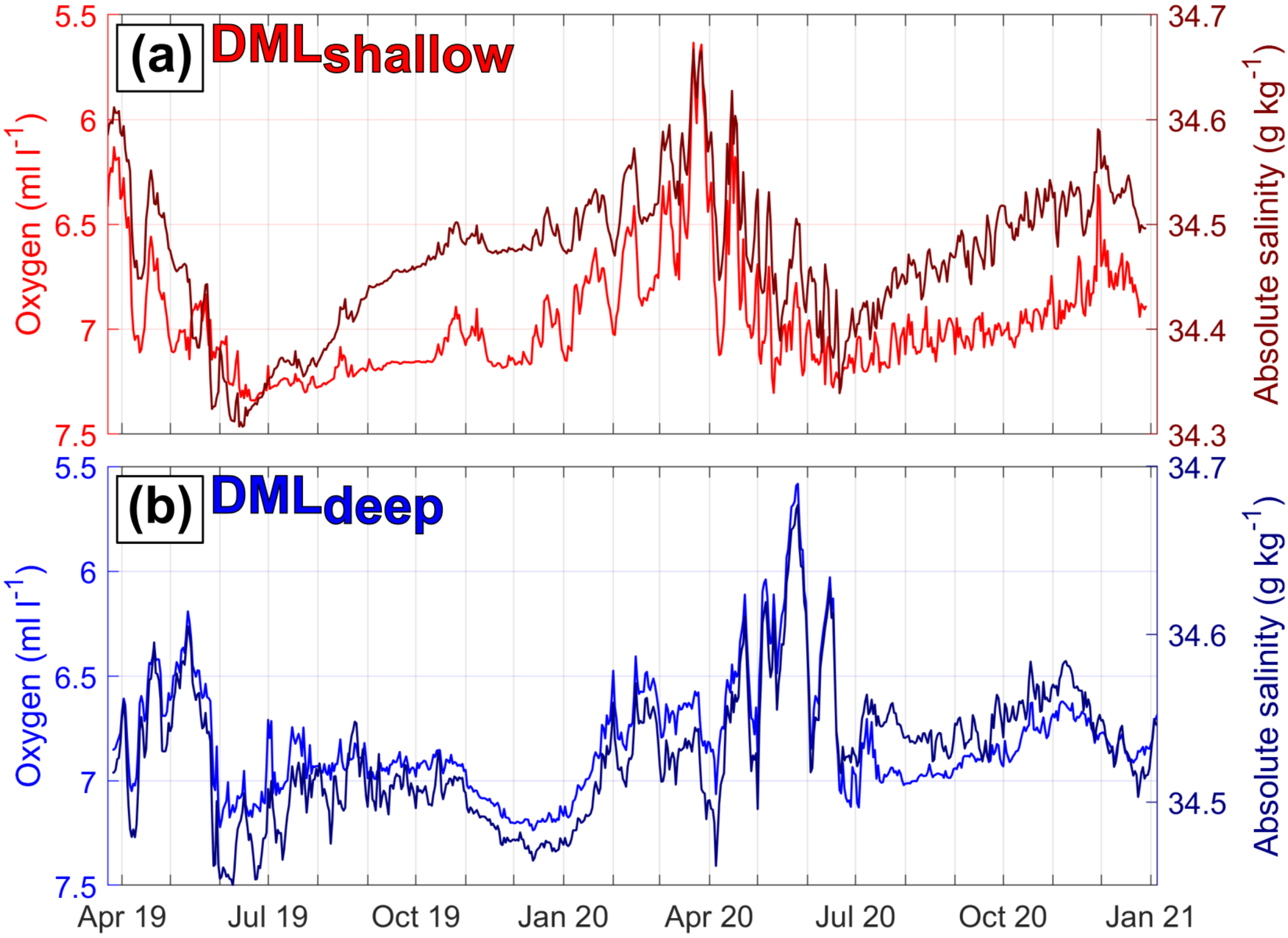

Figure S1. Daily averaged time series of oxygen (left axis) and absolute salinity (right axis) at the uppermost MicroCAT at (a) $\mathrm{DML_{shallow}}$ (210 m) and (b) $\mathrm{DML_{deep}}$ (130 m). Note that the y-axis for oxygen has been reversed for better comparability with the salinity.

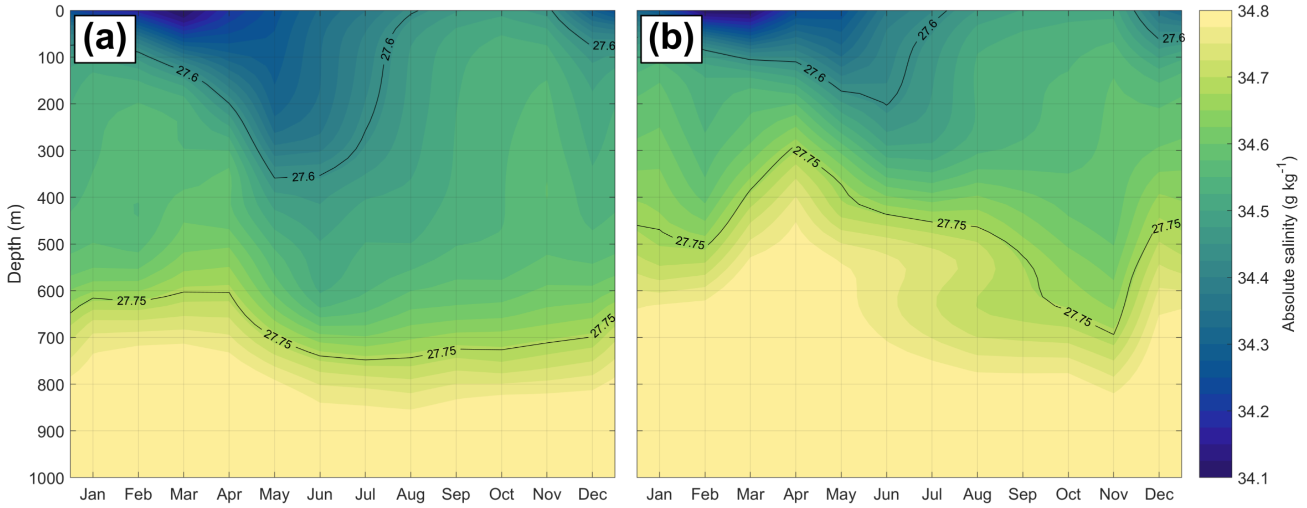

Figure S2. Time-depth Hovmöller diagrams of absolute salinity in the upper 1000 m of the H18 data over (a) $\mathrm{DML}_{\mathrm{shallow}}$ and (b) $\mathrm{DML}_{\mathrm{deep}}$ bathymetry. Contours show selected isolines of potential density in $\mathrm{kg\,m^{-3}}$.

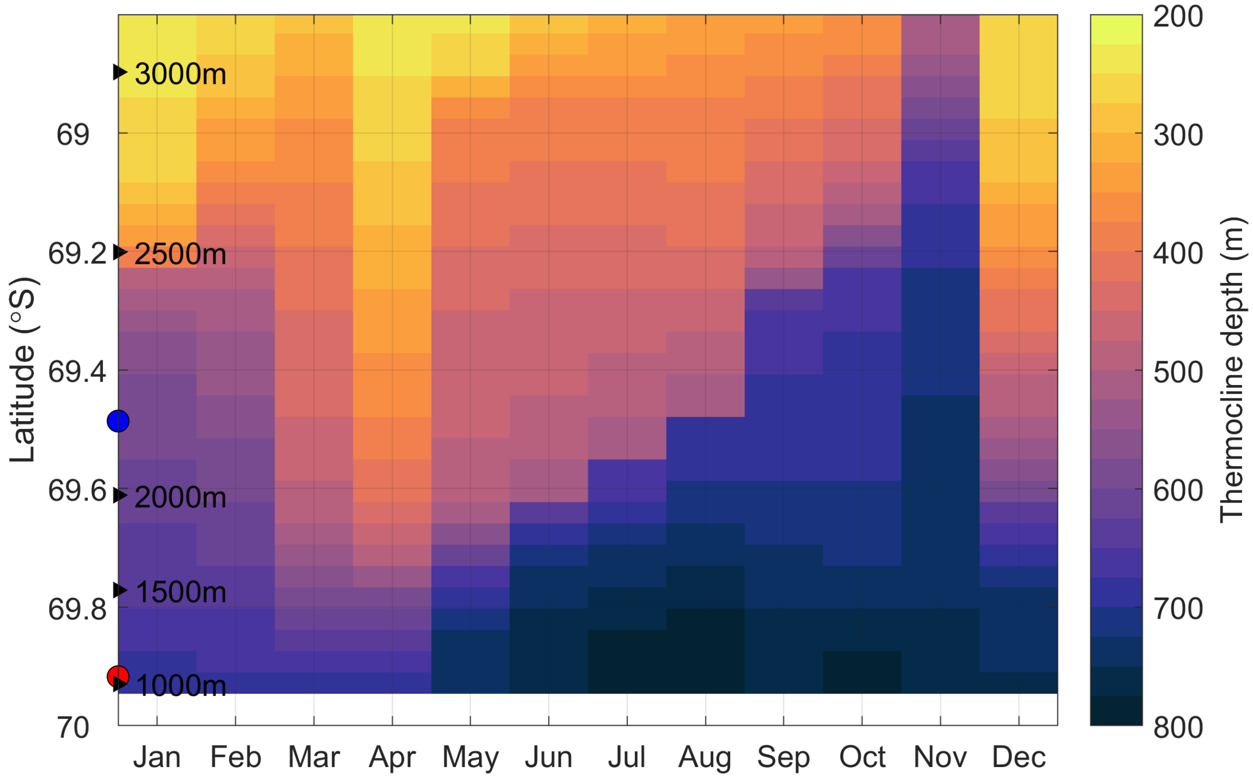

Figure S3. Time-latitude/bathymetry Hovmöller diagram of thermocline depth ($-0.3\,°C$ isotherm) of the H18 data projected on the bathymetry at 6°E. The grid and axis limits are the same as in Fig. 8a.

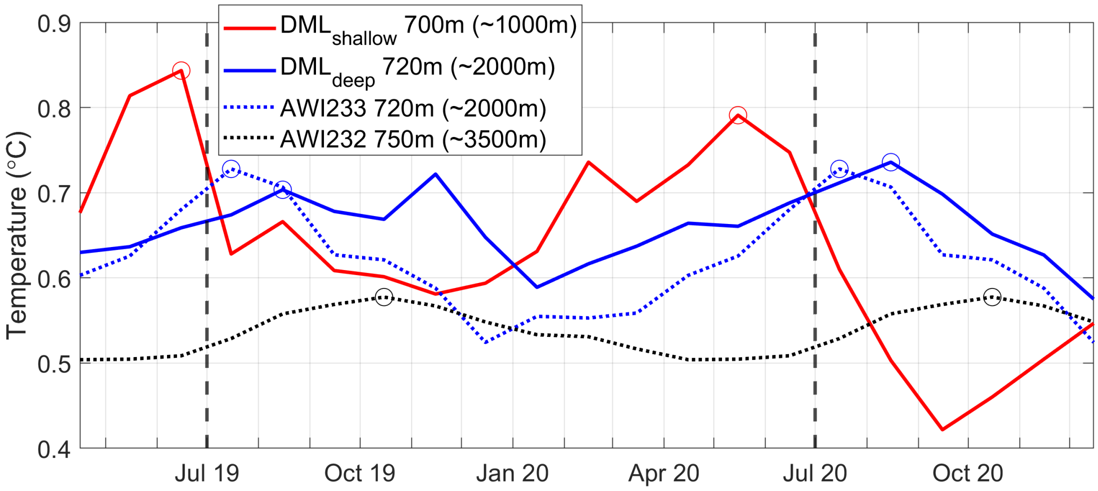

Figure S4. Comparison between temperatures at DML$_{shallow}$, DML$_{deep}$, AWI233 and AWI232 (both at the prime meridian). In the legend, the depth given after the mooring name is the rough depth for which the respective temperature is shown, and the depth in parentheses is the isobath over which the respective mooring is located. The circles indicate corresponding seasonal maxima between the different time series. For the AWI moorings, monthly mean climatologies are shown (AWI233: 1996-2008, AWI232: 1996-2016). The AWI-233 data are taken from Fahrbach and Rohardt (2012g), Fahrbach and Rohardt (2012h), Fahrbach and Rohardt (2012i), Fahrbach and Rohardt (2012j), Fahrbach and Rohardt (2012k), Fahrbach and Rohardt (2012l), Fahrbach and Rohardt (2012m), and Fahrbach and Rohardt (2012n). The AWI-232 data are taken from Fahrbach and Rohardt (2012a), Fahrbach and Rohardt (2012b), Fahrbach and Rohardt (2012c), Fahrbach and Rohardt (2012d), Fahrbach and Rohardt (2012e), Fahrbach and Rohardt (2012f), Fahrbach and Rohardt (2013a), Fahrbach and Rohardt (2013b), Fahrbach and Rohardt (2013c), Rohardt and Boebel (2017a), and Rohardt and Boebel (2015), Rohardt and Boebel (2017b).

$DML_{shallow}$ 69° 22.81' S, 10° 38.23' E / 1059 m		
Instrument	Depth	Duration
ADCP300	207 m	23.3.19 - 4.9.20
SBE37	213 m	23.3.19 - 29.12.20
SBE56	271 m	23.3.19 - 29.12.20
Aquadopp	332 m	23.3.19 - 29.12.20
SBE37	385 m	23.3.19 - 29.12.20
SBE56	447 m	23.3.19 - 29.12.20
SBE56	498 m	23.3.19 - 29.12.20
SBE56	550 m	23.3.19 - 29.12.20
SBE56	601 m	23.3.19 - 29.12.20
SBE56	652 m	23.3.19 - 29.12.20
SBE37	703 m	23.3.19 - 29.12.20
ADCP150	779 m	23.3.19 - 9.11.20
SBE56	814 m	23.3.19 - 29.12.20
SBE56	867 m	23.3.19 - 29.12.20
SBE56	920 m	23.3.19 - 29.12.20
SBE56	973 m	23.3.19 - 29.12.20
SBE37	1040 m	23.3.19 - 29.12.20
Aquadopp	1047 m	23.3.19 - 29.12.20

Table S1. Overview of instruments mounted on mooring $DML_{shallow}$. ADCP300 denotes a short-range 300 kHz ADCP, and ADCP150 a long-range 150 kHz ADCP. SBE 37 is a MicroCAT and SBE56 is a Thermistor.

DML$_{deep}$ 69° 4.08' S, 6° 1.80' E / 2166 m		
Instrument	Depth	Duration
ADCP300	126 m	31.3.19 - 1.11.20
SBE37	132 m	26.3.19 - 5.1.21
SBE56	216 m	26.3.19 - 5.1.21
SBE56	269 m	26.3.19 - 5.1.21
SBE56	374 m	26.3.19 - 5.1.21
Aquadopp	451 m	31.3.19 - 5.1.21
SBE56	505 m	26.3.19 - 5.1.21
SBE56	558 m	26.3.19 - 5.1.21
SBE56	611 m	26.3.19 - 5.1.21
SBE56	663 m	26.3.19 - 5.1.21
SBE56	716 m	26.3.19 - 5.1.21
SBE56	769 m	26.3.19 - 5.1.21
SBE37	821 m	26.3.19 - 5.1.21
ADCP150	880 m	31.3.19 - 10.11.20
SBE56	923 m	26.3.19 - 5.1.21
SBE56	974 m	26.3.19 - 5.1.21
SBE37	2150 m	26.3.19 - 5.1.21
Aquadopp	2158 m	31.3.19 - 5.1.21

Table S2. Same as Table S1, but for DML$_{deep}$.